Universidad Nacional Autónoma de México

FACULTAD DE CIENCIAS

Phase Diagram of the 3d O(4) Model as a Conjecture for Quantum Chromodynamics in the Chiral Limit

T E S I S

QUE PARA OBTENER EL TÍTULO DE:

FÍSICO

P R E S E N T A :

EDGAR LÓPEZ CONTRERAS

TUTOR:

DR. WOLFGANG PETER BIETENHOLZ

Ciudad Universitaria, Cd. Mx., 2021

1. Datos del alumno
López
Contreras
Edgar
Universidad Nacional Autónoma de México
Facultad de Ciencias
Física
414007653

2. Datos del tutor
Dr
Wolfgang Peter
Bietenholz

3. Datos del sinodal 1
Dr
José Alejandro
Ayala
Mercado

4. Datos del sinodal 2
Dr
Pablo
Roig
Garcés

5. Datos del sinodal 3
Dr
Eleazar
Cuautle
Flores

6. Datos del sinodal 4
Dr
Saúl Noé
Ramos
Sánchez

7. Datos del trabajo escrito
Phase Diagram of the 3d O(4) Model as a Conjecture for Quantum Chromodynamics in the Chiral Limit
92 p
2021

Abstract

We present a numerical study of the lattice-regularized 3d O(4) non-linear σ model with chemical potential, as an effective model for finite baryon density QCD with two flavors in the chiral limit. We use L^3 volume lattices, with L between 13.6 and 27.2 fm. We explore chemical potential values between 0 and 363 MeV.

From the 4d O(4) non-linear σ model we perform a high temperature dimensional reduction down to a three dimensional model. The 3d model has topological sectors characterized by the topological charge. As in the Skyrme model, the topological charge is interpreted as the baryon number and the chemical potential is related to the baryon density.

In the 3d O(4) non-linear σ model the O(4) symmetry breaks spontaneously down to O(3). This symmetry breaking is locally isomorphic to the chiral symmetry breaking of QCD with two flavors in the chiral limit, $\mathrm{SU_L}(2) \otimes \mathrm{SU_R}(2) \to \mathrm{SU_{L=R}}(2)$. It is conjectured that the critical points of the symmetry breakings in these models are in the same universality class.

In our study we use the lattice regularization and the geometrical interpretation of topological charge on the lattice. To capture the topological properties of the 3d O(4) non-linear σ model a non-perturbative approach is required. We perform a numerical study using the multi cluster algorithm.

We obtain several critical exponents at nonzero baryon densities. Our critical exponents at $\mu_B = 0$ deviate from the ones found in the literature, by at most 15%. This indicates that the finite size effects are considerable for the critical exponents. Nevertheless, also in the case $\mu_{B,\mathrm{lat}} = 0$, the finite size effects still allow us to extrapolate the critical temperature consistently with the literature.

We obtain the phase diagram of this model at different baryon densities based on three observables and three autocorrelation times. We obtain the critical temperature $T_c = 154.6(4)$ MeV at $\mu_B = 0$, in agreement with the literature, and $T_c = 124.9(8)$ MeV at $\mu_B = 362.7$ MeV which appears to agree with the non-chiral case from the literature only within 4 sigma. We cover several baryon densities and temperatures at which the Critical End Point of QCD is predicted in part of the literature. The phase diagram boundary is monotonically decreasing, as expected for finite baryon density QCD with two flavors in the chiral limit.

We observe only second order phase transitions, but there are indications of a possible first order phase transition on larger chemical potentials, which are inaccessible in this work due to the required computational time.

A mi mamá y Michelle

Acknowledgements

I would like to thank Dr. Bietenholz for all his support and commitment throughout the development of this work, all our discussions were very helpful. This project would not have been possible without the computational resources that Dr. Bietenholz offered me within the computational cluster of the Instituto de Ciencias Nucleares. I am grateful to José Antonio García Hernández and Miguel Ángel Nava Blanco for their valuable help during the development of my code. I would also like to thank to the Centro de Datos y Cómputo de Alto Rendimiento del ICN for all the technical support. I wish to gratefully acknowledge the financial support of the DGAPA-PAPIIT project IG100219 "Exploración teórica y experimental del diagrama de fase de la cromodinámica cuántica".

Mamá te agradezco con lo más profundo de mi corazón todo tu apoyo, motivación y enseñanzas. Sobre todo, gracias por enseñarme con tu ejemplo que la constancia y dedicación todo lo puede. Nada de esto habría sido posible sin tí, esto es un logro de ambos.

Michelle muchas gracias por siempre motivarme a salir de mi zona de confort, nadie ha cambiado tanto mi vida como tú. Todo ha sido más fácil con tu apoyo y cariño.

Contents

1 Introduction

1.1 Quantum chromodynamics

Quantum chromodynamics (QCD) is the theory that describes the dynamics of quarks (fermions) and gluons (massless bosons of the strong interaction). There are six flavors of quarks, namely up (u), down (d), charm (c), strange (s), top (t) and bottom (b). These quarks are classified in the following three families,

$$\begin{pmatrix} u \\ d \end{pmatrix}, \qquad \begin{pmatrix} c \\ s \end{pmatrix}, \qquad \begin{pmatrix} t \\ b \end{pmatrix}. \tag{1.1}$$

Quarks have a color charge, denoted as red (r), green (g) or blue (b). Gluons carry a superposition of color and anticolor charges, e.g.

$$\frac{1}{\sqrt{2}}(|r\bar{g}\rangle + |g\bar{r}\rangle). \tag{1.2}$$

Gluons couple to quarks and also to each other because they have color charge.

The QCD Lagrangian reads [1]

$$\mathscr{L} = \sum_f \bar{q}_f (i\not{D} - m_f) q_f - \frac{1}{4} G^a_{\mu\nu} G^{\mu\nu}_a, \quad a = 1, \ldots, 8, \tag{1.3}$$

where the sum in the first term runs over the flavors $f \in \{u, d, s, c, b, t\}$ and in the second term summation over repeated indices is understood. In the first term, q_f is the quark field of the flavor f,

$$q_f = \begin{pmatrix} q_{f,r} \\ q_{f,g} \\ q_{f,b} \end{pmatrix}, \tag{1.4}$$

the expression $\not{D}$ is the notation for $\gamma^\mu D_\mu$, where γ^μ are the Dirac matrices and

$$D_\mu = \partial_\mu - i\frac{g}{2}\lambda_a A^a_\mu \tag{1.5}$$

is the covariant derivative acting on fields that transform in the fundamental representation of SU(3). In the second term,

$$G^a_{\mu\nu} = \partial_\mu A^a_\nu - \partial_\nu A^a_\mu + g f^a_{bc} A^b_\mu A^c_\nu, \quad a, b, c = 1, \ldots, 8, \tag{1.6}$$

is the gluon field strength tensor, where A^a_μ are the gluon fields (gauge potentials), λ_a are the Gell-Mann matrices and f^{abc} are the structure constants of SU(3).

The QCD Lagrangian depends on the quark masses m_f and the strong coupling constant g (or $\alpha_s = g^2/4\pi$).

Experimentally, there are no observations of individual quarks or gluons, this is interpreted as the property of *color confinement* (sometimes called simply confinement property), which implies that the asymptotic states must have neutral color charge[1] [2]. Mesons are linear combinations of quark-antiquark pairs with color-anticolor charge. An example of the color wave function of mesons is as follows,

$$\frac{1}{\sqrt{3}}(|r\bar{r}\rangle + |g\bar{g}\rangle + |b\bar{b}\rangle). \tag{1.7}$$

Baryons consist of three quarks of different colors which result in a null color charge. An example of the color wave function of baryons is the following,

$$\frac{1}{\sqrt{6}}(|rgb\rangle + |gbr\rangle + |brg\rangle - |rbg\rangle - |grb\rangle - |bgr\rangle). \tag{1.8}$$

As a consequence of the color charges of the quarks and gluons, the color charges are screened and antiscreened by virtual quarks and virtual gluons, respectively. The dominant effect is antiscreening, as a result, the QCD theory has the property of *asymptotic freedom*, according to which the strong interaction weakens as the energy increases [3]. In the infinite energy limit of QCD, quarks are free.

The parameter $\Lambda_{\mathrm{QCD}} \approx 300$ MeV characterizes the intrinsic scale of QCD[2] [2]. At low energies (less than 1 GeV), the perturbative approximations of QCD are not valid due to the lack of a reliable expansion parameter.

1.2 QCD phase diagram

A rich phase structure is conjectured in the QCD theory [4; 5; 6]. The phase transitions of QCD are located in the non-perturbative region; the phase diagram at finite baryon density is a set of conjectures, which are extremely difficult to verify, both theoretically and experimentally. In the QCD phase diagram, at least the hadronic phase and the quark-gluon plasma have been observed. As an example of the conjectured phase diagram see Fig. 1.1.

In the conjectured phase diagram there is a consensus that at low baryon density, the hadronic and quark-gluon phases are separated by a crossover transition. Recent lattice studies (see below) report $T = 156.5(1.5)$ MeV for the crossover temperature at zero chemical potential [7]. Most of the literature conjectures the existence of a critical end point (CEP) finishing the crossover zone followed by first order phase transitions, however, there is no agreement on its position.

It seems impossible to attain the CEP experimentally with the only two operating hadron colliders, namely the Large Hadron Collider (LHC) and the Relativistic Heavy Ion Collider (RHIC). In the near future the Nuclotron-based Ion Collider fAcility (NICA) [8], the Facility for Antiproton and Ion Research (FAIR) [9] and the Japan Proton Accelerator Research Complex (J-PARC) [10] will operate at favorable baryon densities and temperatures to locate the CEP. The determination of the CEP would be a milestone for physics.

One approach to QCD is known as *lattice QCD*, which uses lattice regularization and Monte Carlo methods to perform non-perturbative studies. The standard Monte Carlo methods in Quantum Field Theory use a probability measure to statistically weight the field configurations $\phi(x)$. Usually this probability measure has the form [11]

[1] The asymptotic states must be color-singlets.

[2] The Λ_{QCD} value depends on the number of flavors and the renormalization scheme.

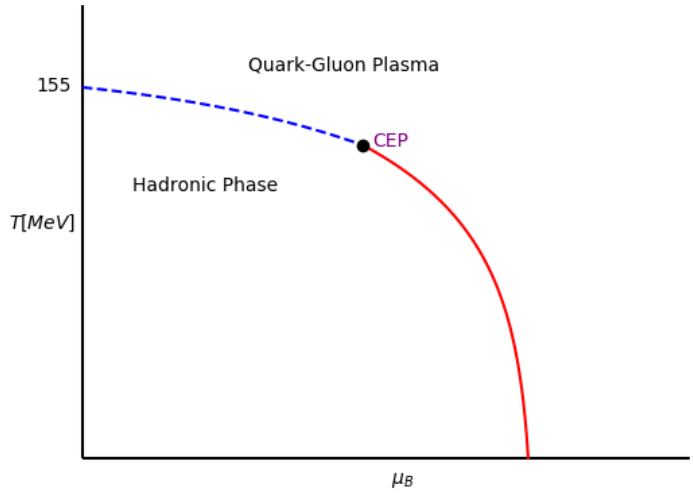

Figure 1.1: *Example of the conjectured phase diagram of QCD, where T denotes temperature and μ_B the baryonic chemical potential. The dashed line represents the crossover transitions and the solid line the first order phase transitions.*

$$p[\phi] = \frac{e^{-S_E[\phi]}}{Z}, \tag{1.9}$$

where $S_E[\phi]$ is the Euclidean action and Z is the partition function. Unfortunately, introducing a real nonzero chemical potential into the QCD Lagrangian generates a complex Euclidean action, causing Eq. (1.9) to be complex, which is a major problem since the probability measure must be real; this is known as the *sign problem* [12; 13]. Therefore, the application of Monte Carlo methods at nonzero chemical potential is not straightforward. However, there are proposals to circumvent the sign problem, such as using an imaginary chemical potential.

1.3 3d O(4) non-linear σ model

The 3d O(4) non-linear σ model has particular features. First, the 3d O(4) non-linear σ model breaks spontaneously its symmetry down to O(3). This symmetry breaking is locally isomorphic to the chiral symmetry breaking of QCD with two flavors in the massless quarks limit, $SU_L(2) \times SU_R(2) \rightarrow SU_{L=R}(2)$ [14]. Second, its field configurations are divided into topological sectors characterized by a topological charge. As in other models (e.g. the Skyrme model) the topological charge represents the baryon number, so although the 3d O(4) model has mesonic fields, the field configurations with nonzero topological charge represent baryonic fields [15]. Third, it is conjectured that the chiral symmetry breaking of QCD with two massless quarks and the symmetry breaking of the 3d O(4) model are in the same universality class [15]. Therefore under this assumption, we can study the phase diagram of QCD with two flavors in the massless quarks limit with the 3d O(4) non-linear σ model. Fourth, the 3d O(4) model can be simulated at finite baryon density without sign problem. These four features are the main motivations of this work.

1.4 Outline

In this work we present a numerical study of the lattice 3d O(4) non-linear σ model with chemical potential. This thesis is composed of the following chapters:

- *Chapter 2.* A brief introduction to the chiral limit of QCD and the O(N) models. A discussion of the topological charge in the continuum and on the lattice can be found here.
- *Chapter 3.* A review of phase transitions and critical phenomena. The definitions of the observables used in this work are presented in this chapter.
- *Chapter 4.* A review of Monte Carlo methods. A discussion on the algorithm used in the numerical study is part of this chapter.
- *Chapter 5.* The results of this work. The graphs of the observables, critical exponents and the phase diagram are presented here.
- *Chapter 6.* Conclusions and possible future work.

2 | 3d O(4) Model with Chemical Potential

2.1 Low energy QCD

The QCD theory has an intrinsic energy scale Λ_{QCD}; with 3 *flavors* in the $\overline{\mathrm{MS}}$ scheme[1] $\Lambda_{\mathrm{QCD}} \approx 300$ MeV [2]. The *light quarks* (the flavors u, d and s) have masses lower than Λ_{QCD}, [16]

$$m_{\mathrm{u}} = 2.16^{+0.49}_{-0.26}\ \mathrm{MeV}, \tag{2.1}$$

$$m_{\mathrm{d}} = 4.67^{+0.48}_{-0.17}\ \mathrm{MeV} \tag{2.2}$$

and

$$m_{\mathrm{s}} = 93^{+11}_{-5}\mathrm{MeV}. \tag{2.3}$$

Therefore, at low energy, the massless quark approximation, known as the *chiral limit*, is to some extent a good approximation for the masses of the light quarks[2] [17].

The QCD Lagrangian, with 3 flavors in the chiral limit, is given by [17]

$$\mathscr{L} = \sum_{l=\mathrm{u,d,s}} (\overline{q}_{\mathrm{L},l} i \not{D} q_{\mathrm{L},l} + \overline{q}_{\mathrm{R},l} i \not{D} q_{\mathrm{R},l}) - \frac{1}{4} G^a_{\mu\nu} G^{\mu\nu}_a, \quad a = 1, \ldots, 8, \tag{2.4}$$

where $q_{\mathrm{L},l}$ and $q_{\mathrm{R},l}$ are the left- and right-handed projections of the quark field q_l,

$$q_{\mathrm{L},l} = P_{\mathrm{L}} q_l, \quad \overline{q}_{\mathrm{L},l} = \overline{q}_l P_{\mathrm{R}}, \tag{2.5}$$

$$q_{\mathrm{R},l} = P_{\mathrm{R}} q_l, \quad \overline{q}_{\mathrm{R},l} = \overline{q}_l P_{\mathrm{L}}, \tag{2.6}$$

where P_{L} and P_{R} are the chiral projection operators,

$$P_{\mathrm{L}} = \frac{1}{2}(1 - \gamma_5), \tag{2.7}$$

$$P_{\mathrm{R}} = \frac{1}{2}(1 + \gamma_5). \tag{2.8}$$

The QCD Lagrangian, with N_{f} flavors in the chiral limit, has a global symmetry

$$\mathrm{U}(N_{\mathrm{f}})_{\mathrm{L}} \otimes \mathrm{U}(N_{\mathrm{f}})_{\mathrm{R}} = \mathrm{SU}(N_{\mathrm{f}})_{\mathrm{L}} \otimes \mathrm{SU}(N_{\mathrm{f}})_{\mathrm{R}} \otimes \mathrm{U}(1)_{\mathrm{V}} \otimes \mathrm{U}(1)_{\mathrm{A}}. \tag{2.9}$$

[1] The *Modified Minimal Subtraction* scheme ($\overline{\mathrm{MS}}$) is a renormalization scheme. The scheme consists of: dimensional regularization in $4-\epsilon$ dimensions, transformation of UV and IR divergences into polynomials in $1/\epsilon - \gamma_E$ and subtraction of divergences, where ϵ comes from the dimensional regularization and $\gamma_E = 0.5772\ldots$ is the Euler constant [2].

[2] The chiral limit is most suitable for the flavors u and d, both of which have masses far below Λ_{QCD}.

The $SU(N_f)_L \otimes SU(N_f)_R$ part corresponds to the chiral symmetry, $U(1)_V$ to the baryon number conservation and $U(1)_A$ to the axial symmetry. At the quantum level the axial symmetry is broken [18; 19].

In the chiral limit, the chiral symmetry breaks spontaneously[3],

$$SU(N_f)_L \otimes SU(N_f)_R \longrightarrow SU(N_f)_{L=R}. \tag{2.10}$$

This process is known as *chiral symmetry breaking* (CSB). The CSB generates $N_f^2 - 1$ Nambu-Goldstone bosons by the Goldstone mechanism[4].

Additionally, the small masses of the light quarks also break explicitly the chiral symmetry in the form of (2.10) [23][5]. In the special case of equal masses of quarks ($m_u = m_d = m_s$), it has been proven that the NGBs acquire mass and these are consistent with the masses of the octet of the *pseudoscalar* mesons (the mesons π^+, π^-, π^0, K^+, K^-, K^0, $\overline{K^0}$ and η) [24; 17].

In the case $N_f = 2$, considering only flavors u and d, the quasi-NGBs are the π-mesons (the mesons π^+, π^- and π^0), which have masses [16]

$$m_{\pi^\pm} = 139.57061(24)\ \text{MeV}, \tag{2.11}$$

$$m_{\pi^0} = 134.9770(5)\ \text{MeV}. \tag{2.12}$$

In the case $N_f = 3$, with all the light quarks (u, d, s), the inclusion of the quark s produces the heavier quasi-NGBs of the octet (the mesons K^+, K^-, K^0, $\overline{K^0}$ and η), which have masses [16]

$$m_{K^\pm} = 493.677(13)\ \text{MeV}, \tag{2.13}$$

$$m_{K^0} = 497.648(22)\ \text{MeV}, \tag{2.14}$$

$$m_\eta = 547.862(18)\ \text{MeV}. \tag{2.15}$$

The large N_c (number of colors) limit of QCD gives an effective theory of low energy QCD, based on meson fields and glueballs [25]. It was shown that this effective theory must be of the non-linear σ model type [26].

2.1.1 Skyrme model

The 3d SU(2) non-linear σ model has topologically nontrivial field configurations characterized by a *topological charge* (Q), which is conserved under infinitesimal transformations [27]. Nevertheless, these configurations are unlikely. To solve this problem, Skyrme added a term to the 4d Lagrangian. The *Skyrme model* Lagrangian reads [27; 28]

[3] When a Langrangian is invariant under a symmetry but not the vacuum state, we say that the theory undergoes a *Spontaneous Symmetry Breaking* (SSB).

[4] The *Goldstone theorem* states that when the Langrangian of a theory has a continuous symmetry, the vacuum state is also invariant under this symmetry or otherwise there must be L massless and spinless particles, where L is the number of Lie generators which do not annihilate the vacuum state (or equivalently that do not leave the vacuum state invariant) [20; 21; 22]. The particles generated by the Goldstone mechanism are called *Nambu-Goldstone bosons* (NGBs).

[5] The Goldstone mechanism is also approximately satisfied in case of an *Explicit Symmetry Breaking* (ESB) originated by small fermions masses. In the ESB case of the Goldstone mechanism, the bosons generated acquire mass and are named *quasi-NGBs* [20; 22].

$$\mathscr{L}[U] = \frac{F_\pi^2}{16}\mathrm{Tr}(\partial_\mu U \partial_\mu U^\dagger) + \mathscr{L}_{\mathrm{Skyrme}}[U], \tag{2.16}$$

where F_π is the pion decay constant and $U(x)$ is a SU(2) field. The so called *Skyrme term* is given by

$$\mathscr{L}_{\mathrm{Skyrme}}[U] = \frac{1}{32e^2}\mathrm{Tr}[(\partial_\mu U)U^\dagger, (\partial_\nu U)U^\dagger]^2, \tag{2.17}$$

where e is a dimensionless parameter.

The Skyrme model is an effective theory of low energy QCD in the large N_c limit [28]. The SU(2) bosonic field represents the mesons π^+ and π^-. Nevertheless, this apparently mesonic field theory includes baryons, which are the solitonic solutions of the field with topological charge $Q = 1$ [27; 26; 29]. Therefore, the topological charge is the baryon number. The solitons of the Skyrme theory are called *skyrmions*.

2.1.2 Lowest order effective Lagrangian

In the $N_f = 2$ case, the lowest order effective Langrangian of QCD is given by the 4d O(4) non-linear σ model coupled to an external field [30]. The Euclidean action of this model reads

$$S_E[\vec{\sigma}, \vec{H}] = F_\pi^2 \int d^4x \left(\frac{1}{2}\partial_\mu \vec{\sigma}(x) \cdot \partial_\mu \vec{\sigma}(x) + \vec{H}(x) \cdot \vec{\sigma}(x)\right), \tag{2.18}$$

where F_π is the pion decay constant, $\vec{\sigma}(x)$ is a four-component real unit vector field, $\vec{\sigma}^{\,2}(x) = 1$, and $\vec{H}(x)$ is the external field. The field $\vec{H}(x)$ is the way to introduce the mass of the quarks to the theory, as is done in [31].

This work is limited to the effective action (2.18) in the chiral limit (without external field),

$$S_E[\vec{\sigma}] = \frac{1}{2}F_\pi^2 \int d^4x\, \partial_\mu \vec{\sigma}(x) \cdot \partial_\mu \vec{\sigma}(x). \tag{2.19}$$

This model undergoes a spontaneous symmetry breaking,

$$\mathrm{O}(4) \longrightarrow \mathrm{O}(3), \tag{2.20}$$

which is locally isomorphic to the CSB of QCD with two massless flavors (2.10) [14],

$$\mathrm{SU}(2)_L \otimes \mathrm{SU}(2)_R \longrightarrow \mathrm{SU}(2)_{L=R}. \tag{2.21}$$

It is conjectured that the symmetry breakings (2.20) and (2.21) belong to the same universality class [32; 33; 34; 35], see Chap. 3.

2.2 O(N) non-linear σ model

In this section we briefly review some of the properties of the O(N) non-linear σ model. Later we will introduce the dimensional reduction and the lattice regularization that allows us to perform a numerical study of this theory.

2.2.1 Definition

Consider a unit vector $\hat{u} \in S^{N-1}$, where S^{N-1} is the $(N-1)$-dimensional unit sphere. We define the field $\vec{\sigma}(x)$ parametrized by [36]

$$\vec{\sigma} = g(x)\hat{u}, \tag{2.22}$$

where $g(x)$ is an element of the orthogonal group $\mathrm{O}(N)$. From the parametrization (2.22) we see that $\vec{\sigma}(x) \in S^{N-1}$, then $\vec{\sigma}(x)$ has the constraint

$$\vec{\sigma}^{\,2}(x) = 1. \tag{2.23}$$

In a field with the constraint (2.23), the general d-dimensional $\mathrm{O}(N)$ symmetric Euclidean action, with at most two derivatives, is given by [36]

$$S_{\mathrm{E}}[\vec{\sigma}] = \frac{F}{2}\int d^d x \partial_\mu \vec{\sigma}(x)\cdot\partial_\mu\vec{\sigma}(x), \tag{2.24}$$

where F is a constant. The constraint (2.23) and the Euclidean action (2.24) define the *d-dimensional $O(N)$ non-linear σ model*.

The stabilizer[6] of $\hat{u}$ is the group $\mathrm{O}(N-1)$. Furthermore [36],

$$\mathrm{O}(N)/\mathrm{O}(N-1) \simeq S^{N-1}, \tag{2.25}$$

i.e. the coset space $\mathrm{O}(N)/\mathrm{O}(N-1)$ is diffeomorphic to S^{N-1}.[7] Due to this diffeomorphism, $\vec{\sigma}(x)$ takes its values in the coset space $\mathrm{O}(N)/\mathrm{O}(N-1)$.

It is well known that the nth homotopy group[8] of S^n satisfies

$$\pi_n(S^n) = \mathbb{Z}, \quad n > 0. \tag{2.26}$$

Based on the diffeomorphism (2.25) we obtain,

$$\pi_{d-1}(\mathrm{O}(d)/\mathrm{O}(d-1)) = \mathbb{Z}, \quad d > 1. \tag{2.27}$$

This implies that the $(d-1)$ dimensional $\mathrm{O}(d)$ non-linear σ model is topologically nontrivial; the field configurations in this model fall into the homotopy classes of $\pi_{d-1}(\mathrm{O}(d)/\mathrm{O}(d-1))$. Let $\vec{\sigma}(x)$ be a field configuration such that it is in the homotopy class Q, $Q \in \mathbb{Z}$, we say that Q is the *topological charge* of $\vec{\sigma}(x)$ and we write it as $Q[\vec{\sigma}(x)]$. The topological charge can be identified by the *winding number* of the field around the d-sphere. The topological charge is conserved under infinitesimal transformations[9].

2.2.2 High temperature dimensional reduction

The high temperature regime of the theory brings a simplification of the action (2.24). In connection with statistical mechanics, the equivalence between inverse temperature T^{-1} ($\beta = 1/T$) and Euclidean time t_E is made[10], i.e. $t_E = 1/T = \beta$ (assuming natural units ($\hbar = c = 1$) and $k_B = 1$,

[6] The *stabilizer* of $\hat{u}$ is the subgroup H of $\mathrm{O}(N)$ that leaves $\hat{u}$ invariant, i.e. $h\hat{u} = \hat{u}$, $\forall h \in H$.

[7] Given a subgroup H of a group G (usually written as $H < G$), for $g \in G$, the *coset* gH (left coset), is defined as $gH := \{gh | h \in H\}$. Belonging to the same (left) coset is an equivalence relation, i.e. x and $y \in G$ are equivalent if $x^{-1}y \in H$. The equivalence classes of this relation are the (left) cosets. The *coset space* G/H is defined as the set of all cosets of H in G, $G/H := \{gH | g \in G\}$, i.e. the coset space is the set of all the equivalence classes of the previous equivalence relation. In general, the coset space is not a group unless H is a normal subgroup in G (H is a normal subgroup if $\forall h \in H$ and $\forall g \in G$, $ghg^{-1} \in H$, this is usually written as $H \lhd G$). If G/H is a group we call it the *quotient group* of G by H.

[8] A brief introduction to homotopy groups can be found in [37].

[9] The homotopy transformations conserve the topological charge. Furthermore, each homotopy can be identified by a continuous path in space-time [38]. Thus, all physical paths conserve the topological charge.

[10] The change from time to Euclidean time is obtained after performing a $\pi/2$ rotation in time in the complex time plane, known as *Wick rotation*, $t_E := it$, and carrying out the corresponding analytical continuations to the theory.

otherwise $t_E/\hbar = 1/(k_B T) = \beta$). From Eq. (2.24) (with $F = 1$, $d-1$ spatial and 1 temporal dimensions) we have

$$S_{\mathrm{E}}[\vec{\sigma}] = \frac{1}{2}\int_0^\beta dt_E \int d^{d-1}x\, \partial_\mu \vec{\sigma}(x) \cdot \partial_\mu \vec{\sigma}(x). \tag{2.28}$$

Next, we assume high temperature ($\beta \gtrsim 0$); in such a case the Lagrangian is approximately constant in t_E for typical low energy configurations. With this approximation, we can proceed to

$$S_{\mathrm{E}}[\vec{\sigma}] = \frac{1}{2}\beta \int d^{d-1}x\, \partial_i \vec{\sigma}(x) \cdot \partial_i \vec{\sigma}(x), \tag{2.29}$$

where i runs over the $d-1$ spatial dimensions. This is a *high temperature dimensional reduction* from a d-dimensional to a $(d-1)$-dimensional theory, for more details see [39]. Since the Euclidean time dependency is only contained in the parameter β, this is a static model.

2.2.3 Lattice regularization

Now we replace the continuous space $\mathbb{R}^{d-1}$ of (2.29) by a discrete cubic space lattice Λ. Given $a \in \mathbb{R}$ and $L \in \mathbb{N}$, we have

$$\Lambda := \{x \,|\, x/a \in [0, L-1]^{d-1}\}, \tag{2.30}$$

where a is the lattice spacing and L are the lattice sites per edge, $\Lambda \subset a\mathbb{Z}^{d-1}$. The volume of Λ is given by

$$V = (aL)^3. \tag{2.31}$$

Following the standard notation of lattice spin models from now on we will put the coordinates x as a subscript,

$$\vec{\sigma}_x \equiv \vec{\sigma}(x). \tag{2.32}$$

We refer to $\vec{\sigma}_x$ as a *classical spin* or simply as spin in the context of the O(N) non-linear σ model. We suppose periodic boundary conditions, then $\forall x \in \Lambda$ and for each standard unit vector e_i in $\mathbb{R}^{d-1}$,

$$\vec{\sigma}_{x+aLe_i} = \vec{\sigma}_x. \tag{2.33}$$

We must replace derivatives and integrals in (2.29) with finite differences and sums. The standard choice for finite differences is

$$\partial_i \vec{\sigma}_x \underset{\text{lat}}{\longrightarrow} \frac{\vec{\sigma}_{x+ae_i} - \vec{\sigma}_x}{a}, \tag{2.34}$$

therefore,

$$\partial_i \vec{\sigma}_x \cdot \partial_i \vec{\sigma}_x \underset{\text{lat}}{\longrightarrow} \frac{2}{a^2}\sum_{i=1}^{d-1}\left(1 - \vec{\sigma}_{x+ae_i} \cdot \vec{\sigma}_x\right). \tag{2.35}$$

Since a constant is meaningless in the action, we can drop the 1 in the sum. To discretize the integrals we replace,

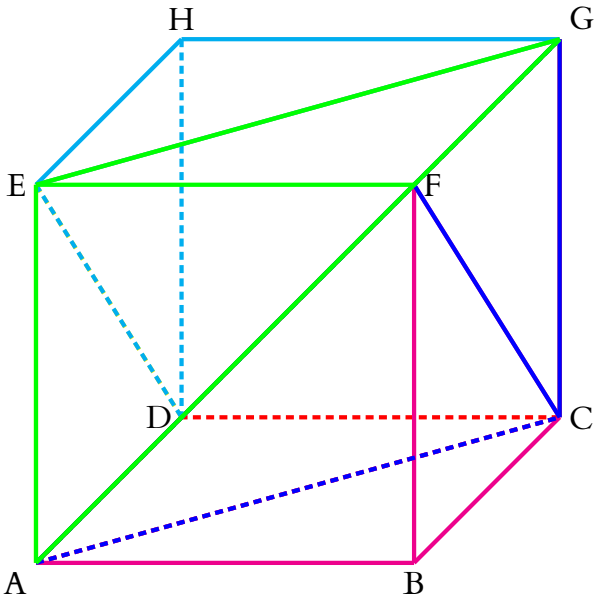

Figure 2.1: *Division of a unit cube of the lattice into six tetrahedra.*

$$\int d^{d-1}x \underset{\text{lat}}{\longrightarrow} a^{d-1} \sum_{x\in\Lambda}. \tag{2.36}$$

After performing these discretizations in (2.29), we have the following lattice regularized Euclidean action,

$$S_{\text{E,reg}}[\vec{\sigma}] = -a^{d-3}\beta_{\text{lat}} \sum_{x\in\Lambda} \sum_{i=1}^{d-1} \vec{\sigma}_{x+ae_i} \cdot \vec{\sigma}_x. \tag{2.37}$$

2.3 Topological charge on the lattice

In the lattice regularized theory we can continuously deform any field configuration into any other. Thus, strictly speaking, the lattice regularized theory is topologically trivial.

The highly important topological properties of the low energy QCD have incited the definition of a topological charge Q on the lattice. One such definition is geometric [40]. With this definition, in a field with periodic boundary conditions, the topological charge Q is an integer (except for a measure zero subset of the field configurations). In this work we extend the geometric definition to the 3d O(4) non-linear σ model, as argued in [15]. The inclusion of the topological charge to the 3d O(4) non-linear σ model has been studied in recent theses [41; 31].

On a 3d cubic lattice Λ (defined in Eq. (2.30)) with lattice spacing $a = 1$, there are L^3 unit cubes, each formed by 8 lattice sites. We divide the unit cubes of the lattice into six non-regular tetrahedra, as shown in fig. 2.1, each tetrahedron is shown separately in fig. 2.2. In the 3d O(4) non-linear σ model each set of spins at the vertices of one of those tetrahedra generates a *spherical tetrahedron* on the surface of S^3. The edges of a spherical tetrahedron are minimum distance curves over S^3 connecting the spins at the vertices of the spherical tetrahedron.

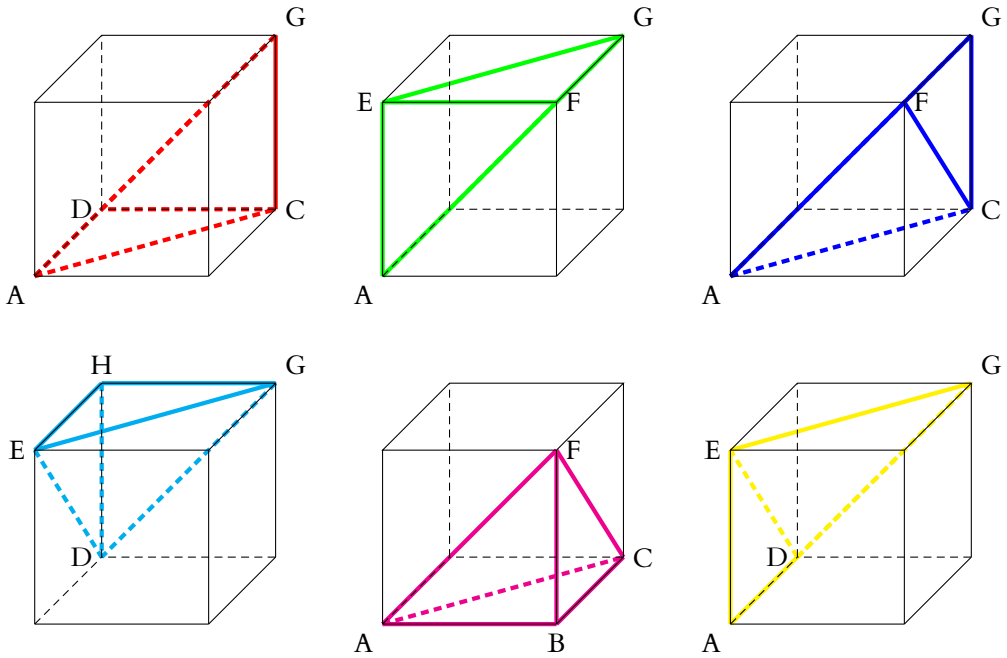

Figure 2.2: *Each of the tetrahedra into which the lattice unit cubes are split.*

For brevity we will refer to the spherical tetrahedra generated by the spins $\{\vec{\sigma}_i, \vec{\sigma}_j, \vec{\sigma}_k, \vec{\sigma}_l\}_n$ at the vertices of the mth lattice tetrahedron (fig. 2.2) from the nth unit cube as T_{nm}, $1 \leq n \leq L^3$ and $1 \leq m \leq 6$. Following the notation in figure 2.2, these tetrahedra are

$$\begin{aligned}
T_{n1} &:= \mathrm{T}(\{\vec{\sigma}_D, \vec{\sigma}_G, \vec{\sigma}_C, \vec{\sigma}_A\}_n), \\
T_{n2} &:= \mathrm{T}(\{\vec{\sigma}_F, \vec{\sigma}_G, \vec{\sigma}_E, \vec{\sigma}_A\}_n), \\
T_{n3} &:= \mathrm{T}(\{\vec{\sigma}_A, \vec{\sigma}_F, \vec{\sigma}_G, \vec{\sigma}_C\}_n), \\
T_{n4} &:= \mathrm{T}(\{\vec{\sigma}_D, \vec{\sigma}_G, \vec{\sigma}_E, \vec{\sigma}_H\}_n), \\
T_{n5} &:= \mathrm{T}(\{\vec{\sigma}_C, \vec{\sigma}_A, \vec{\sigma}_F, \vec{\sigma}_B\}_n), \\
T_{n6} &:= \mathrm{T}(\{\vec{\sigma}_A, \vec{\sigma}_D, \vec{\sigma}_G, \vec{\sigma}_E\}_n),
\end{aligned} \tag{2.38}$$

where $\mathrm{T}(\{\vec{\sigma}_i, \vec{\sigma}_j, \vec{\sigma}_k, \vec{\sigma}_l\}_n)$ denotes the spherical tetrahedron generated when we connect with minimum distance curves in S^3 the spins $\{\vec{\sigma}_i, \vec{\sigma}_j, \vec{\sigma}_k, \vec{\sigma}_l\}_n$. One should not confuse the lattice tetrahedra, shown in fig. 2.2, with the spherical tetrahedra T_{nm}, generated by the spins at the vertices of the lattice tetrahedra.

Extending the explicit formula for the topological charge given in [40], the topological charge in the 3d O(4) non-linear σ model is given by the sum of all the oriented volumes of the spherical tetrahedra T_{nm}. The volume of a spherical tetrahedron is given by the *Murakami formula* and the orientation depends on the parity of the permutation of the vertices.

2.3.1 Murakami formula

Let T_{nm} be a spherical tetrahedron on S^3 with edges $e_1, e_2, \ldots, e_6$ and edge lengths $l_1, l_2, \ldots, l_6$; a schematic representation of T_{nm} is shown in fig. 2.3 . Let

$$b_j = -e^{il_j} \quad \text{for } j = 1, 2, \ldots, 6 \tag{2.39}$$

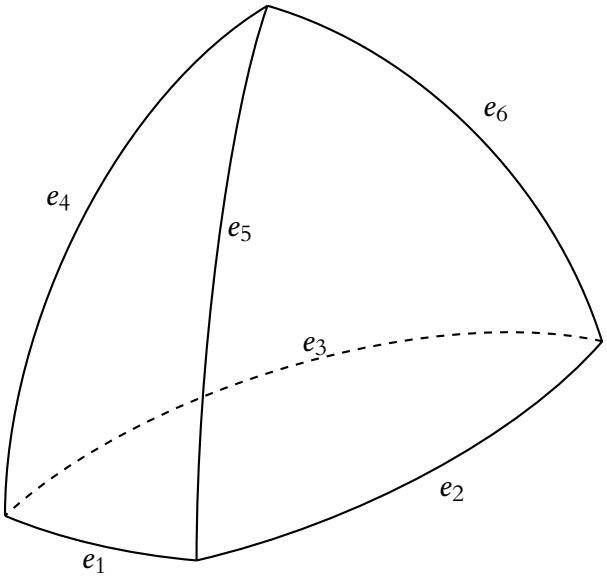

Figure 2.3: *Schematic representation of T_{nm}. The spherical tetrahedron is located in S^3 and therefore its edges are minimum distance curves in S^3.*

and

$$\begin{aligned} \mathrm{L}(b_1,b_2,b_3,b_4,b_5,b_6,z) = \frac{1}{2}\Bigg(&\mathrm{Li}_2(z) + \mathrm{Li}_2(b_1b_2b_4b_5z) + \mathrm{Li}_2(b_1b_3b_4b_6z) \\ &+\mathrm{Li}_2(b_2b_3b_5b_6z) - \mathrm{Li}_2(-b_1b_2b_3z) - \mathrm{Li}_2(-b_1b_5b_6z) \\ &-\mathrm{Li}_2(-b_2b_4b_6z) - \mathrm{Li}_2(-b_3b_4b_5z) + \sum_{j=1}^{3}\mathrm{Log}(b_j)\mathrm{Log}(b_{j+3})\Bigg), \end{aligned} \tag{2.40}$$

where $z \in \mathbb{C}$, $\mathrm{Log}(z)$ is the principal branch of the complex logarithm and $\mathrm{Li}_2(z)$ is the dilogarithm function. $\mathrm{Li}_2(z)$ can be defined as an infinite series [42],

$$\mathrm{Li}_2(z) := \sum_{k=1}^{\infty}\frac{z^k}{k^2}, \quad \text{for } |z| \leq 1. \tag{2.41}$$

Let

$$z_0 = \frac{-q_1 + \sqrt{q_1^2 - 4q_0q_2}}{2q_2}, \tag{2.42}$$

with

$$\begin{aligned} q_0 = &b_1^{-1}b_4^{-1} + b_2^{-1}b_5^{-1} + b_3^{-1}b_6^{-1} + b_1^{-1}b_2^{-1}b_3^{-1} + b_1^{-1}b_5^{-1}b_6^{-1} \\ &+b_2^{-1}b_4^{-1}b_6^{-1} + b_3^{-1}b_4^{-1}b_5^{-1} + b_1^{-1}b_2^{-1}b_3^{-1}b_4^{-1}b_5^{-1}b_6^{-1}, \end{aligned} \tag{2.43}$$

$$q_1 = -(b1 - b_1^{-1})(b_4 - b_4^{-1}) - (b_2 - b_2^{-1}) - (b_3 - b_3^{-1})(b_6 - b_6^{-1}), \tag{2.44}$$

and

$$q_2 = b_1b_4 + b_2b_5 + b_3b_6 + b_1b_2b_3 + b_1b_5b_6 + b_2b_4b_6 + b_3b_4b_5 + b_1b_2b_3b_4b_5b_6. \tag{2.45}$$

The volume of T_{nm} is given by [43],

$$\mathrm{Vol}(T_{nm}) = \left(\mathrm{Re}(L(b_1, b_2, \ldots, b_6, z_0)) - \frac{1}{2}\pi^2 - \pi \arg(-q_2) - \sum_{j=1}^{6} l_j \left. \frac{\partial \mathrm{Re}(L(b_1, b_2, \ldots, b_6, z_0))}{\partial l_j} \right|_{z=z_0} \right) \mod 2\pi^2. \tag{2.46}$$

2.3.2 First formula for the topological charge

Now that we know how to calculate the volume of a spherical tetrahedron, we can give an explicit formula for the topological charge Q on the lattice regularized 3d O(4) non-linear σ model,

$$Q[\vec{\sigma}] = \sum_{n=1}^{L^3} \sum_{m=1}^{6} \mathrm{sgnVol}(T_{nm}), \tag{2.47}$$

where $\mathrm{sgnVol}(T_{nm})$ denotes the oriented volume of the spherical tetrahedron T_{nm}. The volume of the spherical tetrahedron is given by Eq. (2.46) and the sign of this volume is

$$\mathrm{sgn}(T_{nm}) = \mathrm{sgn}(\det(\vec{\sigma}_i \vec{\sigma}_j \vec{\sigma}_k \vec{\sigma}_l)), \tag{2.48}$$

where $(\vec{\sigma}_i \vec{\sigma}_j \vec{\sigma}_k \vec{\sigma}_l)$ is the matrix that has the vector spins that generate T_{nm} as columns. Therefore,

$$\mathrm{sgnVol}(T_{nm}) := \mathrm{sgn}(T_{nm})\mathrm{Vol}(T_{nm}). \tag{2.49}$$

2.3.3 Second formula for the topological charge

The calculation of the topological charge by Eq. (2.47) is a computationally expensive task. Another way to compute the topological charge is based on the geometrical interpretation of the topological charge as the winding number of the spins on the lattice around S^3.

To give an intuitive idea of how the winding number can be calculated, let us look to the 1d O(2) non-linear σ model. The 1d lattice is $\Lambda = \{x \,|\, x/a \in [0, L-1]\}$, and $\vec{\sigma}_i \in S^1$. Let $\vec{\sigma}_{\mathrm{ref}}$ be a reference point on S^1. The winding number is determined by the number of times the reference point is contained in the shortest arc generated by two nearest neighbors spins (the cases where the winding number is not obtained in this way fall into a measure zero set, e.g. when two nearest neighbors spins are separated by a π angle). If we take counterclockwise as the positive direction, each positive arc containing the reference point contributes with +1 to the winding number and each negative arc containing the reference point contributes with -1 to the winding number.

An example of a lattice configuration is shown in fig. 2.4. For the given $\vec{\sigma}_{\mathrm{ref}}$, only the pairs of spins $\vec{\sigma}_2$ and $\vec{\sigma}_3$, $\vec{\sigma}_3$ and $\vec{\sigma}_4$, $\vec{\sigma}_4$ and $\vec{\sigma}_5$, and $\vec{\sigma}_{11}$ and $\vec{\sigma}_0$ contribute to the total topological charge. The spins $\vec{\sigma}_2$ and $\vec{\sigma}_3$ generate a positive arc, $\vec{\sigma}_3$ and $\vec{\sigma}_4$ a negative arc, $\vec{\sigma}_4$ and $\vec{\sigma}_5$ a positive arc and $\vec{\sigma}_{11}$ and $\vec{\sigma}_0$ a positive arc. Therefore, the lattice configuration shown in 2.4 has winding number $Q[\vec{\sigma}] = 2$.

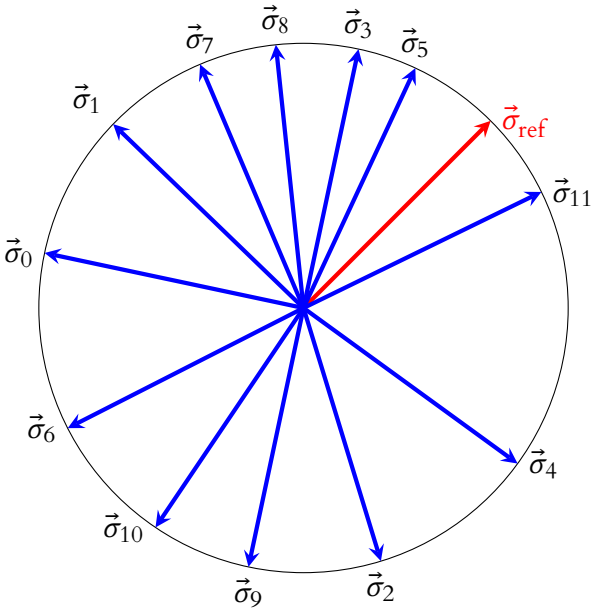

Figure 2.4: *An $L = 12$ field configuration of a 1d O(2) lattice regularized non-linear σ model with periodic boundary conditions. The topological charge (winding number) of this configuration is $Q[\vec{\sigma}] = 2$.*

Any two non-zero and non-parallel vectors, $\vec{\sigma}_i$ and $\vec{\sigma}_j$ in $\mathbb{R}^2$, form a basis for $\mathbb{R}^2$. The reference vector is a linear combination of the basis,

$$\vec{\sigma}_{\text{ref}} = c_1\vec{\sigma}_i + c_2\vec{\sigma}_j. \tag{2.50}$$

The vector $\vec{\sigma}_{\text{ref}}$ is contained in the shortest arc connecting $\vec{\sigma}_i$ and $\vec{\sigma}_j$ if and only if c_1 and $c_2 \geq 0$. Therefore, the winding number is

$$Q[\vec{\sigma}] = \sum_{i=0}^{L-1} \text{sgn}(l(\{\vec{\sigma}_i, \vec{\sigma}_{i+1}\}))f(\{\vec{\sigma}_i, \vec{\sigma}_{i+1}\}), \tag{2.51}$$

where $\text{sgn}(l(\{\vec{\sigma}_i, \vec{\sigma}_{i+1}\}))$ denotes the sign of the shortest oriented arc connecting $\vec{\sigma}_i$ and $\vec{\sigma}_{i+1}$, and f is

$$f(\{\vec{\sigma}_i, \vec{\sigma}_{i+1}\}) = \begin{cases} 1 & \text{if } c_1 \text{ and } c_2 > 0 \\ 0 & \text{otherwise,} \end{cases} \tag{2.52}$$

where c_1 and c_2 are the factors of the linear combination (2.50) in the basis $\{\vec{\sigma}_i, \vec{\sigma}_{i+1}\}$.

With the help of the previous example it is easy to extrapolate the winding number to the 3d O(4) case. Let $\vec{\sigma}_{\text{ref}}$ be a reference point on S^3. Let $\vec{\sigma}_i$, $\vec{\sigma}_j$, $\vec{\sigma}_k$ and $\vec{\sigma}_l$ form a basis for $\mathbb{R}^4$, then

$$\vec{\sigma}_{\text{ref}} = c_1\vec{\sigma}_i + c_2\vec{\sigma}_j + c_3\vec{\sigma}_k + c_4\vec{\sigma}_l. \tag{2.53}$$

The winding number Q on the lattice regularized 3d O(4) non-linear σ model is

$$Q[\vec{\sigma}] = \sum_{n=1}^{L^3} \sum_{m=1}^{6} \text{sgn}(T_{nm})f(\{\vec{\sigma}_i, \vec{\sigma}_j, \vec{\sigma}_k, \vec{\sigma}_l\}_n), \tag{2.54}$$

where $\{\vec{\sigma}_i, \vec{\sigma}_j, \vec{\sigma}_k, \vec{\sigma}_l\}_n$ are the spins that generate the spherical tetrahedron T_{nm}, see Eqs. (2.38) and fig. 2.2, and f is

$$f(\{\vec{\sigma}_i, \vec{\sigma}_j, \vec{\sigma}_k, \vec{\sigma}_l\}_n) = \begin{cases} 1 & \text{if } c_1, c_2, c_3 \text{ and } c_4 > 0 \\ 0 & \text{otherwise.} \end{cases} \tag{2.55}$$

The constants $c_1, \ldots, c_4$ are the factors of the linear combination (2.53) in the basis $\{\vec{\sigma}_i, \vec{\sigma}_j, \vec{\sigma}_k, \vec{\sigma}_l\}_n$ (the cases in which $\{\vec{\sigma}_i, \vec{\sigma}_j, \vec{\sigma}_k, \vec{\sigma}_l\}_n$ is not a basis are in a measure zero set).

The second explicit equation for the topological charge (2.54) has the advantage over the first explicit equation (2.47) that it is a computationally cheaper task. The first explicit equation has the advantage over the second explicit equation that the internal sums,

$$q_n[\vec{\sigma}] = \sum_{m=1}^{6} \text{sgnVol}(T_{nm}), \tag{2.56}$$

are the topological charge densities, a quantity that cannot be calculated with the second explicit equation for the topological charge.

2.4 Chemical potential

In the Hamiltonian formulation $\hat{H}$ and $\hat{Q}$ are operators. For a general system with some Hamiltonian $\hat{H}$ and a conserved charge $\hat{Q}$ the operators $\hat{H}$ and $\hat{Q}$ commute,

$$[\hat{H}, \hat{Q}] = -i\frac{d\hat{Q}}{dt} = 0, \tag{2.57}$$

so we can find a basis in which $\hat{H}$ and $\hat{Q}$ have simultaneous eigenstates. Then, we can write a new Hamiltonian [44],

$$\hat{H}' = \hat{H} - \mu\hat{Q}, \tag{2.58}$$

where μ will be interpreted as a chemical potential.

Applying this recipe to the $(d-1)$-dimensional O(d) non-linear σ model we can add a chemical potential term to the Hamilton function,

$$H[\vec{\sigma}] = -a^{d-3} \sum_{x\in\Lambda} \sum_{i=1}^{d-1} \vec{\sigma}_{x+e_i} \cdot \vec{\sigma}_x - \mu_B Q[\vec{\sigma}]. \tag{2.59}$$

Then, the Euclidean action of this model is

$$S_{\text{E}}[\vec{\sigma}] = \beta_{\text{lat}} \left(- \sum_{x\in\Lambda} \sum_{i=1}^{d-1} \vec{\sigma}_{x+ae_i} \cdot \vec{\sigma}_x - \mu_{B,\text{lat}} Q[\vec{\sigma}] \right). \tag{2.60}$$

2.5 Statistical mechanics approach

In the Euclidean formulation, the quantum evolution operator $\exp(-i\hat{H}t/\hbar)$ is carried by analytical continuation to the quantum statistical operator $\exp(-\beta\hat{H})$ (the Euclidean time transformation is $it/\hbar \to \beta$).

In this formulation, the partition function $Z(\beta)$ [11],

$$Z(\beta) := \mathrm{Tr}(e^{-\beta\hat{H}}) = \int [d\vec{\sigma}] e^{-\beta H[\vec{\sigma}]}, \tag{2.61}$$

plays the same role as the partition function in statistical mechanics [45]. With the partition function we can assign a statistical weight to each field configuration,

$$p[\vec{\sigma}] := \frac{e^{-\beta H[\vec{\sigma}]}}{Z}, \tag{2.62}$$

formally this is a probability density function. The partition function is the normalization factor of the probability distribution,

$$\int [d\vec{\sigma}] p[\vec{\sigma}] = \frac{1}{Z} \int [d\vec{\sigma}] e^{-\beta H[\vec{\sigma}]} = 1. \tag{2.63}$$

We can calculate expectation values in the same way as in statistical mechanics. Let $\mathcal{O}[\vec{\sigma}]$ be an observable, then [45]

$$\langle \mathcal{O} \rangle = \frac{\int [d\vec{\sigma}] e^{-\beta H[\vec{\sigma}]} \mathcal{O}[\vec{\sigma}]}{Z}. \tag{2.64}$$

2.6 3d O(4) model with chemical potential

Finally we arrive to the model used in this work, the 3d O(4) non-linear σ model with chemical potential. The Euclidean action is

$$S_{\mathrm{E}}[\vec{\sigma}] = \beta_{\mathrm{lat}} \left(- \sum_{x \in \Lambda} \sum_{i=1}^{3} \vec{\sigma}_{x+e_i} \cdot \vec{\sigma}_x - \mu_{B,\mathrm{lat}} Q[\vec{\sigma}] \right). \tag{2.65}$$

The Hamilton function reads

$$H[\vec{\sigma}] = - \sum_{x \in \Lambda} \sum_{i=1}^{3} \vec{\sigma}_{x+e_i} \cdot \vec{\sigma}_x - \mu_{B,\mathrm{lat}} Q[\vec{\sigma}]. \tag{2.66}$$

In Eqs. (2.65) and (2.66), we used lattice units, i.e. lattice spacing $a = 1$. As in the Skyrme model, Sec. 2.1.1, in this bosonic theory the topological charge Q represents the baryon number [26]. The chemical potential $\mu_{B,\mathrm{lat}}$ is the decrease in energy when adding a baryon or the increase in energy when adding an anti-baryon.

Comparing Eq. (2.65) with Eq. (2.19) we see how to obtain the physical values of β_{lat} and $\mu_{B,\mathrm{lat}}$,

$$\beta_{\mathrm{lat}} = \beta F_\pi^2 a \tag{2.67}$$

$$\mu_{B,\mathrm{lat}} = \frac{\mu_B}{F_\pi^2 a}. \tag{2.68}$$

The value of the pion decay constant ($F_\pi = 92.1(8)$ MeV [16]) is not a reliable constant in dimensional reduced theories. Instead, with the $\mu_B = 0$ value of critical temperature (see Chap. 3) $T_c \approx 155$ MeV [46] and the lattice value $\beta_{c,\mathrm{lat}} = 0.93590$ [47], we can conjecture the physical values β and μ_{B} [48],

$$\beta = \frac{\beta_c}{\beta_{c,\mathrm{lat}}}\beta_{\mathrm{lat}} \approx 0.007\ \mathrm{MeV}^{-1}\,\beta_{\mathrm{lat}} \tag{2.69}$$

$$\mu_B = \frac{\beta_{c,\mathrm{lat}}}{\beta_c}\mu_{B,\mathrm{lat}} \approx 145\ \mathrm{MeV}\,\mu_{B,\mathrm{lat}}. \tag{2.70}$$

The physical values of the lattice spacing can be conjectured similarly,

$$a = \frac{\beta_c}{\beta_{c,\mathrm{lat}}}a_{\mathrm{lat}} \approx 0.007\ \mathrm{MeV}^{-1}\,a_{\mathrm{lat}}. \tag{2.71}$$

The equivalence $1\ \mathrm{fm} = (197.3\ \mathrm{MeV})^{-1}$ (in natural units) allow us to calculate the lattice spacing in fermis,

$$a = 197.3\ \mathrm{MeV}\frac{\beta_c}{\beta_{c,\mathrm{lat}}}a_{\mathrm{lat}} \approx 1.36\ \mathrm{fm}\,a_{\mathrm{lat}}. \tag{2.72}$$

3 Phase Transitions and Critical Phenomena

In this chapter we review some of the basic concepts of phase transitions and critical phenomena. Definitions of the observables measured in this work are also given.

3.1 Classification of phase transitions

There are several types of phase transitions in nature; we focus in the Ehrenferst classification (a compilation of the phase transitions classifications can be found in [49]). In this classification, the first and second order phase transitions are the most recurrent. The first order phase transitions are marked changes of thermodynamic quantities occurring at specific conditions, e.g. the abrupt change of the density of water at 1 atm and 0 °C, Fig. 3.1. First order transitions often form continuous lines known as *phase boundaries*, as in the phase diagram of water, Fig. 3.2. The second order transitions are smoother changes and take place at *critical points*, e.g. the critical point of the liquid-gas boundary in the phase diagram of water (at *critical temperature* T_c = 373.946 °C and *critical pressure* P_c = 217.75 atm, Fig. 3.2) and the Curie temperature of iron (at critical temperature T_c = 769.85 °C and *critical external magnetic field* $\vec{B}_c = \vec{0}$).

Many phase transitions are characterized by two phases: a symmetric phase known as *ordered phase* and a lower-symmetry phase known as *disordered phase*. An example of these phases are the non-zero (ordered) and zero (disordered) magnetization phases of a ferromagnetic system. Theses phases let us introduce the *order parameter*, a thermodynamic quantity that is non-zero and finite on the ordered phase and zero on the disordered phase. In the case of the ferromagnetic systems (as the classical spin models) the order parameter is the magnetization M.

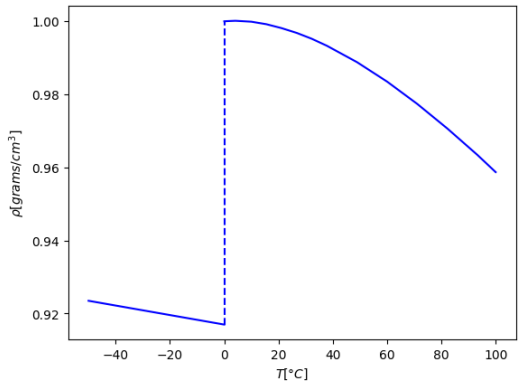

Figure 3.1: *Plot of the density (ρ) of water, as a function of temperature (T), capturing the phase transition at 1 atm and 0 °C [50; 51]. This type of change in a thermodynamic quantity is characteristic of the first order phase transitions.*

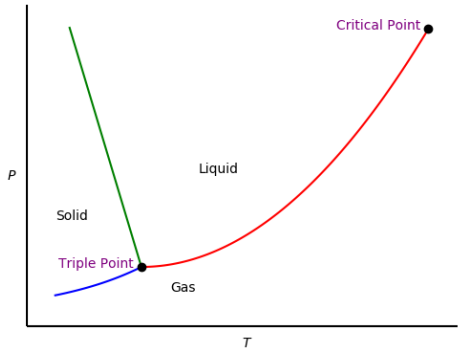

Figure 3.2: *Scheme of the phase diagram of water (not to scale). The colored lines represent first order phase transition. In the triple point the solid, liquid and gaseous phases of water coexist. The critical point at a temperature of 373.946 °C and a pressure of 217.75 atm is a second order phase transition.*

In *first order phase transitions*, at least one of the first derivatives of free energy is discontinuous. Furthermore, the derivatives of discontinuous quantities are δ-type divergences. In *second order phase transitions*, the first derivatives of free energy are continuous and the second derivatives are discontinuous or divergent. The physics related to second order phase transitions is known as *critical phenomena*.

3.2 Free energy and derivatives

The *free energy* can be obtained from the partition function $Z(\beta)$,

$$F(\beta) = -\frac{1}{\beta}\ln(Z(\beta)). \tag{3.1}$$

This is an extensive quantity, whereas the *free energy density* is an intensive quantity,

$$f(\beta) = -\frac{1}{\beta V}\ln Z(\beta). \tag{3.2}$$

We are interested in two first derivatives: the *magnetization*,

$$M(\beta) := -\left(\frac{\partial F}{\partial B}\right)_\beta, \tag{3.3}$$

and the *energy*,

$$E(\beta) := -\frac{\partial \ln Z(\beta)}{\partial \beta}, \tag{3.4}$$

where B is the magnitude of an external magnetic field.

The following are two of the derivatives of these quantities: the *magnetic susceptibility*,

$$\chi_M(\beta) := \frac{1}{V}\left(\frac{\partial M}{\partial B}\right)_\beta = -\left(\frac{\partial^2 f}{\partial B^2}\right)_\beta \tag{3.5}$$

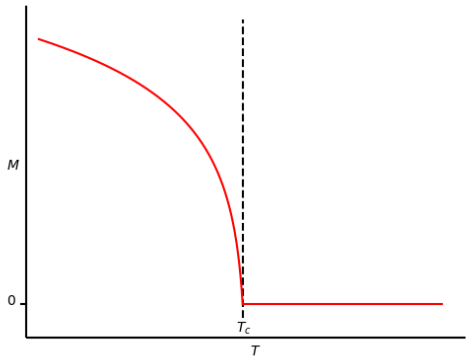

Figure 3.3: *Typical behavior of the order parameter M near T_c in a second order phase transition. The red horizontal line is the zero magnetization phase.*

and the *specific heat*,

$$c_V(\beta) := \frac{1}{V}\frac{\partial E}{\partial T} = -T\frac{\partial^2 f}{\partial T^2}. \tag{3.6}$$

3.3 Critical exponents

In this section we will introduce the critical exponents phenomenologically in a ferromagnetic system at $B = 0$. This section refers to a second order phase transition, which occurs in the infinite volume limit.

We define the *reduced temperature* as

$$t := \frac{T_c - T}{T_c}. \tag{3.7}$$

If we approach T_c from below, the magnetization behaves as [52; 53]

$$M(T)|_{T\lesssim T_c, B=0} \propto t^{\beta}. \tag{3.8}$$

This expression introduces the critical exponent β. To avoid confusion with the inverse temperature, we will be clear when we refer to the critical exponent β. The behavior of M is as observed in Fig. 3.3.

Near T_c, the magnetic susceptibility scales according to

$$\chi_M(T)|_{T\approx T_c, B=0} \propto |t|^{-\gamma}, \tag{3.9}$$

where γ is another critical exponent. The behavior of the magnetic susceptibility and specific heat is as observed in Fig. 3.4. The specific heat near T_c behaves as

$$c_V(T)|_{T\approx T_c, B=0} \propto |t|^{-\alpha}, \tag{3.10}$$

where α is a critical exponent.

In classical spin models (see Chap. 2), another important quantity is the *connected correlation function*,

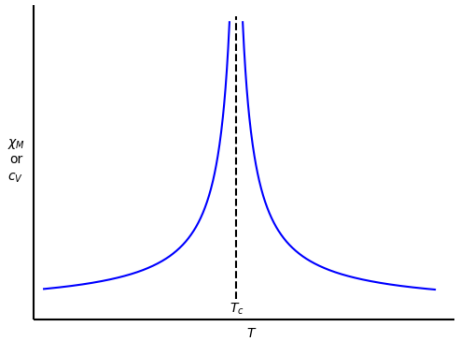

Figure 3.4: *Typical behavior of the susceptibility of the order parameter χ_M and the specific heat c_V near T_c in a second order phase transition.*

$$G(x, x') := \langle \vec{\sigma}_x \cdot \vec{\sigma}_{x'} \rangle - \langle \vec{\sigma}_x \rangle \cdot \langle \vec{\sigma}_{x'} \rangle. \tag{3.11}$$

At large distances ($|x - x'| \to \infty$) and $T > T_c$, G decays according to

$$G(x, x') \propto e^{-\frac{|x-x'|}{\xi(T)}}, \tag{3.12}$$

and at $T = T_c$,

$$G(x, x') \propto |x - x'|^{-(d-2+\eta)}, \tag{3.13}$$

where d is the spatial dimension of the model and η is a critical exponent.

The Eq. (3.12) introduces the *correlation length* $\xi(T)$, it is the spatial length within which the spins are highly correlated. Intuitively, within the correlation length it is particularly probable to find approximately parallel spins. Close to T_c, ξ scales as

$$\xi(T) \propto |t|^{-\nu}. \tag{3.14}$$

Typical values for these critical exponents are [39; 53; 54]

$$\alpha \gtrsim 0, \qquad \beta \approx 1/3, \qquad \gamma \approx 4/3, \qquad \nu \approx 1/2, \qquad \eta \approx 0. \tag{3.15}$$

Not all the critical exponents are independent, their dependence is summarized in the *scaling laws*, here we show three of them [52],

$$\begin{aligned} \alpha + 2\beta + \gamma &= 2 \\ 2 - d\nu &= \alpha \\ \nu(2 - \eta) &= \gamma, \end{aligned} \tag{3.16}$$

where d is the spatial dimension of the model.

A *universality class* is a set of critical models that have common features. Universality classes arise within the framework of the renormalization group theory, see for example [39; 52; 55]. A universality class has *universal quantities* shared by all models of the class, e.g. critical exponents. The universal quantities of a universality class depend on finite relevant variables, e.g. the spin

coupling constants in the 2d Ising model [56]. The universality classes allow us to calculate the universal quantities using simple or toy models rather than complicated or realistic ones. It is conjectured that the critical points of the 3d O(4) model with chemical potential and the nonzero baryon density QCD with two flavors in the chiral limit are in the same universality class [15].

3.4 Phase transitions and finite size lattices

In a finite volume some artifacts known as *finite size effects* are always present. The finite volume sets bounds on observables, thus observables cannot diverge in finite volumes. Furthermore, discontinuities are pronounced slopes. Both effects cause that in a lattice regularized theory on a finite volume, we cannot always distinguish between first and second order transitions.

3.4.1 Finite size scaling for second order phase transitions

On finite size lattices near a second order transition, the behavior of the observables is not the one presented in Sec. 3.3. The scaling behaviors for ferromagnetic systems at $B = 0$ on finite lattices of size L^d (see Eq. (2.30)) are given by [39; 52]

$$M(T_c) \propto L^{-\beta/\nu}, \tag{3.17}$$

$$\chi_M(T_c) \propto L^{\gamma/\nu}, \tag{3.18}$$

$$c_V(T_c) \propto L^{\alpha/\nu}, \tag{3.19}$$

$$\xi(T_c) \propto L. \tag{3.20}$$

The critical exponents α, β, γ and ν are the same as in Sec. 3.3. These relationships are valid only on large volume lattices at T_c.

The correlation length is the usual intrinsic scale, then, the finite size effects are significant when [52; 57]

$$\xi(T)_\infty \gtrsim O(L), \tag{3.21}$$

where $\xi(T)_\infty$ is the correlation length in the thermodynamic limit.

The maximum of the expectation value of an observable $\langle \mathcal{O} \rangle$ on finite volumes can be shifted away from T_c,

$$T_{\max} = T_{\max}(L, \mathcal{O}), \tag{3.22}$$

i.e. the position of the maximum of $\langle \mathcal{O} \rangle$ depends on L and on $\mathcal{O}$ itself. We refer to $T_{\max}$ as the *pseudo critical temperature* of observable $\mathcal{O}$ in a volume L^d. In large volumes, the displacement of $T_{\max}$ decays like [39]

$$T_{\max} - T_c \propto L^{-1/\nu}. \tag{3.23}$$

3.4.2 First order phase transitions and finite lattices

Only in the infinite volume limit we can be sure whether or not that a system has a phase transition and its order. On large volume lattices we can infer a first order phase transition if some of the following qualitative phenomena take place [39; 57],

- Discontinuities in the infinite volume limit are pronounced slopes in finite volumes.

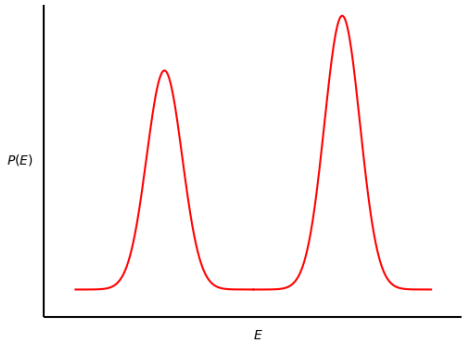

Figure 3.5: *Example for the energy probability distribution $P(E)$ in a vicinity of a first order phase transition, where E is energy.*

- After some simulation time, ordered and disordered field configurations reach different equilibrium states corresponding to the ordered and disordered phases. Whereas in a second order transition, the equilibrium state is unique.
- Tunneling occurs between ordered and disordered phases. There is a back and forth movement between two equilibrium states in the history of energy or another observable of interest.
- The energy probability distribution is sharply peaked at two values corresponding to the ordered and disordered phases, see Fig. 3.5. This is an expression of tunneling and *metastability*.
- The system presents *hysteresis effects*.
- The behavior of the observables near a first order phase transition is not the one of the second order phase transition. Inconsistent results for critical exponents and scaling functions are obtained in a first order transition.

If these criteria are not met we cannot discard a first order phase transition, it may be a sign that our volume is not large enough.

3.5 Observables

In this section we summarize the definitions of the observables measured in this work.

The (total) magnetization of a lattice configuration is defined by

$$\vec{M}[\vec{\sigma}] = \sum_{x \in \Lambda} \vec{\sigma}_x. \tag{3.24}$$

The magnetization is always zero in systems with Hamilton function which is symmetric under $O(N)$ transformations and in the absence of an external magnetic field,

$$\langle \vec{M}[\vec{\sigma}] \rangle = \vec{0}. \tag{3.25}$$

So, the actual order parameter must be constructed with some care. The order parameter on finite volume lattices is given by [58]

$$M(\beta_{\text{lat}}) = \langle |\vec{M}[\vec{\sigma}]| \rangle. \tag{3.26}$$

The order parameter M is always positive,

$$\langle|\vec{M}[\vec{\sigma}]|\rangle > 0. \tag{3.27}$$

In the disordered phase it is zero (in infinite volume), thus, M is suitable to be an order parameter.

The *magnetization density* is

$$m(\beta_{\text{lat}}) = \frac{1}{L^3}\langle|\vec{M}[\vec{\sigma}]|\rangle. \tag{3.28}$$

The *energy density* is

$$\epsilon(\beta_{\text{lat}}) = \frac{1}{L^3}\langle H[\vec{\sigma}]\rangle, \tag{3.29}$$

where $H[\vec{\sigma}]$ is the Hamilton function of the 3d O(4) non-linear σ model with chemical potential, Eq. (2.66).

The *topological charge density* is

$$q(\beta_{\text{lat}}) = \frac{1}{L^3}\langle Q[\vec{\sigma}]\rangle, \tag{3.30}$$

where $Q[\vec{\sigma}]$ is the topological charge, Eq. (2.54).

The *magnetic susceptibilty* is defined by [57; 58; 59]

$$\chi_M(\beta_{\text{lat}}) = \frac{\beta_{\text{lat}}}{L^3}\left(\langle|\vec{M}[\vec{\sigma}]|^2\rangle - \langle|\vec{M}[\vec{\sigma}]|\rangle^2\right). \tag{3.31}$$

The *specific heat* is given by

$$c_V(\beta_{\text{lat}}) = \frac{\beta_{\text{lat}}^2}{L^3}\left(\langle(H[\vec{\sigma}])^2\rangle - \langle H[\vec{\sigma}]\rangle^2\right). \tag{3.32}$$

The *topological susceptibility* is

$$\chi_Q(\beta_{\text{lat}}) = \frac{1}{L^3}\left(\langle(Q[\vec{\sigma}])^2\rangle - \langle Q[\vec{\sigma}]\rangle^2\right). \tag{3.33}$$

In finite but large volume lattices with periodic boundary conditions, the connected correlation function $G(x, x')$ at large distances, $|x - x'| \gg 1$, behaves as

$$G(x, x') \propto \cosh\left(\frac{|x - x'| - L/2}{\xi_s(\beta_{\text{lat}})}\right), \qquad \xi_s(\beta_{\text{lat}}) > 0, \tag{3.34}$$

where $\xi_s(\beta_{\text{lat}})$ is the spin-spin correlation length. The following function behaves approximately as $G(x, x')$ at large distances,

$$C(n, m) = \langle\vec{S}_n \cdot \vec{S}_m\rangle - \langle\vec{S}_n\rangle \cdot \langle\vec{S}_m\rangle, \tag{3.35}$$

where

$$\vec{S}_n[\vec{\sigma}] = \frac{1}{L^2}\sum_{y,z=0}^{L-1}\vec{\sigma}_{(n,y,z)}, \tag{3.36}$$

where (n, y, z) is a lattice position with the first entry being n. Then,

$$C(0, n) = C(n) \propto \cosh\left(\frac{n - L/2}{\xi(\beta_{\text{lat}})}\right), \tag{3.37}$$

where $\xi(\beta_{\text{lat}})$ is the correlation length introduced in Eq. (3.12).

The *second moment correlation length* reads [60]

$$\xi_{\text{2nd}}(\beta_{\text{lat}}) = \frac{(\chi'_M(\beta_{\text{lat}})/F(\beta_{\text{lat}}) - 1)^{1/2}}{2\sin(\pi/L)}, \tag{3.38}$$

where

$$\chi'_M(\beta_{\text{lat}}) = \frac{1}{L^3}\langle|\vec{M}[\vec{\sigma}]|^2\rangle, \tag{3.39}$$

and

$$F(\beta_{\text{lat}}) = \frac{1}{L^3}\sum_{x,y\in\Lambda}\langle\vec{\sigma}_x \cdot \vec{\sigma}_y\rangle \cos\left(\frac{2\pi(x_1 - y_1)}{L}\right), \tag{3.40}$$

where x_1 and y_1 are the first components of lattice positions x and y.

The *root mean square magnetization* is

$$M_{\text{rms}}(\beta_{\text{lat}}) = \frac{1}{L^3}\sqrt{\langle|\vec{M}[\vec{\sigma}]|^2\rangle}. \tag{3.41}$$

At $T = T_c$, M_{rms} decays as [58]

$$M_{\text{rms}}(T_c) \propto (L^{2-d-\eta})^{1/2} \propto L^{-\beta/\nu}, \tag{3.42}$$

where η, β and ν are the critical exponents.

3.6 Autocorrelation times

The field configurations in a Markov chain are correlated (see Sec. 4.1), this correlation propagates to the observables. The autocorrelation time is a measure in the Markov chain time of the statistical correlation of a sample of an observable.

The *time displaced autocorrelation* of an observable $\mathcal{O}$ is defined by [59; 61]

$$C_{\mathcal{O}}(t) := \frac{1}{\int dt' \left[\mathcal{O}(t') - \langle\mathcal{O}\rangle\right]^2}\int dt' \left[\mathcal{O}(t') - \langle\mathcal{O}\rangle\right]\left[\mathcal{O}(t' + t) - \langle\mathcal{O}\rangle\right], \tag{3.43}$$

where $\mathcal{O}(t)$ is the temporary value of $\mathcal{O}$ at the Markov chain time t. The time displaced autocorrelation typically decays exponentially at long times,

$$C_{\mathcal{O}}(t) \propto e^{-t/\tau_{\mathcal{O}}}, \tag{3.44}$$

where $\tau_{\mathcal{O}}$ is the *autocorrelation time* of $\mathcal{O}$. The autocorrelation time is not an observable, it is a simulation artifact and depends on the specific simulation method. Intuitively, $\tau_{\mathcal{O}}$ is the time between two approximately independent measurements of the observable $\mathcal{O}$. Sampling at intervals of $2\tau_{\mathcal{O}}$ guarantees an almost independent sample [59; 61].

At T_c, the autocorrelation time scales as [58]

$$\tau_{\mathcal{O}}(T_c) \propto L^{z_{\mathcal{O}}}, \tag{3.45}$$

where $z_{\mathcal{O}}$ is the *dynamical critical exponent* of the observable $\mathcal{O}$. When $z_{\mathcal{O}} > 0$ the time to obtain statistically independent measures of $\mathcal{O}$ increases exponentially with volume, this phenomenon is known as *critical slowing down*.

3.7 Continuum and thermodynamic limits

Let $\mathcal{A}^{V,a/\xi}$ be the expectation values of a set of observables in a lattice regularized theory. The upper indices indicate that expectation values are taken on a lattice with volume V, lattice spacing a and correlation length ξ.

In the *thermodynamic limit*, we extrapolate the value of $\mathcal{A}^{V,a/\xi}$ to $\mathcal{A}^{\infty,a/\xi}$. On a d-dimensional lattice of size $(aL)^d$,

$$\mathcal{A}^{\infty,a/\xi} = \lim_{L\to\infty} \mathcal{A}^{(aL)^d,a/\xi}. \tag{3.46}$$

In the *continuum limit*, we extrapolate the value of $\mathcal{A}^{V,a/\xi}$ to $\mathcal{A}^{V,0}$,

$$\mathcal{A}^{V,0} = \lim_{a/\xi\to 0} \mathcal{A}^{V,a/\xi}. \tag{3.47}$$

4 Markov Chain Monte Carlo Methods

The wide range of *Markov chain Monte Carlo* (MCMC) methods are essential tools in the numerical approaches of numerous branches of science and technology. They arose as a sampling method of probability distributions in statistical mechanics. Therefore, sampling a probability distribution is the type of problems in which MCMC methods are applicable.

In this chapter we will review basic concepts of stochastic processes and Markov chains, and their applications to some MCMC methods. The algorithm, used in the numerical simulations of this work, is also described.

4.1 Stochastic processes

A *stochastic process* over a probability space $(\Omega, \mathcal{A}, P)$ (where Ω is a state space, $\mathcal{A}$ is the event space and P is a probability measure) and with initial probability distribution $p_0(x)$ ($p_0 : \Omega \to \mathbb{R}$ is such that $\int_\Omega p_0(x)dx = 1$), is defined as a set of random variables $\boldsymbol{X} = \{X_t \in \Omega | t \in T\}$, where T is an index set [62].

The index set T of a stochastic process is commonly called *time*. We say that $\boldsymbol{X}$ is a *discrete* or *continuous* stochastic process, depending on whether T is discrete or continuous. If T has more than one dimension, $\boldsymbol{X}$ is called a *random field* [63]. We call $X_t \in \boldsymbol{X}$ the state of the process at time t. If $\boldsymbol{X}$ is a discrete time stochastic process, from now on we will write $\boldsymbol{X} = \{i_n | n \in [0, N]\}$ with $N \in \mathbb{N}$ or more frequently $N = \infty$, in the later case we will write $\boldsymbol{X} = \{i_n | n \in \mathbb{N}\}$.

A computer can only deal with finite state spaces and discrete time. Our purpose is to apply the theory of stochastic processes and Markov chains to the numerical work with computers, therefore from now on we will only refer to stochastic processes with discrete state spaces. For simplicity we will assume that the time $T = \mathbb{N}$. The results and concepts exposed continue to be valid with some modifications to the continuous cases.

4.2 Markov chains

The Markov chains are the underlying essence of the MCMC algorithms. As discrete time Markov chains are needed in this work, a brief look at some definitions and properties will be given.

4.2.1 Some definitions and theorems

A (discrete time) *Markov chain* is a (discrete time) stochastic process $\boldsymbol{X} = \{i_0, \dots, i_n, \dots\}$, with a probability measure P having the property [62; 64]

$$P(i_n | i_0, \dots, i_{n-1}) = P(i_n | i_{n-1}). \tag{4.1}$$

This property means that the state of the process at time n only depends on the immediately previous state of the process at time $n - 1$.

The probabilities in Eq. (4.1) are called *transition probabilities* and are often written as $p_{jk}(n) := P(i_n = k|i_{n-1} = j), \forall j, k \in \Omega$. The $p_{jk}(n)$ probabilities form transition probability matrices $\boldsymbol{P}(n)$, such matrices are called *stochastic matrices* (these matrices have several interesting properties, for example $\sum_j p_{jk}(n) = \sum_k p_{jk}(n) = 1$ and $p_{jk}(n) \geq 0 \; \forall j, k$). We say that a Markov chain with time independent transition probabilities has *stationary transition probabilities* $\boldsymbol{P} \neq \boldsymbol{P}(n)$.

Let $a_{jk}(n) := P(i_n = k|i_0 = j)$; these transition probabilities form matrices $\boldsymbol{A}(n)$. If the Markov chain $\boldsymbol{X}$ has stationary transition probabilities, then by the Markovian property we can relate the matrices $\boldsymbol{A}(n)$ to the matrix $\boldsymbol{P}$, Eq. (4.1),

$$\boldsymbol{A}(n) = \boldsymbol{P}^n. \tag{4.2}$$

The *Chapman-Kolmogorov* theorem states that [63],

$$a_{jk}(n) = \sum_{l \in \Omega} a_{jl}(m) a_{lk}(n-m), \quad 1 \leq m \leq n-1. \tag{4.3}$$

Given two states i and j of a Markov chain $\boldsymbol{X}$, if there is $a_{ij}(n) > 0$ at some time n (n can be finite or infinite time), we say that i *reaches* j and we denote it as $i \to j$. The states i and j *communicate* if $i \to j$ and $j \to i$, we write it as $i \leftrightarrow j$. It can be shown that $\leftrightarrow$ is an equivalence relation [63]. Given a state i of a Markov chain $\boldsymbol{X}$, if $\boldsymbol{X}$ returns to i with probability 1 in a finite time (i.e. $a_{ii}(n) = 1$ for some finite $n > 0$), we say that i is a *recurrent* state. If the state i is not recurrent, it is called a *transient* state.

An equivalence class C of the equivalence relation $\leftrightarrow$ is called *positive recurrent* when all the members of the class are recurrent and $i \to j$ in a finite time, $\forall i, j \in C$. If the process reaches a positive recurrent class, the process remains in that class forever.

A Markov chain is said to be *irreducible* if any state of the chain is reachable from every other state. When a Markov chain is irreducible, there is only one positive recurrent class or all the states are transient [62].

If the initial probability distribution is $\boldsymbol{p}_0 = (P(i_0 = l_0), P(i_0 = l_1), P(i_0 = l_2) \dots)$ (where $l_0, l_1, l_2 \cdots \in \Omega$), hence the probability distribution at time n is given by [63]

$$\boldsymbol{p}_n = \boldsymbol{p}_0 \boldsymbol{A}(n). \tag{4.4}$$

If the Markov chain has stationary transition probabilities, then by Eq. (4.2),

$$\boldsymbol{p}_n = \boldsymbol{p}_0 \boldsymbol{P}^n. \tag{4.5}$$

If $\boldsymbol{p}_n = \boldsymbol{p}_0 \; \forall n \in \mathbb{N}$, we say that the Markov chain has a *stationary distribution*. From Eq. (4.5), a stationary distribution $\boldsymbol{p}$ obeys,

$$\boldsymbol{p}(\boldsymbol{P} - \boldsymbol{I}) = 0. \tag{4.6}$$

When a distribution is stationary, we write it as $\boldsymbol{\pi}$.

An irreducible Markov chain $\boldsymbol{X}$ has a stationary distribution $\boldsymbol{\pi}$ if and only if it has a positive recurrent class or equivalently if and only if it has no transient states [63]. This is a very useful property.

4.2.2 Ergodicity

The *period* of state i is the time d, where

$$d := \max\{m \in \mathbb{N} \mid a_{ii}(l) \neq 0 \text{ only if } l \text{ is a multiple of } m\}. \tag{4.7}$$

In other words, the period of state i is the maximum $d \in \mathbb{N}$ such that the process cannot return to state i in times which are not multiples of d. A state is called *aperiodic* if its period is 1. If state i is aperiodic, then the process can return to state i at any time, hence the name aperiodic.

If two states communicate, $i \leftrightarrow j$, both have the same period [63]. Therefore, all states in a positive recurrent class have the same period; in this case we will refer to the period of the class.

A Markov chain is *ergodic* if it has a unique positive recurrent class C and it is aperiodic [63]. From this, a Markov chain is not ergodic if it has a state with period $d > 1$ or at least two positive recurrent classes C_1 and C_2 such that $P(C_1) > 0$ and $P(C_2) > 0$ [62].

Due to the aperiodicity and positive recurrence of the ergodic Markov chains, there exists a natural number $N(i, j)$ such that $a_{ij}(m) > 0 \; \forall m \geq N$ [64]. This means that at a large time the state i reaches the state j with nonzero probability, for all the states i and k in the Markov chain.

If an ergodic Markov chain has a stationary distribution, it is unique [62; 64], i.e. the solution of the Eq. (4.6), if it exists, is unique in ergodic Markov chains. This is a very valuable property.

4.2.3 Detailed balance

Given a Markov chain $\boldsymbol{X} = \{X_n | n \in \mathbb{N}\}$, with stationary transition probabilities p_{ij} and a stationary distribution π_j, we can define another Markov chain $\boldsymbol{Y} = \{Y_m | m \in \mathbb{N}\}$ such that $\forall m \in \mathbb{N}\; Y_m = X_n$ for some $n \in \mathbb{N}$ and if $n > 0$ then $Y_{m+1} = X_{n-1}$; $\boldsymbol{Y}$ is the reversed time Markov chain of $\boldsymbol{X}$. We say that $\boldsymbol{X}$ is *reversible* if $\boldsymbol{X}$ and $\boldsymbol{Y}$ have equal transition probabilities, this is, if [63; 64]

$$\pi_i p_{ij} = \pi_j p_{ji}, \qquad \forall i, j \in \Omega. \tag{4.8}$$

This equation is called the *detailed balance* condition, it ensures that the probability flux between any two arbitrary states is zero.

If we have an irreducible and reversible Markov chain $\boldsymbol{X}$ with a probability distribution $\boldsymbol{p}$, hence $\boldsymbol{p}$ is a stationary distribution and, as we saw earlier at the end of the Sec. 4.2.1, $\boldsymbol{X}$ is positive recurrent [63; 64]. If an ergodic Markov chain $\boldsymbol{X}$ has a probability distribution $\boldsymbol{p}$ satisfying the Eq. (4.8), then $\boldsymbol{p}$ is the unique stationary probability distribution of $\boldsymbol{X}$. We will see later the application of this theorem to the MCMC methods.

4.2.4 Limiting behavior

If an ergodic Markov chain has a stationary distribution $\boldsymbol{\pi}$, then $\lim_{n\to\infty} a_{ij}(n) = \pi_j \; \forall i \in \Omega$ [63; 64], i.e.

$$\lim_{n\to\infty} \boldsymbol{A}(n) = \begin{pmatrix} \boldsymbol{\pi} \\ \vdots \\ \boldsymbol{\pi} \end{pmatrix}, \tag{4.9}$$

where $\boldsymbol{\pi}$ is the row vector of the stationary distribution. This means that, regardless of the initial state of the Markov chain, the transition probabilities converge to the stationary distribution. In the cases where Eq. (4.9) occurs, we say that $\boldsymbol{A}(n)$ has a *limiting distribution* $\boldsymbol{\pi}$.

Given an initial probability distribution $\boldsymbol{p}_0$, using Eqs. (4.4) and (4.9) we can deduce that

$$\begin{aligned}\lim_{n\to\infty}(p_n)_i &= \lim_{n\to\infty}\sum_{j\in\Omega}(p_0)_j a_{ji}(n)\\ &= \sum_{j\in\Omega}(p_0)_j\pi_i\\ &= \pi_i.\end{aligned} \tag{4.10}$$

If a Markov chain is ergodic and has a stationary distribution $\boldsymbol{\pi}$, then regardless of the initial probability distribution $\boldsymbol{p}_0$, the probability distribution converges to the stationary distribution $\boldsymbol{\pi}$.

Let $\boldsymbol{X}$ be an ergodic Markov chain with stationary distribution $\boldsymbol{\pi}$. Let f be a real valued function, $f:\Omega\to\mathbb{R}$. With $\langle f\rangle_{\boldsymbol{\pi}}$ we denote the expectation value of f in the stationary distribution $\boldsymbol{\pi}$. The *ergodic theorem* states: Regardless of the initial probability distribution function $\boldsymbol{p}_0$ of $\boldsymbol{X}$, if $|\langle f\rangle_{\boldsymbol{\pi}}|<\infty$, then

$$\lim_{n\to\infty}\frac{1}{n}\sum_{j=0}^{n} f(i_j) = \langle f\rangle_{\boldsymbol{\pi}}, \tag{4.11}$$

where $i_j\in\boldsymbol{X}$ [63; 64]. This theorem gives us a simple method to find expectation values in the stationary distribution.

4.3 Markov chain Monte Carlo methods

4.3.1 Metropolis algorithm

The first Markov chain Monte Carlo (MCMC) method was introduced by Metropolis et al. [65]. The so called *Metropolis algorithm* is a general method for the numerical approach to statistical mechanical problems. It is especially useful for the non-analytically soluble type of problems. In this section we will review this algorithm.

Let $\boldsymbol{\pi}$ be a stationary probability distribution over a probability space $(\Omega,\mathcal{A},P)$. Let $\boldsymbol{B}$ be a symmetrical stationary transition matrix, such that $0<b_{ij}\leq 1\ \forall i,j\in\Omega$. It is convenient to take $b_{ij}=b\ \forall i,j\in\Omega$, with $b>0$ a constant probability.

The Metropolis algorithm, to construct a Markov chain $\boldsymbol{X}$ with stationary probability distribution $\boldsymbol{\pi}$, is described in MCMC 1.

MCMC 1 Metropolis

1: Propose one state i_0 from the state space Ω, this is the first element of $\boldsymbol{X}$.

2: Let i_t be the present element of $\boldsymbol{X}$.

3: Propose a random new state $x\in\Omega$.

4: The next element of $\boldsymbol{X}$ is,

$$i_{t+1}=\begin{cases}x & \text{with probability } b_{i_t x}\min\{1,\pi_x/\pi_{i_t}\}\\ i_t & \text{otherwise.}\end{cases} \tag{4.12}$$

5: Return to steps 2.

The acceptance probability of a new state only depends on the last step. Therefore, $\boldsymbol{X}$ satisfy the Markovian property, Eq. (4.1), by construction.

The transition probabilities p_{ij} for $i \neq j$ are [63; 64]

$$p_{ij} = b_{ij} \min\{1, \pi_j/\pi_i\} \tag{4.13}$$

and for $i = j$ are [63; 64]

$$p_{ii} = b_{ii} + \sum_{\substack{x \in \Omega \\ x \neq i}} b_{ix}(1 - \min\{1, \pi_x/\pi_i\}). \tag{4.14}$$

If there are states $i \in \Omega$ such that $\pi_i = 0$, we simply discard these states, taking $\Omega' = \{i \in \Omega | \pi_i \neq 0\}$ as our new state space. Then, in Ω' the right-hand sides of Eqs. (4.13) and (4.14) are well defined. Since $b_{ij} > 0 \; \forall i, j \in \Omega'$, then

$$p_{ij} > 0, \quad \forall i, j \in \Omega'. \tag{4.15}$$

The case $i = j$ of the Eq. (4.8) is always satisfied. For $i \neq j$ and $\pi_i \geq \pi_j$, using Eq. (4.13) and the symmetry of $\boldsymbol{B}$ we have,

$$\frac{p_{ij}}{p_{ji}} = \frac{b_{ij} \min\left\{1, \pi_j/\pi_i\right\}}{b_{ji} \min\left\{1, \pi_i/\pi_j\right\}} = \frac{\pi_j/\pi_i}{1} = \frac{\pi_j}{\pi_i} \tag{4.16}$$

i.e. $\pi_i p_{ij} = \pi_j p_{ji}$, this is the Eq. (4.8). In a similar way, we can also check Eq. (4.8) for $\pi_i < \pi_j$. So, the detailed balance condition is satisfied and hence $\boldsymbol{\pi}$ is a stationary distribution of $\boldsymbol{X}$.

Since $\boldsymbol{X}$ has a stationary transition matrix $\boldsymbol{P}$, by Eqs. (4.2) and (4.15) we have that

$$a_{ij}(n) > 0, \quad \forall i, j \in \Omega' \text{ and } \forall n \in \mathbb{N}. \tag{4.17}$$

By this, $\boldsymbol{X}$ is aperiodic and all its elements communicate in a finite time. Therefore, $\boldsymbol{X}$ is ergodic and $\boldsymbol{\pi}$ is the limiting probability distribution of $\boldsymbol{X}$.

4.3.2 Local and non-local updates

When dealing with classical spin models, like Ising and Potts models, there are mainly two classes of applicable MCMC algorithms, the local update algorithms and the non-local update algorithms. *Local update algorithms* perform an update of a single element of the lattice each time. On the other hand, *non-local update algorithms* can perform collective updates on the lattice.

Non-local update algorithms, like Swendsen-Wang and Wolff algorithms, have proven their effectiveness in the significant reduction of the critical slowing down effect [66], see Sec. 3.6. Hence the non-local update algorithms have become the standard algorithms when dealing with critical phenomena in classical spin models. In the next two subsections, we discuss the Swendsen-Wang and Wolff algorithms[1].

4.3.3 Swendsen-Wang algorithm

The original *Swendsen-Wang* algorithm, also known as the *multicluster* algorithm, is the result of a back and forth mapping from a Potts model to a percolation problem [66; 67].

Let Λ be a d-dimensional cubic lattice[2], with L lattice sites per edge and lattice spacing $a = 1$,

[1] Our terminology differs from most of the literature, usually the Swendsen-Wang algorithm is the multicluster algorithm for the Potts model and the Wolff algorithm is the generalization of the multicluster algorithm for the O(N) models.

[2] The cubic lattice was defined in Eq. (2.30).

$$\Lambda := \{x | x \in [0, L-1]^d\}. \tag{4.18}$$

Let $\vec{\sigma}$ be a vector field,

$$\vec{\sigma} : \Lambda \to S^n, \tag{4.19}$$

where S^n is the n-dimensional sphere. Therefore,

$$\vec{\sigma}_x^2 = 1, \quad \forall x \in \Lambda. \tag{4.20}$$

We suppose periodic boundary conditions, then $\forall x \in \Lambda$ and for each standard unit vector e_i in $\mathbb{R}^d$ we have,

$$\vec{\sigma}_{x+Le_i} = \vec{\sigma}_x. \tag{4.21}$$

Let H be the lattice regularized Hamiltonian of the d-dimensional O(N) σ model,

$$H[\vec{\sigma}] = -J \sum_{\langle xy \rangle \in \Lambda} \vec{\sigma}_x \cdot \vec{\sigma}_y, \tag{4.22}$$

where J is the coupling constant. The sum of Eq. (4.22) runs over all *nearest neighbors* sites $\langle xy \rangle$ in the lattice Λ.

Let P be the following probability density function,

$$P[\vec{\sigma}] = \frac{1}{Z} e^{-\beta H[\vec{\sigma}]}, \tag{4.23}$$

where β is the inverse temperature, i.e. $\beta = 1/T$, and Z is the partition function,

$$Z(\beta) = \int [d\vec{\sigma}] e^{-\beta H[\vec{\sigma}]}, \tag{4.24}$$

where the integration is over field configurations, $[d\vec{\sigma}]$.

The multicluster algorithm, to construct a Markov chain $\boldsymbol{X}$ with stationary distribution $P[\vec{\sigma}]$ (Eq. (4.23)), is described below in MCMC 2 [66; 67].

The efficiency of the multicluster algorithm depends on the efficient identification of the clusters performed in step 5 of MCMC 2. An efficient algorithm to identify clusters was introduced by Hoshen and Kopelman [68].

Ergodicity of the resulting Markov chain $\boldsymbol{X}$ and the preservation of the initial probability distribution by the multicluster algorithm are demonstrated for the Potts model in ref. [66]. In a similar way this can be demonstrated for the d-dimensional O(N) σ model.

Suppose two field configurations to be given $\vec{\sigma}$ and $\vec{\sigma}' \in \Omega$. If the vector $\hat{r}$ of step 3 of MCMC 2 is suitable, we can transform $\vec{\sigma}_x$ into $\vec{\sigma}'_x$ in just one reflection. The multicluster algorithm always has nonzero probability of forming single site clusters and reflecting only one of those clusters, for nonzero temperatures. Then, in a finite state space at nonzero temperature, the multicluster algorithm always has nonzero probability to transform $\vec{\sigma}$ into $\vec{\sigma}'$ in at most L^d iterations[3]. Therefore, in a finite state space Ω, all elements of Ω communicate in a finite time. So, the resulting Markov chain $\boldsymbol{X}$ from the multicluster algorithm has a unique positive recurrent class.

[3]By an iteration we mean the steps 2 to 7 of MCMC 2.

The multicluster algorithm always has nonzero probability to generate two identical consecutive configurations (when none of the clusters is reflected). Then $\boldsymbol{X}$ is aperiodic.

From all this, the resulting Markov chain $\boldsymbol{X}$ from the multicluster algorithm is ergodic. Furthermore, the Eq. (4.23) satisfy detailed balance condition by a generalization of the argument by which this condition is satisfied in the single cluster algorithm (given in the next section). Therefore, the Eq. (4.23) is the limiting distribution of the Markov chain generated with the algorithm MCMC 2.

MCMC 2 Swendsen-Wang or multicluster

1: Propose an initial field configuration $\vec{\sigma}_0$ from the state space Ω, this is the first element of $\boldsymbol{X}$.

2: Let $i_t = \vec{\sigma}_t$ be the present element of $\boldsymbol{X}$.

3: Propose a random unit vector $\hat{r} \in \mathbb{R}^n$.

4: For each pair of nearest neighbors sites $\langle xy \rangle \in \Lambda$, set a bond between $[\vec{\sigma}_t]_x$ and $[\vec{\sigma}_t]_y$ with probability

$$P_{\text{bond}}([\vec{\sigma}_t]_x, [\vec{\sigma}_t]_y) = 1 - e^{\min\{0, -\beta \Delta h([\vec{\sigma}_t]_x, [\vec{\sigma}_t]_y)\}}, \tag{4.25}$$

where

$$\Delta h([\vec{\sigma}_t]_x, [\vec{\sigma}_t]_x) = J([\vec{\sigma}_t]_x \cdot [\vec{\sigma}_t]_y - [\vec{\sigma}_t]_x \cdot \vec{R}_{\hat{r}}([\vec{\sigma}_t]_y)) = 2J(\hat{r} \cdot [\vec{\sigma}_t]_x)(\hat{r} \cdot [\vec{\sigma}_t]_y), \tag{4.26}$$

with the reflected spin $\vec{R}_{\hat{r}}$,

$$\vec{R}_{\hat{r}}([\vec{\sigma}_t]_y) := [\vec{\sigma}_t]_y - 2(\hat{r} \cdot [\vec{\sigma}_t]_y)\hat{r}. \tag{4.27}$$

5: Identify all the clusters in Λ. Two spins in the lattice $[\vec{\sigma}_t]_x$ and $[\vec{\sigma}_t]_y$ are in the same cluster if there is a path of bonds joining them.

6: Denote the set of reflected clusters as $\mathscr{C}_R$. For each cluster C in Λ, C is in $\mathscr{C}_R$ with probability 1/2 (or another constant probability).

7: The new element of $\boldsymbol{X}$, i_{t+1}, is the following field configuration,

$$[\vec{\sigma}_{t+1}]_x = \begin{cases} \vec{R}_{\hat{r}}([\vec{\sigma}_t]_x), & \text{if } [\vec{\sigma}_t]_x \in C \text{ for some } C \in \mathscr{C}_R \\ [\vec{\sigma}_t]_x, & \text{otherwise.} \end{cases} \tag{4.28}$$

8: Return to steps 2.

4.3.4 Wolff algorithm

The *Wolff* algorithm[4], also known as the *single cluster* algorithm, is again based in a back and forth mapping from a classical spin model to a percolation problem [69].

Let Λ be a d-dimensional cubic lattice and $\vec{\sigma}$ a vector field, as defined in Sec. 4.3.3. We will consider the Hamiltonian of the d-dimensional O(N) σ model, Eq. (4.22). Hence, the probability density function $P[\vec{\sigma}]$ is given by Eq. (4.23).

The Wolff algorithm to construct a Markov chain $\boldsymbol{X}$ with stationary distribution $P[\vec{\sigma}]$ (Eq. (4.23)), is described below in MCMC 3 [69; 70].

[4] In the literature, the Wolff algorithm refers to the multicluster algorithm for O(N) models. However, Wolff introduced the single cluster algorithm.

The Wolff algorithm is closely related to the multicluster algorithm. Given a vector $\hat{r}$, the selection of a random seed in step 4 of the Wolff algorithm is identical to the selection of a random cluster from all clusters formed in the multicluster algorithm. Larger clusters are more likely to be elected.

The bond probability, Eq. (4.25), is 0 when $\Delta h < 0$, this occurs when $\vec{\sigma}_x$ and $\vec{\sigma}_y$ are on opposite sides of the hyperplane perpendicular to $\hat{r}$. Therefore, all spins in the cluster are at the same side of the hyperplane orthogonal to $\hat{r}$. Further, there is a probability larger than $1/2$ of finding the nearest neighbors spins of the cluster on the opposite side of the hyperplane. Then, with a probability larger than $1/2$, the cluster reflection with respect to the previous hyperplane create a more ordered field configuration, which is a lower energy configuration. Also, there is a nonzero probability of creating a less ordered field configuration; for example, if we take our seed in an ordered zone of the lattice, and not all the spins on the same side of the hyperplaned are added to the cluster. The evolution of the field configurations to lower energy configurations, with a nonzero probability of evolving to a higher energy configuration, is basically the same idea of a local update Metropolis algorithm. This is an intuitive idea of why the Wolff algorithm works and how it relates to local update Metropolis algorithms.

MCMC 3 Wolff or single cluster

1: Propose an initial field configuration $\vec{\sigma}_0$ from the state space Ω, this is the first element of $\boldsymbol{X}$.

2: Let $i_t = \vec{\sigma}_t$ be the present element of $\boldsymbol{X}$.

3: Propose a random unit vector $\hat{r} \in \mathbb{R}^n$.

4: Take a random lattice site x; $[\vec{\sigma}_t]_x$ will be the seed (first element) of the cluster $C \subseteq \Lambda$.

5: For each pair of nearest neighbors sites $\langle xy \rangle$, such that $[\vec{\sigma}_t]_x \in C$ and $[\vec{\sigma}_t]_y \notin C$, add the spin $[\vec{\sigma}_t]_y$ to C with probability,

$$P_{\text{bond}}([\vec{\sigma}_t]_x, [\vec{\sigma}_t]_y) = 1 - e^{\min\{0, -\beta \Delta h([\vec{\sigma}_t]_x, [\vec{\sigma}_t]_y)\}}, \tag{4.25}$$

where $\Delta h([\vec{\sigma}_t]_x, [\vec{\sigma}_t]_y)$ is again,

$$\Delta h([\vec{\sigma}_t]_x, [\vec{\sigma}_t]_x) = J[[\vec{\sigma}_t]_x \cdot [\vec{\sigma}_t]_y - [\vec{\sigma}_t]_x \cdot \vec{R}_{\hat{r}}([\vec{\sigma}_t]_y)] = 2J(\hat{r} \cdot [\vec{\sigma}_t]_x)(\hat{r} \cdot [\vec{\sigma}_t]_y). \tag{4.26}$$

Repeat this step until there are no new elements in C. Each spin $[\vec{\sigma}_t]_y$ must have at most one opportunity to join C.

6: The new element of $\boldsymbol{X}$, i_{t+1}, is the following field configuration,

$$[\vec{\sigma}_{t+1}]_x = \begin{cases} \vec{R}_{\hat{r}}([\vec{\sigma}_t]_x), & \text{if } [\vec{\sigma}_t]_x \in C \\ [\vec{\sigma}_t]_x, & \text{otherwise.} \end{cases} \tag{4.29}$$

The reflected spin is again,

$$\vec{R}_{\hat{r}}([\vec{\sigma}_t]_x) = [\vec{\sigma}_t]_x - 2(\hat{r} \cdot [\vec{\sigma}_t]_x)\hat{r}. \tag{4.27}$$

7: Return to steps 2.

Consider two field configurations $\vec{\sigma}$ and $\vec{\sigma}'$, where $\vec{\sigma}'$ differs from $\vec{\sigma}$ by a reflection of a cluster C with respect to the hyperplane orthogonal to the vector $\hat{r}_C$. We denote as ∂C the nearest neighbors $\langle xy \rangle$ such that $x \in C$ and $y \notin C$.[5]

[5]Occasionally we will write $x \in C$ when $\vec{\sigma}_x \in C$, although it must be stressed that a cluster is a set of spins not of

The scalar product of two arbitrary spins is preserved under the reflection of both spins,

$$\vec{R}_{\hat{r}}(\vec{\sigma}_x) \cdot \vec{R}_{\hat{r}}(\vec{\sigma}_y) = \vec{\sigma}_x \cdot \vec{\sigma}_y. \tag{4.30}$$

Reflecting twice with respect to the same reflection vector left the spin unchanged,

$$\vec{R}_{\hat{r}}(\vec{R}_{\hat{r}}(\vec{\sigma}_x)) = \vec{\sigma}_x, \tag{4.31}$$

therefore, from Eq. (4.30) we have the following equation,

$$\vec{R}_{\hat{r}}(\vec{\sigma}_x) \cdot \vec{\sigma}_y = \vec{\sigma}_x \cdot \vec{R}_{\hat{r}}(\vec{\sigma}_y). \tag{4.32}$$

Eq. (4.30) implies that the contributions to the total energy of the system from interactions of the spins inside the cluster C are the same before and after the reflection of C. Therefore, the energy difference of the field configurations $\vec{\sigma}$ and $\vec{\sigma}'$ comes only from the energy difference at ∂C.

Using Eqs. (4.30) and (4.32) in Eq. (4.26), we obtain for $\langle xy \rangle \in C$,

$$\Delta h(\vec{\sigma}_x, \vec{\sigma}_y) = \Delta h(\vec{\sigma}'_x, \vec{\sigma}'_y). \tag{4.33}$$

Using this equation in Eq. (4.25), we obtain

$$P_{\text{bond}}(\vec{\sigma}_x, \vec{\sigma}_y) = P_{\text{bond}}(\vec{\sigma}'_x, \vec{\sigma}'_y), \tag{4.34}$$

again for $\langle xy \rangle \in C$.

Given the reflection vector $\hat{r}_C$, the transition probabilities $p_{\vec{\sigma}\vec{\sigma}'}$ are [6]

$$p_{\vec{\sigma}\vec{\sigma}'} = \frac{|C|}{L^3} \left[\prod_{\langle xy \rangle \in C} P_{\text{bond}}(\vec{\sigma}_x, \vec{\sigma}_y) \right] \left[\prod_{\langle xy \rangle \in \partial C} (1 - P_{\text{bond}}(\vec{\sigma}_x, \vec{\sigma}_y)) \right], \tag{4.35}$$

where $|C|$ denotes the number of spins in the cluster C.

Using Eqs. (4.34) and (4.35) ,

$$\begin{aligned} \frac{p_{\vec{\sigma}\vec{\sigma}'}}{p_{\vec{\sigma}'\vec{\sigma}}} &= \prod_{\langle xy \rangle \in \partial C} \frac{1 - P_{\text{bond}}(\vec{\sigma}_x, \vec{\sigma}_y)}{1 - P_{\text{bond}}(\vec{\sigma}'_x, \vec{\sigma}'_y)}, \\ &= \prod_{\langle xy \rangle \in \partial C} \exp\Big(\min\{0, -\beta \Delta h(\vec{\sigma}_x, \vec{\sigma}_y)\} - \min\{0, -\beta \Delta h(\vec{\sigma}'_x, \vec{\sigma}'_y)\} \Big), \end{aligned}$$

at ∂C we have that $\Delta h(\vec{\sigma}'_x, \vec{\sigma}'_y) = -\Delta h(\vec{\sigma}_x, \vec{\sigma}_y)$, so

$$\begin{aligned} \frac{p_{\vec{\sigma}\vec{\sigma}'}}{p_{\vec{\sigma}'\vec{\sigma}}} &= \prod_{\langle xy \rangle \in \partial C} \exp\left(\min\{0, -\beta \Delta h(\vec{\sigma}_x, \vec{\sigma}_y)\} - \min\{0, \beta \Delta h(\vec{\sigma}_x, \vec{\sigma}_y)\} \right), \\ &= \exp\left(-\beta \sum_{\langle xy \rangle \in \partial C} \Delta h(\vec{\sigma}_x, \vec{\sigma}_y) \right), \\ &= \exp\left(-J\beta \sum_{\langle xy \rangle \in \partial C} \left(\vec{\sigma}_x \cdot \vec{\sigma}_y - \vec{\sigma}_x \cdot \vec{R}_{\hat{r}_C}(\vec{\sigma}_y) \right) \right). \end{aligned}$$

lattice sites.

[6] In a continuum state space Ω, if we do not assume that the reflection vector is $\hat{r}_C$, then $p_{\vec{\sigma}\vec{\sigma}'} = 0$. In continuum state spaces a field configuration has measure zero. In general, in continuum state spaces we must use nonzero measure subsets, as the energy values, to make statements.

In a finite state space $p_{\vec{\sigma}\vec{\sigma}'} \neq 0$, our assumption that the reflection vector is $\hat{r}_C$ eliminates a multiplicative constant from $p_{\vec{\sigma}\vec{\sigma}'}$.

Using Eq. (4.32) we obtain the following,

$$\frac{p_{\vec{\sigma}\vec{\sigma}'}}{p_{\vec{\sigma}'\vec{\sigma}}} = \exp\left(-J\beta \sum_{\langle xy\rangle \in \partial C} \left(\vec{\sigma}_x \cdot \vec{\sigma}_y - \vec{R}_{\hat{r}_C}(\vec{\sigma}_x) \cdot \vec{\sigma}_y\right)\right),$$

since $y \notin C$ these spins are not reflected, this is $\vec{\sigma}_y = \vec{\sigma}'_y$, then

$$\frac{p_{\vec{\sigma}\vec{\sigma}'}}{p_{\vec{\sigma}'\vec{\sigma}}} = \exp\left(-J\beta \sum_{\langle xy\rangle \in \partial C} \left(\vec{\sigma}_x \cdot \vec{\sigma}_y - \vec{\sigma}'_x \cdot \vec{\sigma}'_y\right)\right).$$

The scalar product is preserved by the cluster reflection except at ∂C, i.e. $\vec{\sigma}'_x \cdot \vec{\sigma}'_y = \vec{\sigma}_x \cdot \vec{\sigma}_y$, $\forall \langle xy\rangle \notin \partial C$, hence

$$\begin{aligned}\frac{p_{\vec{\sigma}\vec{\sigma}'}}{p_{\vec{\sigma}'\vec{\sigma}}} &= \exp\left(J\beta \sum_{\langle xy\rangle \in C} \left(\vec{\sigma}'_x \cdot \vec{\sigma}'_y - \vec{\sigma}_x \cdot \vec{\sigma}_y\right)\right), \\ &= \frac{P[\vec{\sigma}']}{P[\vec{\sigma}]}.\end{aligned}$$

In conclusion,

$$P[\vec{\sigma}]p_{\vec{\sigma}\vec{\sigma}'} = P[\vec{\sigma}']p_{\vec{\sigma}'\vec{\sigma}}, \tag{4.36}$$

this is the detailed balance equation, Eq. (4.8). If $\vec{\sigma}$ and $\vec{\sigma}'$ differ by two or more clusters we have that $p_{\vec{\sigma}\vec{\sigma}'} = p_{\vec{\sigma}'\vec{\sigma}} = 0$, so the Eq. (4.8) is also satisfied. As a consequence, the Eq. (4.23) is a stationary probability density function of the Markov chain $\boldsymbol{X}$ generated with the Wolff algorithm.

Consider two field configurations $\vec{\sigma}$ and $\vec{\sigma}' \in \Omega$; with the appropriate reflection vector, $\hat{r}$ from step 3 of MCMC 3, we can transform $\vec{\sigma}_x$ into $\vec{\sigma}'_x$ in just one reflection. The Wolff algorithm always has nonzero probability of forming a single site cluster, for nonzero temperatures. Then, in a finite state space Ω at nonzero temperature, the Wolff algorithm always has nonzero probability to transform $\vec{\sigma}$ into $\vec{\sigma}'$ in at most L^d iterations[7]. Therefore, in a finite state space Ω, all elements of Ω communicate in a finite time. Consequently, the resulting Markov chain $\boldsymbol{X}$ from the single cluster algorithm has a unique positive recurrent class.

Let $\vec{\sigma}_1$ and $\vec{\sigma}_2$ belong to a finite state space Ω, the field $\vec{\sigma}_2$ differs from $\vec{\sigma}_1$ by the reflection of a cluster C_1, such that $|C_1| > 1$. The Wolff algorithm always has nonzero probability of going from $\vec{\sigma}_1$ to $\vec{\sigma}_2$ and then return to $\vec{\sigma}_1$, for nonzero temperature. Hence, $\boldsymbol{X}$ has at most period 2. Now, consider two other different field configurations $\vec{\sigma}_3$ and $\vec{\sigma}_4$ in Ω, such that $\vec{\sigma}_1$ and $\vec{\sigma}_3$ differs by a reflections in a cluster C_2, and $\vec{\sigma}_3$ differs from $\vec{\sigma}_4$ by a reflection in a cluster C_3. Moreover, C_2 and C_3 are such that $C_2 \cup C_3 = C_1$ and $C_2 \cap C_3 = \varnothing$. At nonzero temperature, the Wolff algorithm always has nonzero probability of going from $\vec{\sigma}_1$ to $\vec{\sigma}_3$, then to $\vec{\sigma}_4$ and then go back to $\vec{\sigma}_1$. If $\boldsymbol{X}$ has period 2, this route through 3 field configurations would be impossible. Therefore $\boldsymbol{X}$ is aperiodic.

Based on these properties, the resulting Markov chain $\boldsymbol{X}$ from the Wolff algorithm is ergodic. This together with the detailed balance condition, Eq. (4.36), imply that the Eq. (4.23) is the limiting probability density function of $\boldsymbol{X}$.

4.4 3d O(4) model with chemical potential

In this work a combination of Swendsen-Wang and Metropolis algorithms was used for the 3d O(4) model with a chemical potential.

[7] By an iteration we mean the steps 2 to 6 of MCMC 3.

Let Λ be a 3d cubic lattice and $\vec{\sigma}$ an O(4) vector field, both as defined in Sec. 4.3.3. Let H be the lattice Hamiltonian of the 3d O(4) σ model with chemical potential,

$$H[\vec{\sigma}] = -\sum_{x\in\Lambda}\sum_{i=1}^{3}\vec{\sigma}_{x+e_i}\cdot\vec{\sigma}_x - \mu_{B,\text{lat}}Q[\vec{\sigma}]. \tag{2.66}$$

Eq. (2.66) can be split into two independent parts,

$$H[\vec{\sigma}] = H_1[\vec{\sigma}] + H_2[\vec{\sigma}], \tag{4.37}$$

with

$$H_1[\vec{\sigma}] = -\sum_{x\in\Lambda}\sum_{i=1}^{3}\vec{\sigma}_{x+e_i}\cdot\vec{\sigma}_x = -\sum_{\langle xy\rangle\in\Lambda}\vec{\sigma}_x\cdot\vec{\sigma}_y, \tag{4.38}$$

and

$$H_2[\vec{\sigma}] = -\mu_{B,\text{lat}}Q[\vec{\sigma}]. \tag{4.39}$$

Let P be the probability density function of the 3d O(4) σ model with chemical potential,

$$P[\vec{\sigma}] = \frac{1}{Z}e^{-\beta_{\text{lat}}H[\vec{\sigma}]}, \tag{4.40}$$

where H is the Hamiltonian Eq. (2.66), β is the inverse temperature, i.e. $\beta = 1/T$, and Z is the partition function.

Using the Eqs. (4.38) and (4.39), the probability density function Eq. (4.40) can be written as

$$P[\vec{\sigma}] = P_1[\vec{\sigma}]P_2[\vec{\sigma}], \tag{4.41}$$

with

$$P_1[\vec{\sigma}] \propto e^{-\beta_{\text{lat}}H_1[\vec{\sigma}]}, \tag{4.42}$$

and

$$P_2[\vec{\sigma}] \propto e^{-\beta_{\text{lat}}H_2[\vec{\sigma}]}. \tag{4.43}$$

and (4.39) respectively (defined in Eq. (2.61)). The splitting of the probability density function can be done because Eqs. (4.38) and (4.39) are independent.

The probability given by Eq. (4.42) can be introduced into the bond probability in the Wolff or Swendsen-Wang algorithms. The probability coming from Eq. (4.43) cannot be part of the bond probability and therefore must be introduced in a different way. In the chosen algorithm, this is done introducing a non-constant reflection probability in the Swendsen-Wang algorithm (the same can be done in the Wolff algorithm). The non-constant reflection probability corresponds to a transition probability from a Metropolis algorithm. The algorithm used is described below in MCMC 4.

Two of the possible initial configurations i_0 are the hot and cold starts. In the *hot start*, $\vec{\sigma}_x$ is a random unit vector in $\mathbb{R}^4$, $\forall x \in \Lambda$. In the *cold start*, let $\hat{u}$ be a unit vector in $\mathbb{R}^4$, then $\vec{\sigma}_x = \hat{u}$, $\forall x \in \Lambda$.

The MCMC 4 algorithm is a composition of Swendsen-Wang and Metropolis algorithms, for P_1 and P_2 probabilities density functions respectively. Each algorithm satisfies detailed balance and ergodicity individually, therefore the MCMC 4 algorithm also satisfy detailed balance and ergodicity. Then Eq. (4.40) is the limiting probability density function of the Markov chain $\boldsymbol{X}$ generated with the MCMC 4.

After some time evolution of the Markov chain, we will arrive close enough to the limiting probability density function. In practice, the initial states are discarded until the approximate

stabilization of the expectation values of the observables. The time until this approximate stabilization is called *thermalization time*.

MCMC 4 $3DO(4)$ **with chemical potential** $\mu_{B,\mathrm{lat}}$

1: Propose an initial field configuration $\vec{\sigma}_0$ from the state space Ω, this is the first element of $\boldsymbol{X}$.

2: Let $i_t = \vec{\sigma}_t$ be the present element of $\boldsymbol{X}$.

3: Propose a random unit vector $\hat{r} \in \mathbb{R}^4$.

4: For each pair of nearest neighbors sites $\langle xy \rangle \in \Lambda$, set a bond between $[\vec{\sigma}_t]_x$ and $[\vec{\sigma}_t]_y$ with probability

$$P_{\mathrm{bond}}([\vec{\sigma}_t]_x, [\vec{\sigma}_t]_y) = 1 - e^{\min\{0, -\beta_{\mathrm{lat}} \Delta h([\vec{\sigma}_t]_x, [\vec{\sigma}_t]_y)\}}, \tag{4.25}$$

where

$$\Delta h([\vec{\sigma}_t]_x, [\vec{\sigma}_t]_y) = 2(\hat{r} \cdot [\vec{\sigma}_t]_x)(\hat{r} \cdot [\vec{\sigma}_t]_y). \tag{4.26}$$

5: Identify all the clusters in Λ. Two spins in the lattice $[\vec{\sigma}_t]_x$ and $[\vec{\sigma}_t]_y$ are in the same cluster if there is a path of bonds joining them.

6: Denote the set of clusters to be reflected as $\mathscr{C}_R$. For each cluster C in Λ, C is in $\mathscr{C}_R$ with probability

$$P_{\mathrm{ref}}(C) = \frac{1}{2} \min\{1, \exp(-\beta_{\mathrm{lat}} \mu_{B,\mathrm{lat}} \Delta Q)\}, \tag{4.44}$$

where

$$\Delta Q = Q[\vec{\sigma}_t'] - Q[\vec{\sigma}_t]. \tag{4.45}$$

$\vec{\sigma}_t'$ is the field configuration after reflecting the cluster C,

$$[\vec{\sigma}_t']_x = \begin{cases} \vec{R}_{\hat{r}}([\vec{\sigma}_t]_x), & \text{if } x \in C \\ [\vec{\sigma}_t]_x, & \text{otherwise.} \end{cases} \tag{4.46}$$

The reflected spin is again

$$\vec{R}_{\hat{r}}([\vec{\sigma}_t]_x) = [\vec{\sigma}_t]_x - 2(\hat{r} \cdot [\vec{\sigma}_t]_x)\hat{r}. \tag{4.27}$$

7: The new element of $\boldsymbol{X}$, i_{t+1}, is the following field configuration,

$$[\vec{\sigma}_{t+1}]_x = \begin{cases} \vec{R}_{\hat{r}}([\vec{\sigma}_t]_x), & \text{if } x \in C \text{ for some } C \in \mathscr{C}_R \\ [\vec{\sigma}_t]_x, & \text{otherwise.} \end{cases} \tag{4.28}$$

8: Return to steps 2.

5 Results

We simulate the lattice-regularized 3d O(4) non-linear σ model with a chemical potential on a regular cubic lattice with periodic boundary conditions. We perform simulations with eighteen chemical potentials (see Tab. 5.1).

We simulate the model on eleven lattice sizes (on a set of eleven lattice sizes at $\mu_{B,\mathrm{lat}} = 0$ and on a subset of four lattice sizes at $\mu_{B,\mathrm{lat}} > 0$) (see Tab. 5.2). The physical units of the lattice sizes are estimated with the relation (2.72) (see Tab. 5.3). The volume of each lattice is L^3.

At each $\mu_{B,\mathrm{lat}}$ we employ a temperature range that captures the critical temperature.

The magnetic susceptibility, specific heat, topological susceptibility and autocorrelation times have maxima at each pair of L and $\mu_{B,\mathrm{lat}}$ values (for L large enough). We call "pseudo critical" temperatures the temperatures at which these maxima occur.

In this chapter we present plots of our results. Some tables of values are given in Appendix A. Unless otherwise specified, the errors in this chapter and in the appendices were calculated using the jackknife method with 10 bins[1].

$\mu_{B,\mathrm{lat}}$	0	0.1	0.2	0.3	0.4	0.5	0.6	0.7	0.8
	0.9	1	1.1	1.2	1.3	1.4	1.5	2.0	2.5
μ_B[MeV]	0	14.5	29	43.5	58	72.5	87	101.5	116.1
	130.6	145.1	159.6	174.1	188.6	203.1	217.6	290.1	362.7

Table 5.1: *Chemical potentials used in the simulations of this project. In the first and second rows are the chemical potentials in lattice units and in the third and fourth rows in physical units. The physical units are estimated with the relation* (2.70).

L $(\mu_{B,\mathrm{lat}} = 0)$	10	12	14	16	18	19	20	21	22	23	24
L $(\mu_{B,\mathrm{lat}} > 0)$	10	12	16	20							

Table 5.2: *Lattice sizes used in the simulations of this work. In the first row are the lattice sizes used in the case $\mu_{B,lat} = 0$, in the second row are the lattice sizes used in the other cases.*

L_{lat}	10	12	14	16	18	19	20	21	22	23	24
L[fm]	13.6	16.3	19.0	21.8	24.5	25.8	27.2	28.6	29.9	31.3	32.6

Table 5.3: *Lattice sizes used in the simulations of this work. L_{lat} are the lattice units and L[fm] are the respective lattice sizes in fermis. The physical units are estimated with the relation* (2.72).

[1] The jackknife method is described e.g. in references [59; 71].

5.1 Statistics

We measure the autocorrelation times of the magnetization, energy and topological charge, τ_M, τ_E and τ_Q respectively. The autocorrelation times were calculated at each triad of parameters β_{lat}, L and $\mu_{B,\text{lat}}$, see Sec. 5.2. In most of the cases the largest autocorrelation time is τ_M and the smallest is τ_Q. The autocorrelation time τ_Q is not larger as a benefit of the cluster algorithm; the correlation of the topological charge measurements is often a big problem with other algorithms. Thermalization times were at least 10^4 and at most $10^3\tau_M$ sweeps (the maximum of these two values).[2] The observables were measured in intervals of $2\tau_{\mathbb{O}}$, where $\tau_{\mathbb{O}}$ is the largest of τ_M, τ_E and τ_Q, which can be considered safe to autocorrelation effects.

The statistics are not constant, it depends on the maximal autocorrelation time at each triad of parameters β_{lat}, L and $\mu_{B,\text{lat}}$. The minimum statistics in all cases are 10^4 measurements. For $L = 20$, the statistics are given in Appendix A.

5.2 Autocorrelation times

In this section we present the autocorrelation times of the magnetization, energy and topological charge, τ_M, τ_E and τ_Q respectively (see Sec. 3.6). To calculate these autocorrelation times, we take the values of the observables in a field configuration of the Markov chain as the temporary values of the observables (see Sec. 3.6). We take one sweep as the unit of algorithmic time (the time of the Markov chain, see Chap. 4).

Figs. 5.1, 5.2 and 5.3 show the autocorrelation times at different values of $\mu_{B,\text{lat}}$ in a lattice of volume 20^3. The maximal autocorrelation times increase rapidly, and the pseudo critical temperatures move toward larger β_{lat} values, as $\mu_{B,\text{lat}}$ grows.

Figs. 5.4, 5.5 and 5.6 show the autocorrelation times at different values of $\mu_{B,\text{lat}}$ and lattice volumes. At fixed $\mu_{B,\text{lat}}$ the maxima of the autocorrelation times grow, and the pseudo critical temperatures move to larger β_{lat} values, as L grows.

The autocorrelation time τ_Q is nearly zero at $\mu_{B,\text{lat}} = 0.1$, but as $\mu_{B,\text{lat}}$ grows it increases rapidly to values closer to the other two autocorrelation times. The non-local updates of the field configurations in the multicluster algorithm diminish the autocorrelation times, particularly the autocorrelation time τ_Q.

The autocorrelation times are algorithm properties. With our algorithm, the maxima of the autocorrelation times grow rapidly as L or $\mu_{B,\text{lat}}$ increases. Furthermore, as the temperature approaches the pseudo critical temperature at fixed $\mu_{B,\text{lat}}$, the autocorrelation time increases exponentially. Both effects of increasing autocorrelation times are evidence of a persistent critical slowing down effect in our algorithm, although this effect is less pronounced than in local update algorithms.

As we mention in Sec. 3.6, the autocorrelation time in a finite size lattice at T_c increase as L^z, where z is the dynamical critical exponent, and in the thermodynamic limit the autocorrelation times diverge at T_c. Thus the autocorrelation times are also criteria to find the critical temperature.

The largest autocorrelation time in our data set is $\tau_M = 1218(21)$ sweeps at $\beta_{\text{lat}} = 1.15$, $L = 20$ and $\mu_{B,\text{lat}} = 2.5$. This autocorrelation time sets the limit of the chemical potential in this project at $\mu_{B,\text{lat}} = 2.5$. The simulations at $\mu_{B,\text{lat}} = 2.5$ and $L = 20$ takes 42 days with 50 simultaneous jobs[3] running on Intel Xeon E5-2690 v3 processors, whose base frequency is 2.60 GHz.

[2] One sweep in the multicluster algorithm is the update of all the spins on the lattice, it corresponds to steps 2 to 7 of the MCMC 4.

[3] A job is a process running on a CPU.

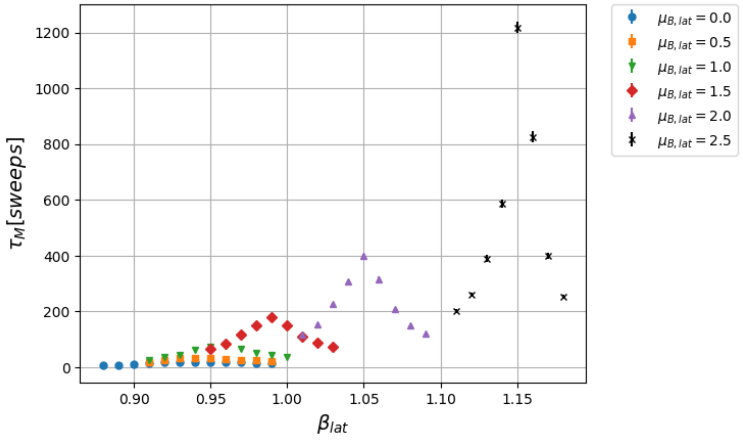

Figure 5.1: *Autocorrelation time of the magnetization at $\mu_{B,lat}$ = 0, 0.5, 1, 1.5, 2 and 2.5, in a lattice of volume 20^3.*

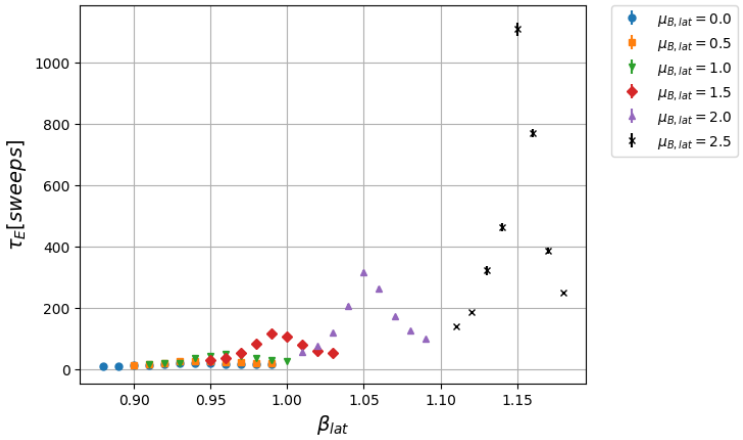

Figure 5.2: *Autocorrelation time of the energy at $\mu_{B,lat}$ = 0, 0.5, 1, 1.5, 2 and 2.5, in a lattice of volume 20^3.*

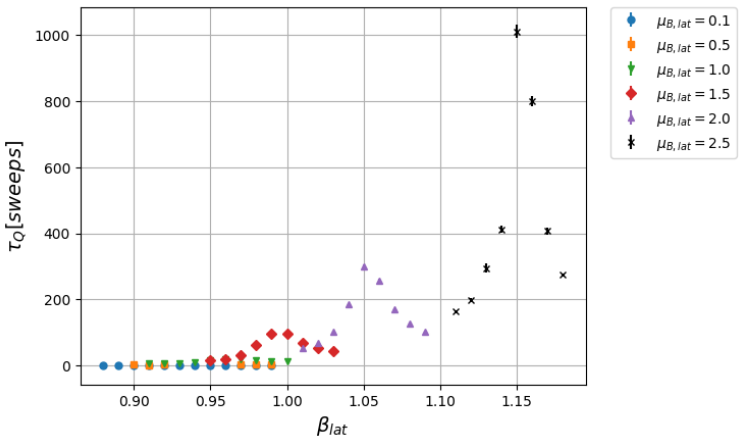

Figure 5.3: *Autocorrelation time of the topological charge at $\mu_{B,lat}$ = 0.1, 0.5, 1, 1.5, 2 and 2.5, in a lattice of volume 20^3.*

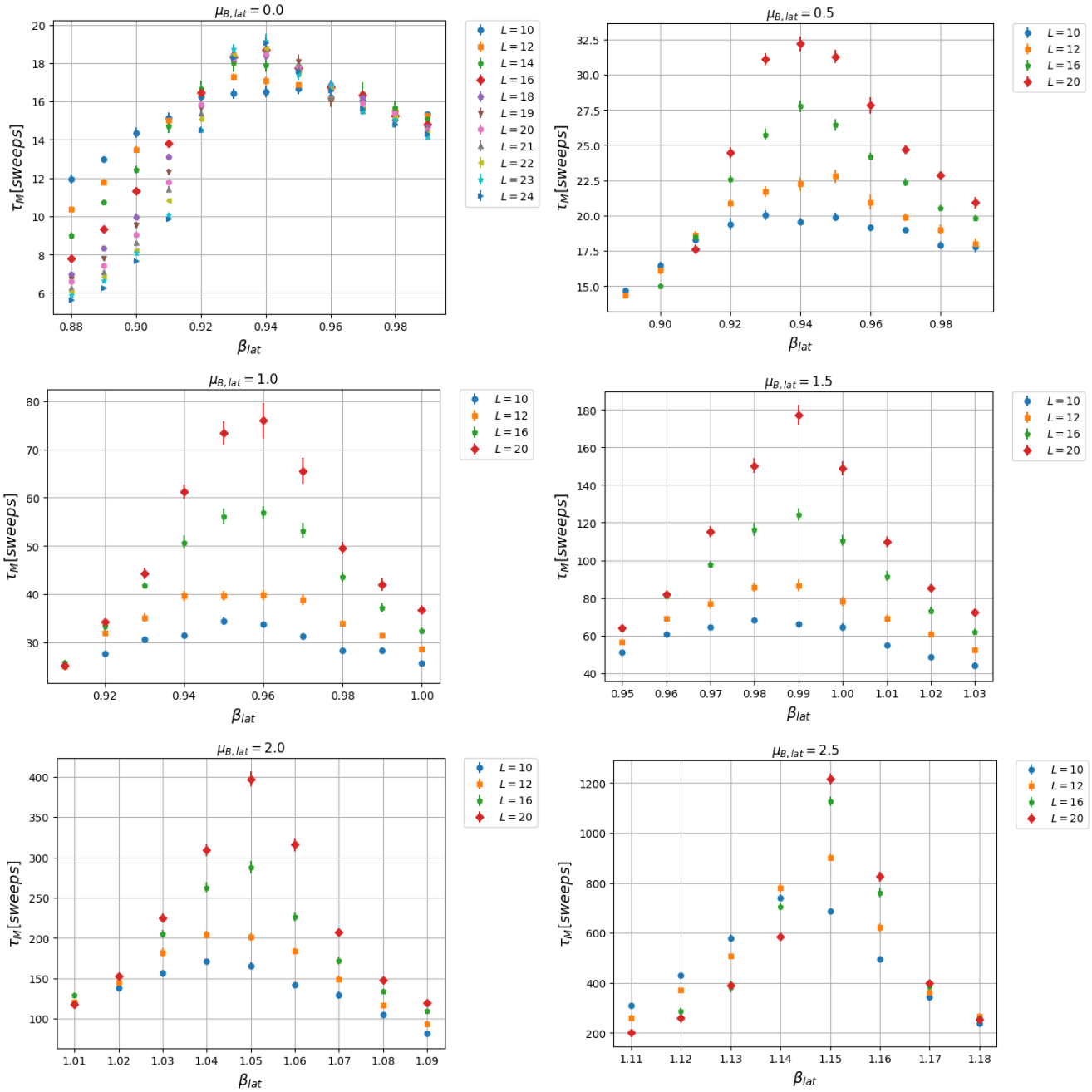

Figure 5.4: *Autocorrelation time of the magnetization at* $\mu_{B,lat} = 0.0, 0.5, 1.0, 1.5, 2.0$ *and* 2.5*, in lattices of volumes* L^3*.*

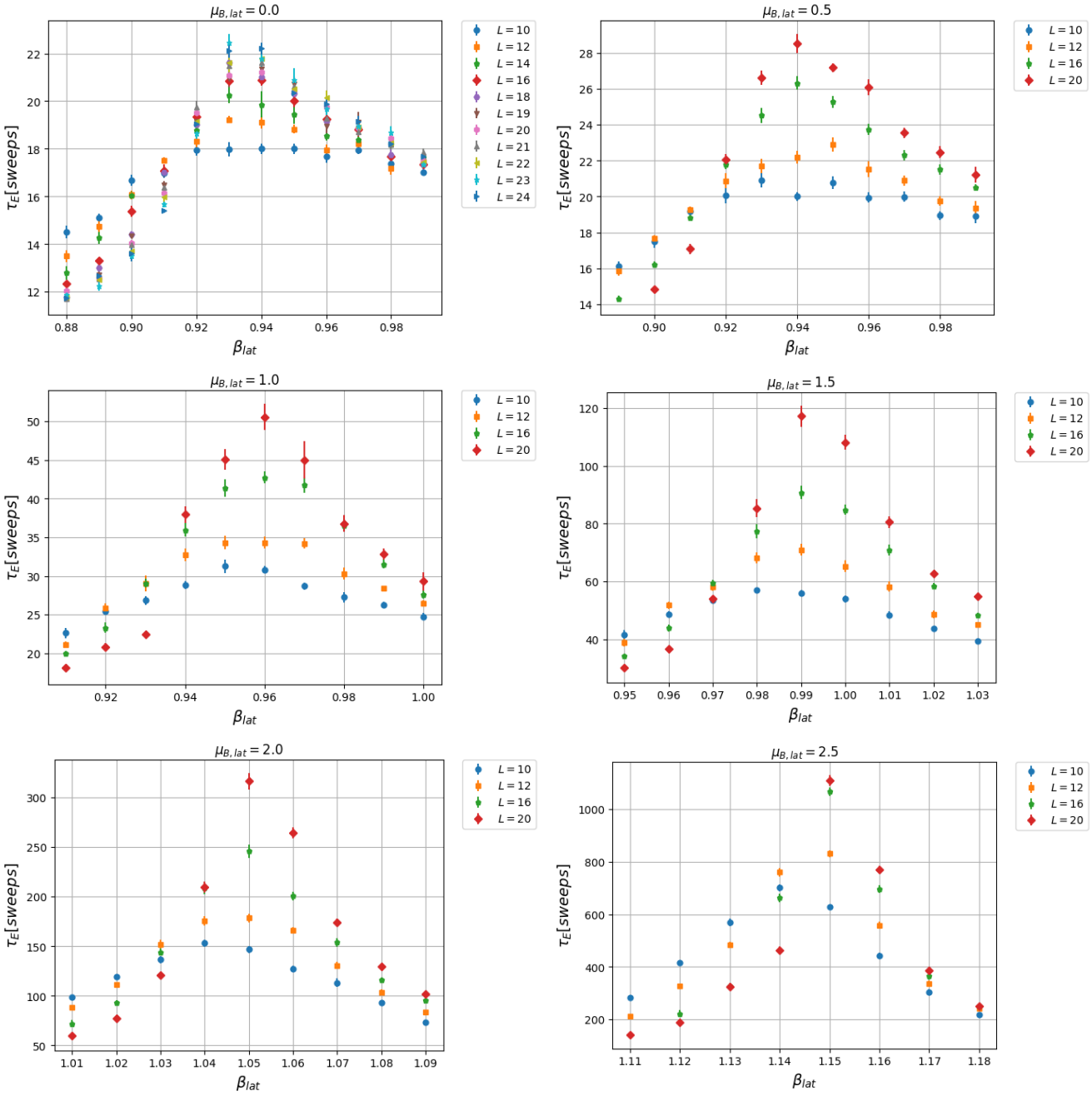

Figure 5.5: *Autocorrelation time of the energy at* $\mu_{B,lat} = 0.0, 0.5, 1.0, 1.5, 2.0$ *and* 2.5*, in lattices of volumes* L^3.

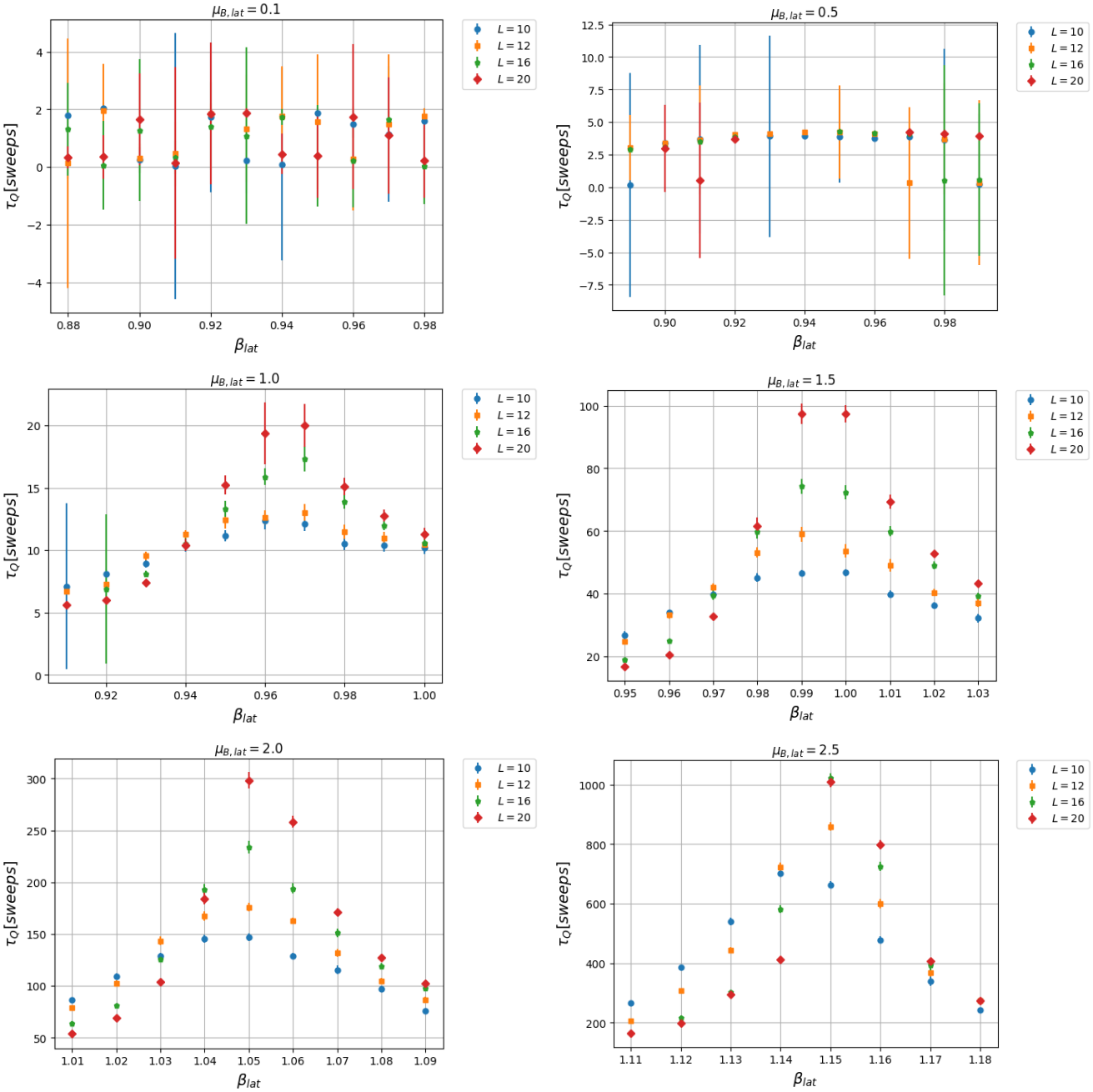

Figure 5.6: *Autocorrelation time of the topological charge at* $\mu_{B,lat}$ = 0.1, 0.5, 1.0, 1.5, 2.0 *and* 2.5, *in lattices of volumes* L^3.

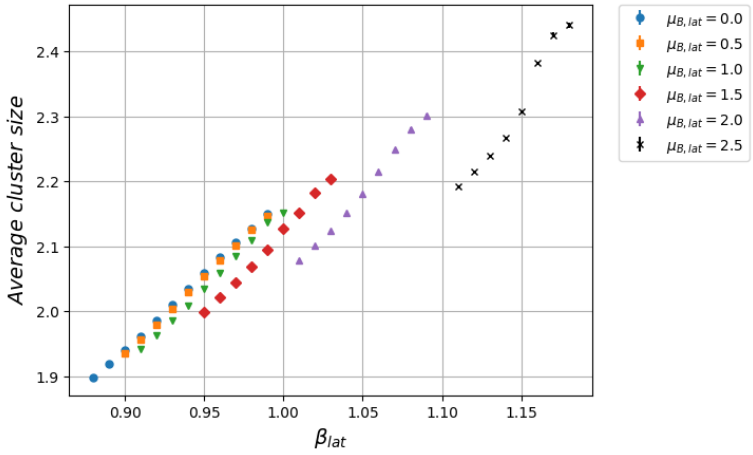

Figure 5.7: *Average cluster size at $\mu_{B,lat}$ = 0, 0.5, 1, 1.5, 2 and 2.5, in a lattice of volume 20^3.*

5.3 Average cluster size

The average cluster size is the average number of spins in the clusters formed in the multicluster part of our algorithm (see Sec. 4.3.3). Fig. 5.7 shows the average cluster size in a lattice of volume 20^3 at different chemical potentials. As the temperature increases the cluster size decreases and the opposite. At fixed β_{lat}, the effect of increasing the chemical potential is a reduction in the average cluster size; when $\mu_{B,\text{lat}}$ increases at fixed β_{lat} the reflection probability of the clusters decreases (see Sec. 4.4), which favors smaller average cluster sizes. We do not find a large difference in the average cluster size when the volume of the lattice is changed.

5.4 Acceptance rate

The acceptance rate is the rate at which a cluster reflection is accepted in our algorithm (see Sec. 4.4). Fig. 5.8 shows the acceptance rate at different chemical potentials in a lattice of volume 20^3. At fixed L and β_{lat}, the effect of increasing the chemical potential is a decrease in the acceptance rate. However, we observe that the $\mu_{B,\text{lat}}$ effect diminishes as β_{lat} increases.

Fig. 5.9 shows the acceptance rates at approximately constant topological charge densities q and non-fixed $\mu_{B,\text{lat}}$ in a lattice of volume 20^3. In this graph the chemical potential increases from left to right. We observe that the points with approximately equal topological charge densities also have approximately equal acceptance rates, apparently the acceptance rate does not depend much on temperature or chemical potential.

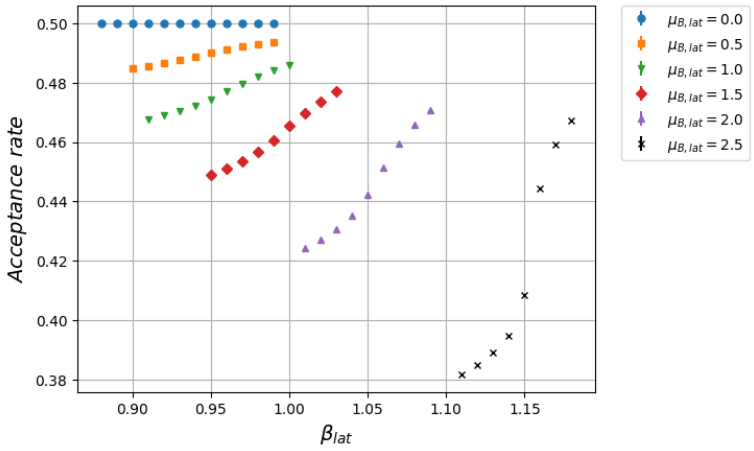

Figure 5.8: *Acceptance rate of reflected clusters at $\mu_{B,lat}$ = 0, 0.5, 1, 1.5, 2 and 2.5, in a lattice of volume 20^3.*

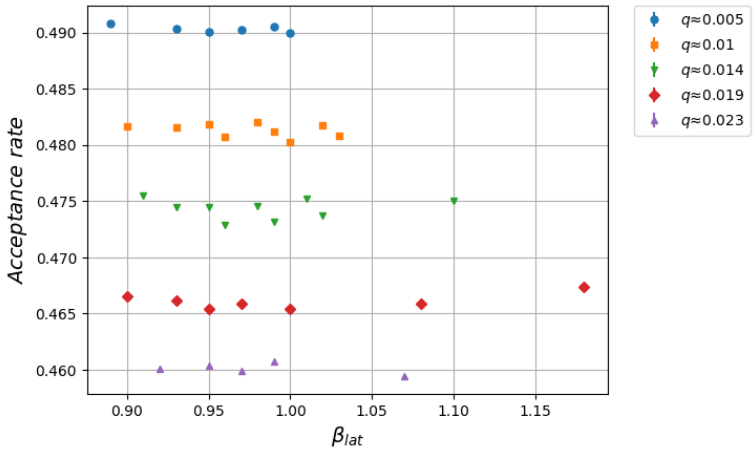

Figure 5.9: *Acceptance rate at approximately constant topological charge densities q and non-fixed $\mu_{B,lat}$ in a lattice of volume 20^3. The chemical potential increases from left to right. The points with approximately equal topological charge density have approximately equal chemical potential, despite its chemical potential or temperature.*

5.5 Magnetization density

The magnetization density (denoted by m, see Eq. (3.28)) is shown in Fig. 5.10 at different chemical potentials in a lattice of volume 20^3. Increasing the chemical potential at fixed β_{lat} causes a decrease in the magnetization density, therefore, as $\mu_{B,\text{lat}}$ increases the field configurations are more disordered (less similar to parallel field configurations). This is related to the decrease in the average cluster size seen in Sec. 5.3.

The slope of this observable (in a small neighborhood of the pseudo critical temperatures of the specific heat) increases with $\mu_{B,\text{lat}}$. The magnetization density increasingly resembles a first order phase transition as $\mu_{B,\text{lat}}$ grows. This may be an indication of a first order phase transition at $\mu_{B,\text{lat}}$ larger than 2.5.

5.6 Root mean square magnetization

The root mean square magnetization (represented by M_{rms}, see Eq. (3.41)) at volume 20^3 and several values of $\mu_{B,\text{lat}}$ is shown in Fig. 5.11. At a fixed triad of parameters L, β_{lat} and $\mu_{B,\text{lat}}$, the values of M_{rms} and m almost coincide. The larger differences between these two observables are located near the pseudo critical temperatures of the specific heat.

5.7 Energy density

The energy density (denoted by ϵ, see Eq. (3.29)) in a lattice of volume 20^3 at several chemical potentials is shown in Fig. 5.12. The effect of increasing $\mu_{B,\text{lat}}$ at fixed β_{lat} is an increase in the energy density; increasing the chemical potential at fixed β_{lat} generates more disordered field configurations (as we mention in Sec. 5.5) and therefore larger energy configurations.

Again we observe an increase in the slope of this observable (in a small neighborhood of the pseudo critical temperatures of the specific heat) as $\mu_{B,\text{lat}}$ increases. This may be another indication of a first order phase transition at larger $\mu_{B,\text{lat}}$ values.

5.8 Magnetic susceptibility

Fig. 5.13 shows the magnetic susceptibility (represented by χ_M, see Eq. (3.31)) in a volume 20^3 at different chemical potentials. As $\mu_{B,\text{lat}}$ increases, the peak of the plot is narrower and higher, and the pseudo critical temperature changes to larger β_{lat} values. Increasingly narrower and higher peaks in the plot may be an indication of a first order phase transition at larger $\mu_{B,\text{lat}}$ values.

Fig. 5.14 shows some plots of χ_M at different $\mu_{B,\text{lat}}$ values. The maxima grow as L increases. At fixed $\mu_{B,\text{lat}}$, the growth behavior corresponds to $L^{\gamma/\nu}$, where γ and ν are critical exponents, which is an indication of a second order phase transition. Again at fixed chemical potential, the pseudo critical temperatures move toward larger β_{lat} values.

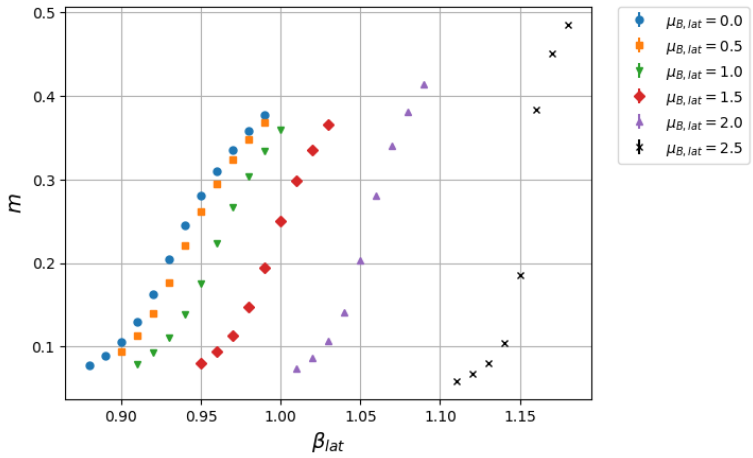

Figure 5.10: *Magnetization density at $\mu_{B,lat}$ = 0, 0.5, 1, 1.5, 2 and 2.5, in a lattice of volume 20^3.*

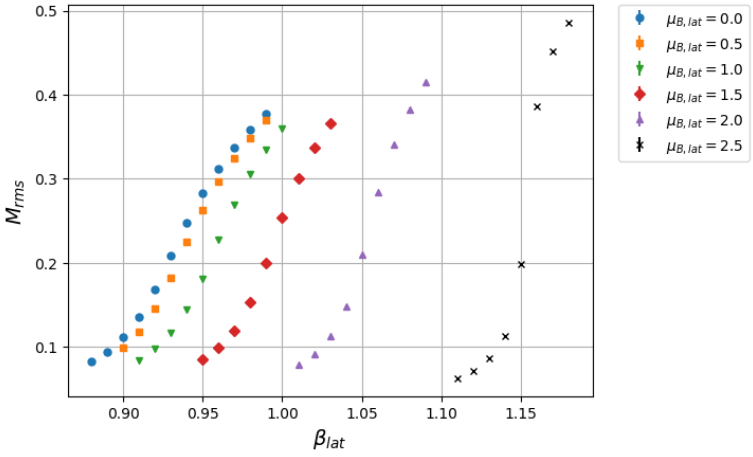

Figure 5.11: *Root mean square magnetization at $\mu_{B,lat}$ = 0, 0.5, 1, 1.5, 2 and 2.5, in a lattice of volume 20^3.*

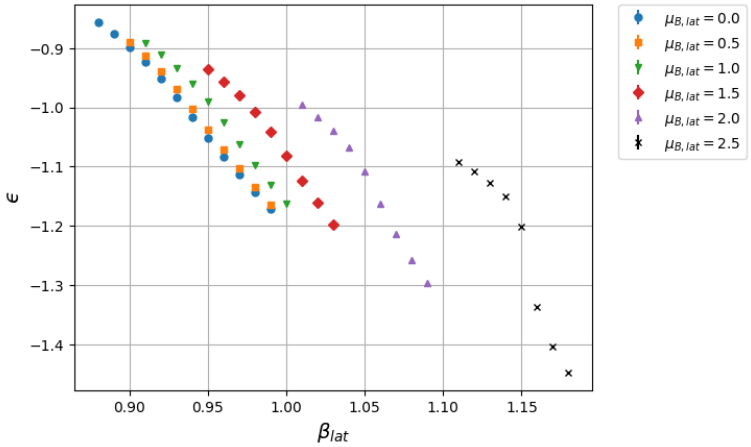

Figure 5.12: *Energy density at $\mu_{B,lat}$ = 0, 0.5, 1, 1.5, 2 and 2.5, in a lattice of volume 20^3.*

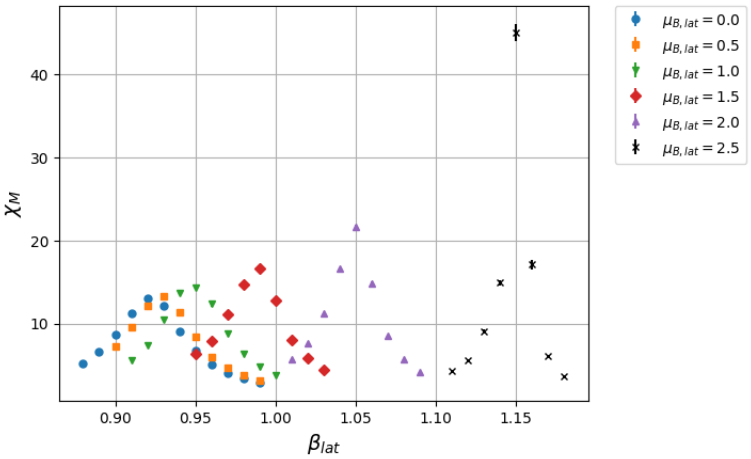

Figure 5.13: *Magnetic susceptibility at $\mu_{B,lat}$ = 0, 0.5, 1, 1.5, 2 and 2.5, in a lattice of volume 20^3.*

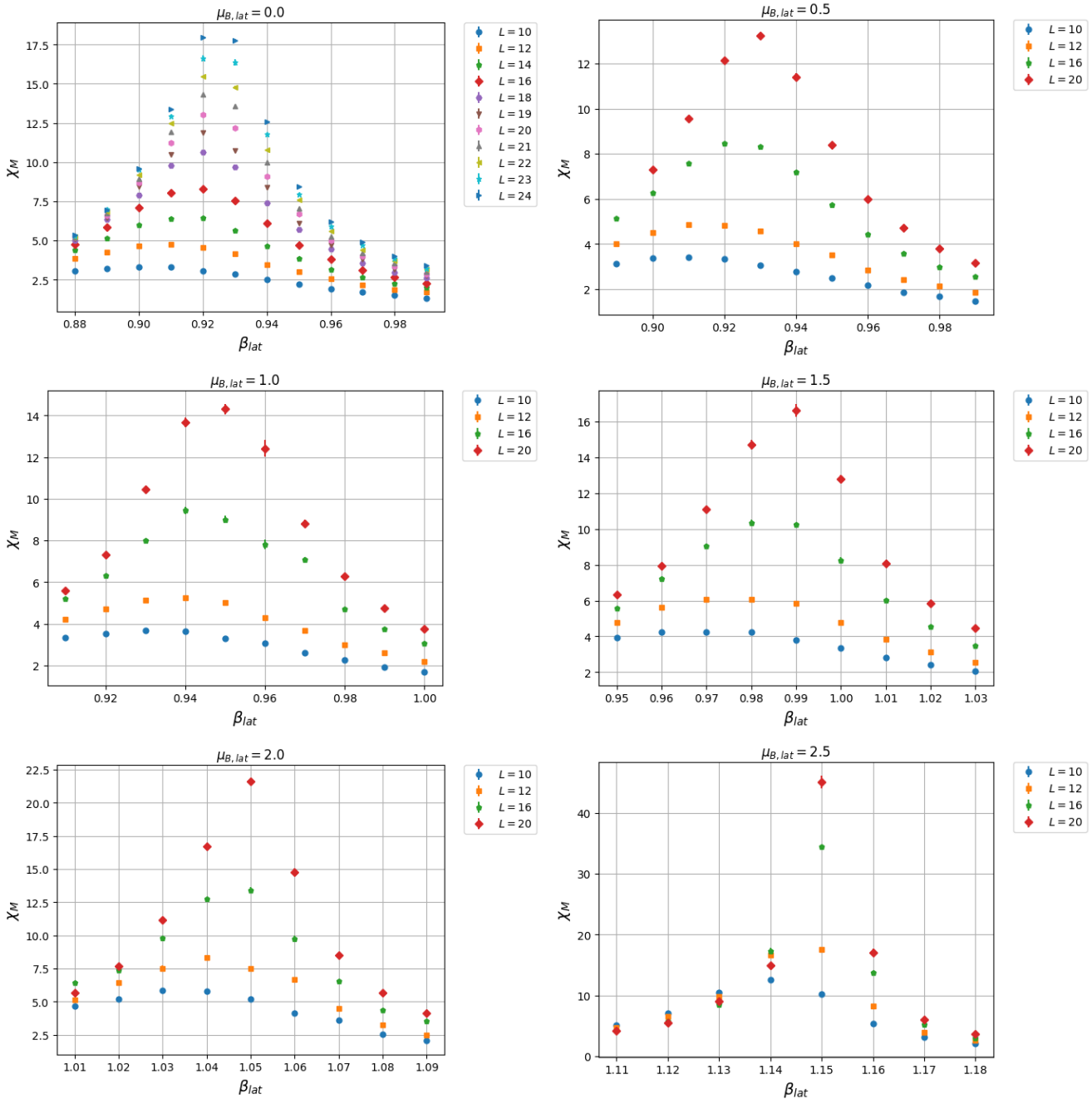

Figure 5.14: *Magnetic susceptibility at* $\mu_{B,lat}$ = 0, 0.5, 1, 1.5, 2 *and* 2.5, *in lattices of volumes* L^3.

5.9 Specific heat

Fig. 5.15 shows the specific heat (denoted by c_V, see Eq. (3.32)) at different values of $\mu_{B,\mathrm{lat}}$ and lattice volumes. At fixed $\mu_{B,\mathrm{lat}}$, the growth behavior does not corresponds to $L^{\alpha/\nu}$ for all the $\mu_{B,\mathrm{lat}}$ values, this can be an artifact of our β_{lat} spacing; the steps of 0.01 units in β_{lat} do not capture the critical temperature well enough. Due to this, the critical exponents ratio α/ν cannot be obtained properly in all the cases.

Fig. 5.16 shows the specific heat at some values of $\mu_{B,\mathrm{lat}}$ and lattice size 20^3. As $\mu_{B,\mathrm{lat}}$ increases, the peak of the plot is narrower and higher, and the pseudo critical temperature changes to larger β_{lat} values. Again, increasingly narrower and higher peaks in the specific heat plot may be an indication of a first order phase transition at larger $\mu_{B,\mathrm{lat}}$ values.

5.10 Topological charge density

The topological charge density (denoted by q, see Eq. (3.30)) is shown at different chemical potentials in a lattice of volume 20^3 in Fig. 5.17. At $\mu_{B,\mathrm{lat}} = 0$ the theoretical topological charge density is zero, which was used as a consistency test in previous works [41; 31]. The effect of increasing $\mu_{B,\mathrm{lat}}$ at fixed β_{lat} is an increase of the topological charge density.

The slope of the topological charge density (near the pseudo critical temperatures of the specific heat) grows with $\mu_{B,\mathrm{lat}}$. In this case this is clearer than in the magnetization and energy at the respective chemical potential and lattice size values. As in the magnetization and energy cases, this is an indication of two topological charge density phases. Below $\mu_{B,\mathrm{lat}} = 2$ the phase transition is of the second order. The data at $\mu_{B,\mathrm{lat}} = 2.5$ resemble a first order phase transition.

5.11 Topological susceptibility

Fig. 5.18 shows the topological susceptibility (represented by χ_Q, see Eq. (3.33)) at some chemical potentials and lattice size 20^3. As $\mu_{B,\mathrm{lat}}$ increases, the peak of the plot is narrower and higher. Again, this may be an indication of a first order phase transition at larger $\mu_{B,\mathrm{lat}}$ values. Furthermore, as the chemical potential grows the pseudo critical temperature of this observable changes to larger β_{lat} values and it is in better agreement to the pseudo critical temperatures of c_V and χ_M.

Fig. 5.19 shows χ_Q at different values of $\mu_{B,\mathrm{lat}}$ and lattice volumes. The maximal of this observable is not well identified in our data set until $\mu_{B,\mathrm{lat}} = 0.9$, but only from $\mu_{B,\mathrm{lat}} = 1.1$ the maximal is clearly visible in all our lattice volumes (see Tab. 5.2).

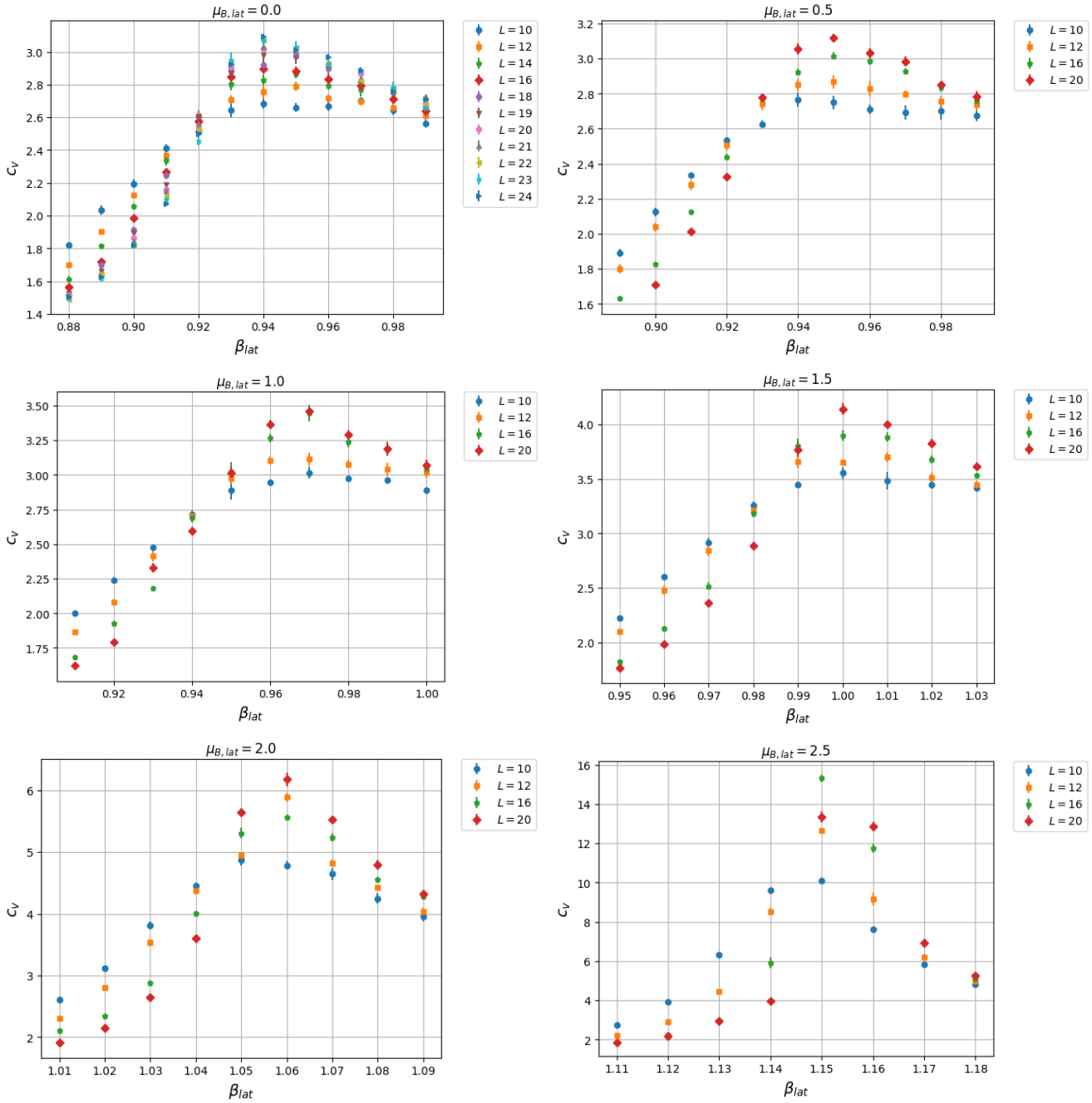

Figure 5.15: *Specific heat at* $\mu_{B,lat}$ = 0, 0.5, 1, 1.5, 2 *and* 2.5, *in lattices of volumes* L^3.

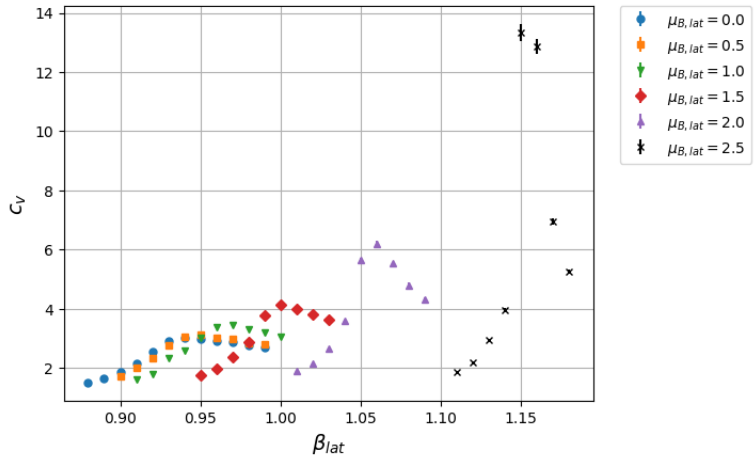

Figure 5.16: *Specific heat at $\mu_{B,lat}$ = 0, 0.5, 1, 1.5, 2 and 2.5, in a lattice of volume 20^3.*

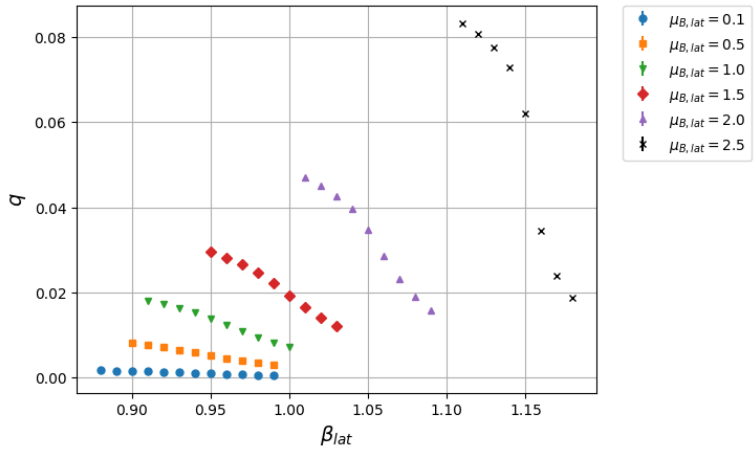

Figure 5.17: *Topological charge density at $\mu_{B,lat}$ = 0.1, 0.5, 1, 1.5, 2 and 2.5, in a lattice of volume 20^3.*

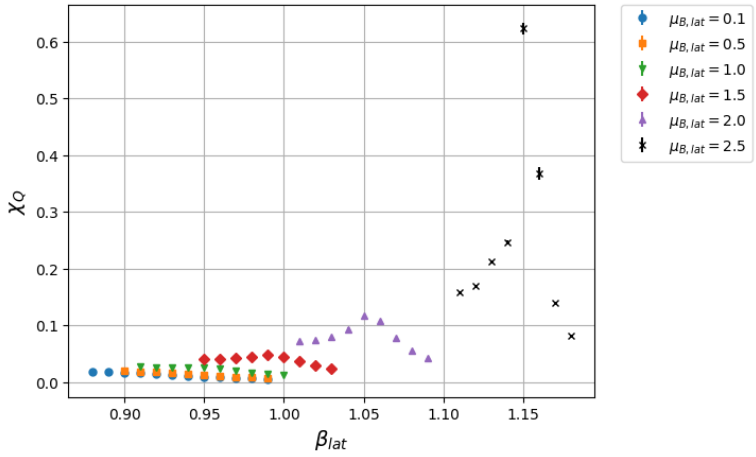

Figure 5.18: *Topological susceptibility at $\mu_{B,lat}$ = 0.1, 0.5, 1, 1.5, 2 and 2.5, in a lattice of volume 20^3.*

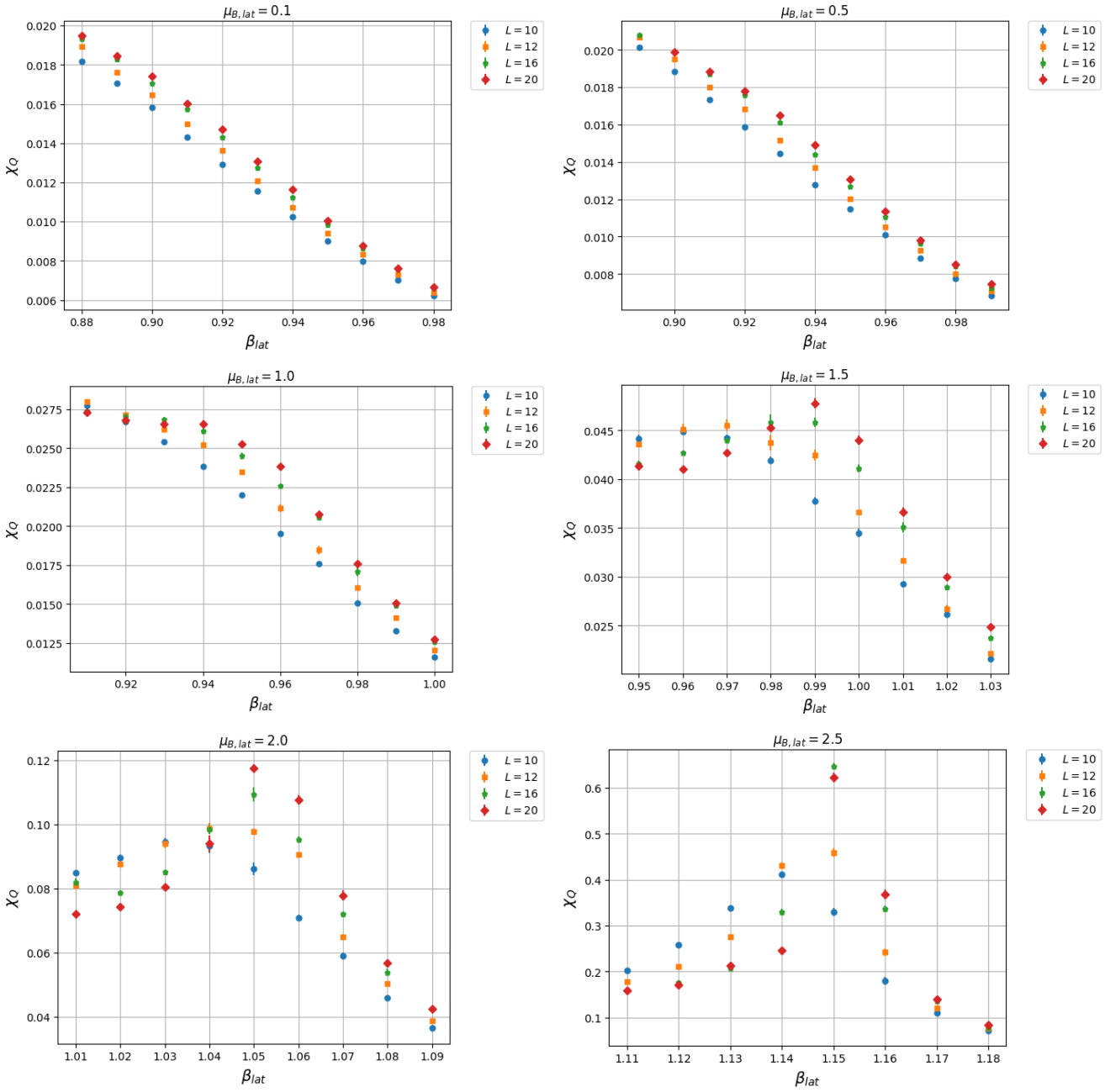

Figure 5.19: *Topological susceptibility at* $\mu_{B,lat}$ = 0.1, 0.5, 1.0, 1.5, 2.0 *and* 2.5.

5.12 Correlation lengths

Fig. 5.20 shows the correlation length and second moment correlation length (denoted by ξ and $\xi_{2\text{nd}}$ respectively, see Eqs. (3.37) and (3.38)) at different chemical potentials in a lattice of volume 20^3. Near $\mu_{B,\text{lat}} = 0$ both observables are nearly identical, the difference between them grows with $\mu_{B,\text{lat}}$, although they remain compatible within the errors.

The errors in both observables were calculated using the jackknife method, the errors of the $\xi_{2\text{nd}}$ values are apparently overestimated.

The quotient L/ξ is shown in Fig. 5.21 at some chemical potentials in a lattice of volume 20^3. As L/ξ decreases the finite size effects are more relevant. In our data, at the pseudo critical temperatures of the specific heat $L/\xi \gtrsim 1$. Therefore, the scaling functions and critical exponents are affected by the finite size effects, a discrepancy is expected from the exact values.

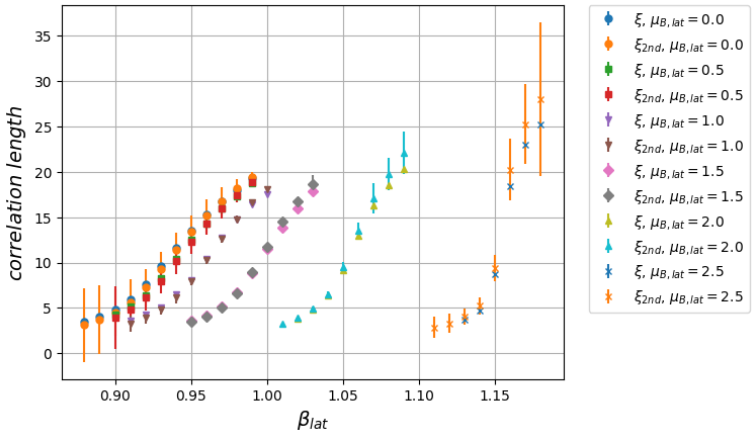

Figure 5.20: *Correlation length and second moment correlation length at $\mu_{B,lat}$ = 0, 0.5, 1, 1.5, 2 and 2.5, in a lattice of volume 20^3.*

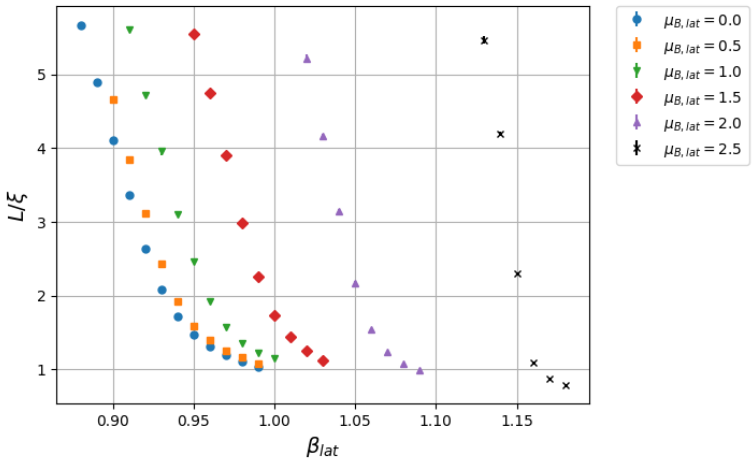

Figure 5.21: *L/ξ at $\mu_{B,lat}$ = 0, 0.5, 1, 1.5, 2 and 2.5, in a lattice of volume 20^3.*

5.13 Statistical distributions

Figs. 5.22, 5.23 and 5.24 show some distributions of the magnetization, energy and topological charge respectively. If the phase transition at $\mu_{B,\mathrm{lat}} = 2.5$ were a first order transition, we would observe double peak distributions, but in the distributions shown below there are only single peaks. At smaller values of $\mu_{B,\mathrm{lat}}$ the distributions also have a single peak. Therefore, under this criterion there are only second order phase transitions up to $\mu_{B,\mathrm{lat}} = 2.5$.

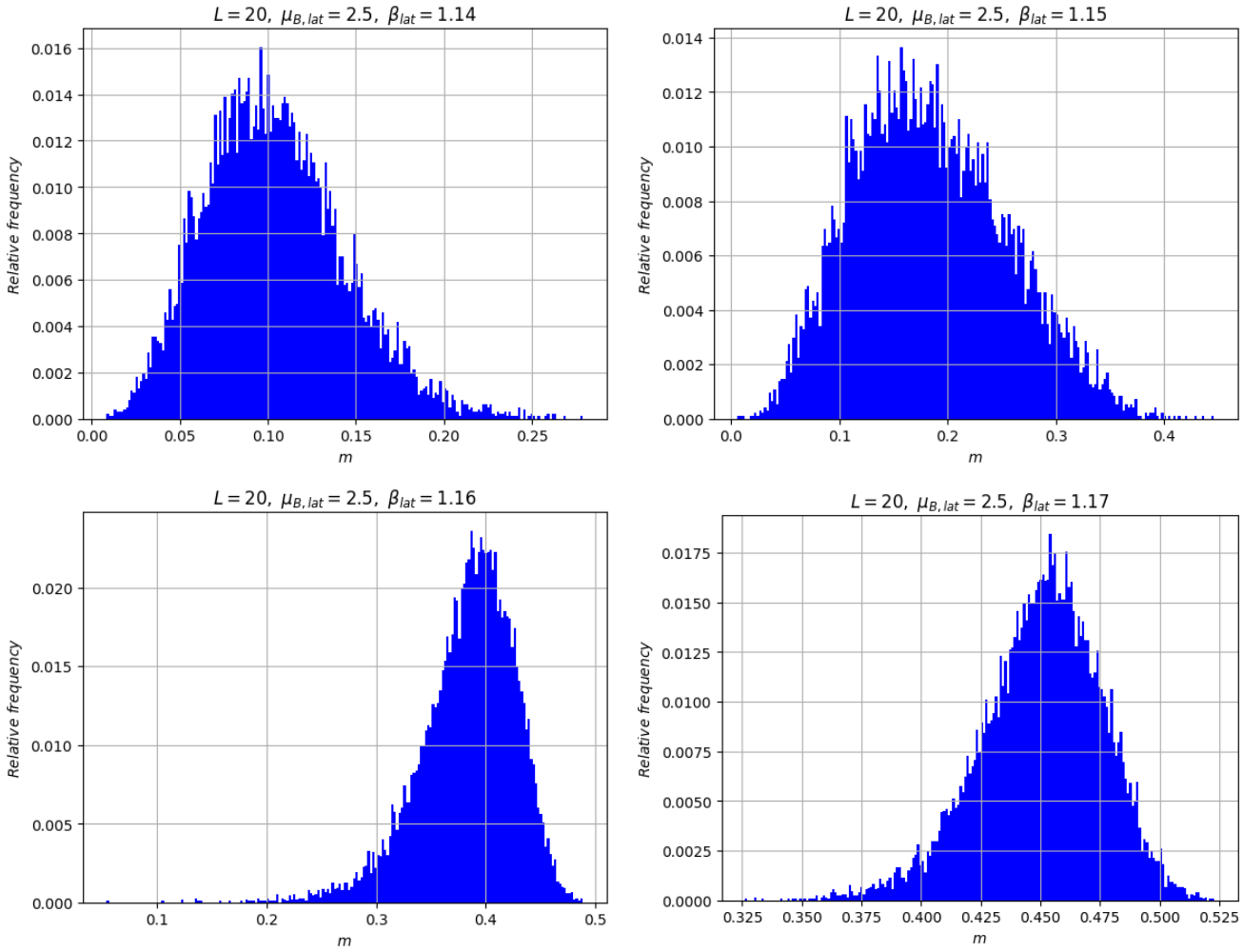

Figure 5.22: *Magnetization density distributions in a lattice of volume* 20^3 *at* $\mu_{B,lat} = 2.5$ *and* $\beta_{lat} = 1.14, 1.15, 1.16$ *and* 1.17.

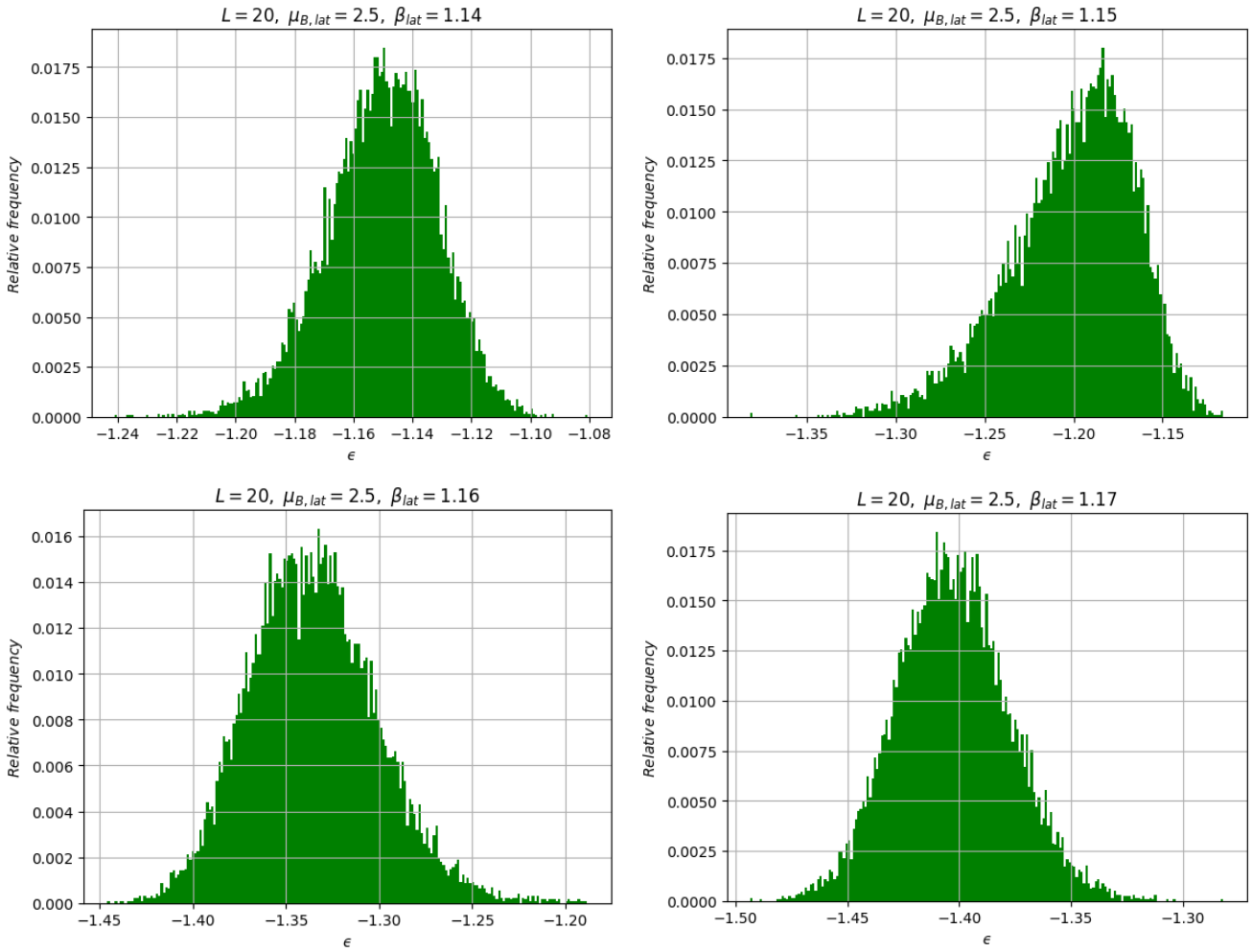

Figure 5.23: *Energy density distributions in a lattice of volume* 20^3 *at* $\mu_{B,lat}$ *= 2.5 and* β_{lat} *= 1.14, 1.15, 1.16 and 1.17.*

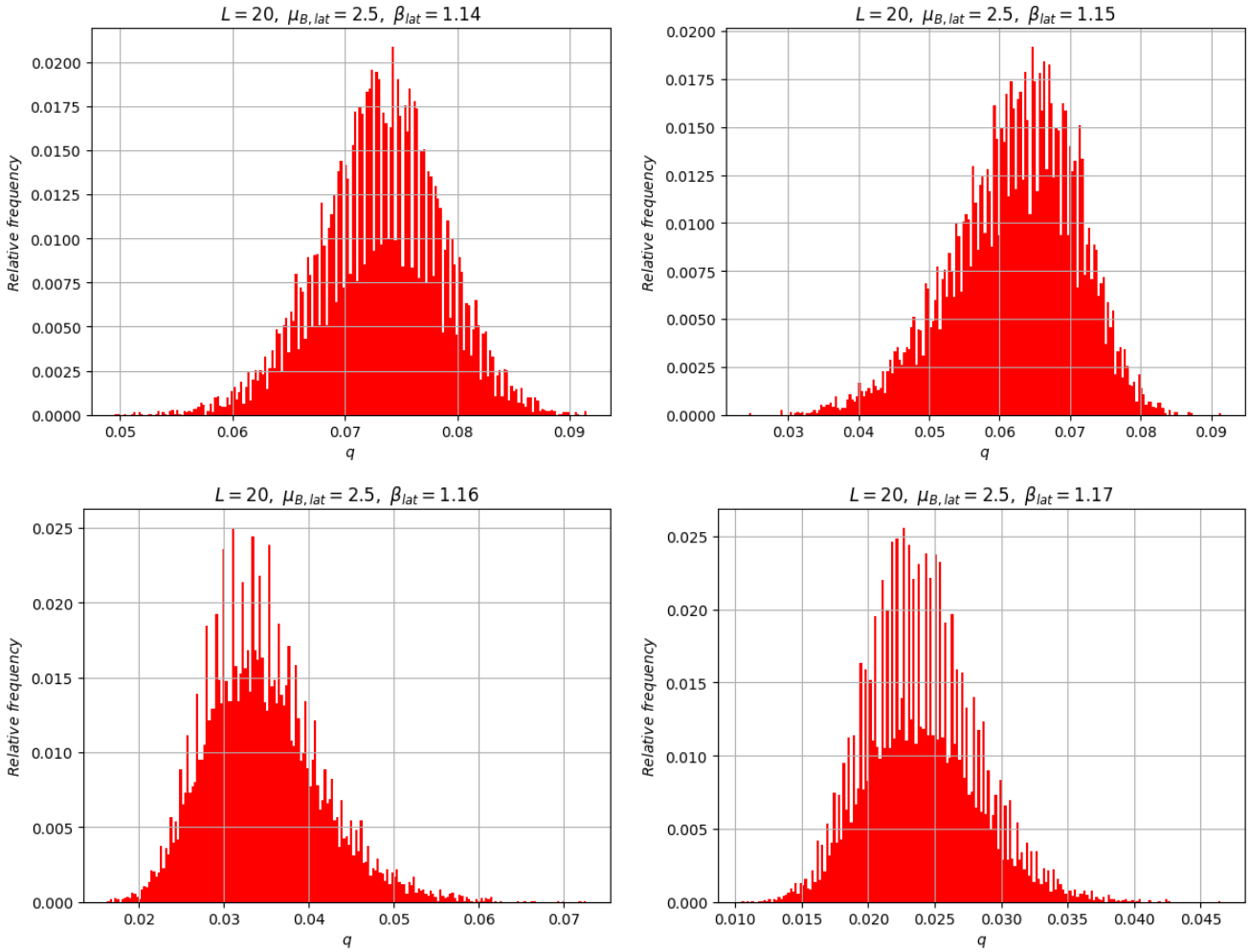

Figure 5.24: *Topological charge density distributions in a lattice of volume* 20^3 *at* $\mu_{B,lat}$ *= 2.5 and* β_{lat} *= 1.14, 1.15, 1.16 and 1.17.*

5.14 Critical exponents

In this section we present the ratios of the critical exponents α/ν, β/ν, γ/ν and x/ν and the dynamical critical exponents z_M, z_E and z_Q.

We introduce phenomenologically the critical exponent x from the observable χ_Q; at the critical temperature, the topological susceptibility scales as

$$\chi_Q(T_c) \propto L^{x/\nu}. \tag{5.1}$$

The dynamical critical exponents have the same subscript as the autocorrelation times from which they were calculated, e.g. z_M is obtained from τ_M.

To obtain the critical exponent from $\mathcal{O}$ we made the fit

$$\mathcal{O}(L, \mu_{B,\mathrm{lat}}, \beta_{\mathrm{lat}}) = cL^b, \tag{5.2}$$

where b and c are the fit parameters. The value of β_{lat} is the closest inverse temperature to the critical temperature in our data set. We use the critical temperatures extrapolated from the observables c_V. The parameter b represents the quotients of critical exponents α/ν, β/ν, γ/ν and x/ν and the dynamical critical exponents z_M, z_E and z_Q, as shown in Eqs. (3.17), (3.18), (3.19), (3.45) and (5.1). The fits were made using all the lattice sizes (see Tab. 5.2).

Figs. 5.25 and 5.26 show the quotients of critical exponents and the dynamical critical exponents up to $\mu_{B,\mathrm{lat}} = 1.5$, our exponents at $\mu_{B,\mathrm{lat}} \geq 2$ are not reliable. All errors were calculated using the jackknife method. Tables of critical exponents for this section are found in Appendix C.

Considering our data is reliable, there is no solid evidence that the chemical potential affects the quotients of critical exponents α/ν, β/ν and γ/ν, in Fig. 5.25 the quotients of critical exponents are compatible with constants. The quotient of critical exponents x/ν and the dynamic critical exponents tend to increase with the chemical potential.

In ref. [72], Engels et al. perform a a high precision study of the critical exponents of the 3d O(4) σ model at $\mu_{B,\mathrm{lat}} = 0$ with lattice sizes from 48^3 to 120^3,[4] which reports the values $\beta = 0.380$, $\gamma = 1.4531$ and $\nu = 0.7377$ at the inverse critical temperature $\beta_{c,\mathrm{lat}} = 0.93590$, therefore

$$\beta/\nu \approx 0.515, \qquad \gamma/\nu \approx 1.970. \tag{5.3}$$

We obtain the following values for these ratios,

$$\beta/\nu = 0.44(1), \qquad \beta/\nu = 0.45(1), \qquad \gamma/\nu = 1.85(2), \tag{5.4}$$

at $\beta_{\mathrm{lat}} = 0.94$, the first β/ν comes from m and the second from M_{rms}. We observe a deviation of approximately 15% and 13% of the β/ν values in Eq. (5.4) from the values in Eq. (5.3). The deviation of the γ/ν value in Eq. (5.4) from the value given in Eq. (5.3) is approximately 6%. As expected, the critical exponents values differ from the exact values due to the finite size effects. Unfortunately our critical exponents are not precise.

[4] These large volumes are possible due to the small autocorrelation time at $\mu_{B,\mathrm{lat}} = 0$, see Fig. 5.1.

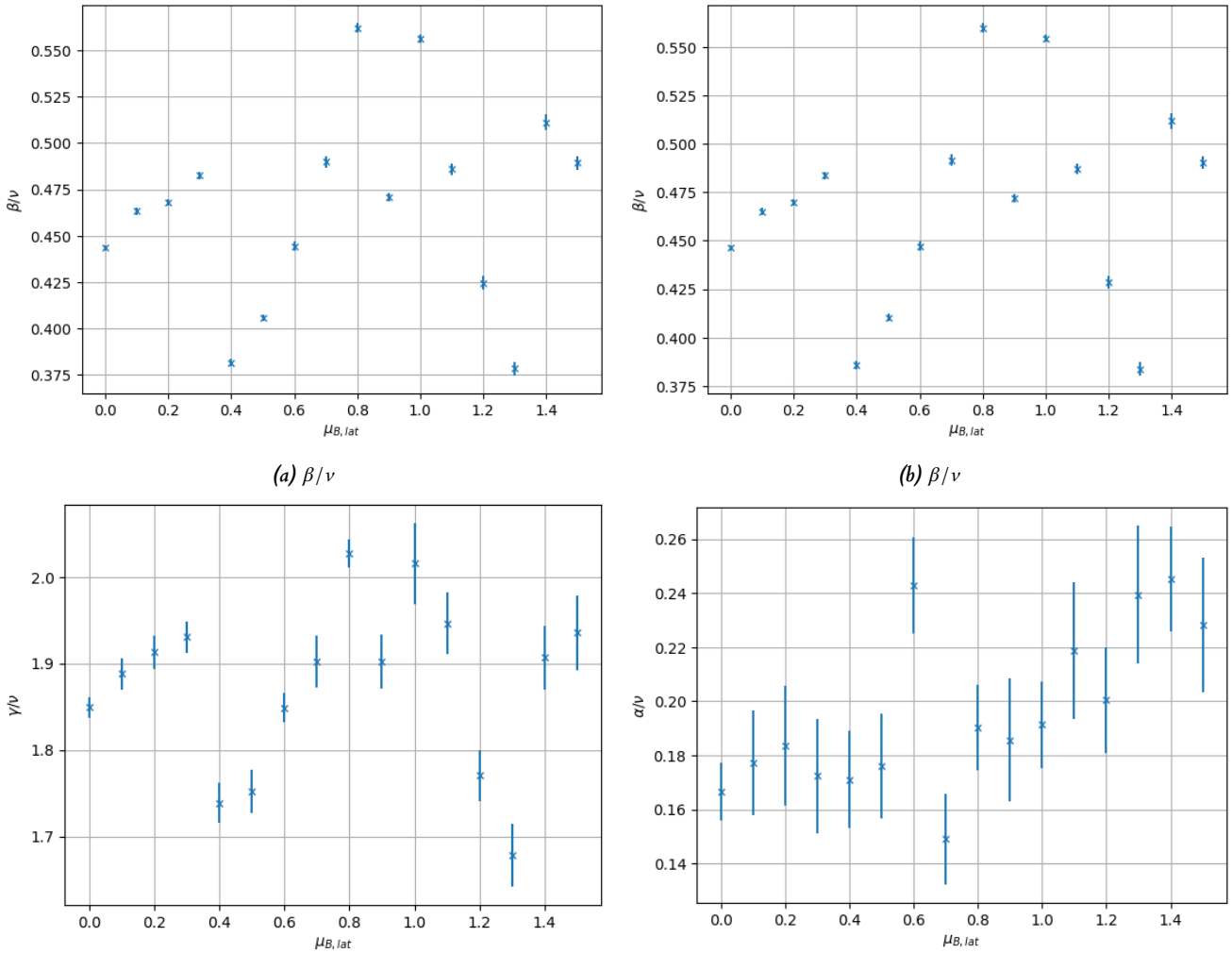

(a) β/ν *(b)* β/ν

(c) γ/ν *(d)* α/ν

Figure 5.25: *Quotients of critical exponents at the closest* β_{lat} *values in our data set from the* $\beta_{c,lat}$ *values extrapolated from the observable* c_V*. (a)* β/ν *obtained from* m*, (b)* β/ν *obtained from* M_{rms}*, (c)* γ/ν *obtained from* χ_M *and (d)* α/ν *obtained from* c_v*.*

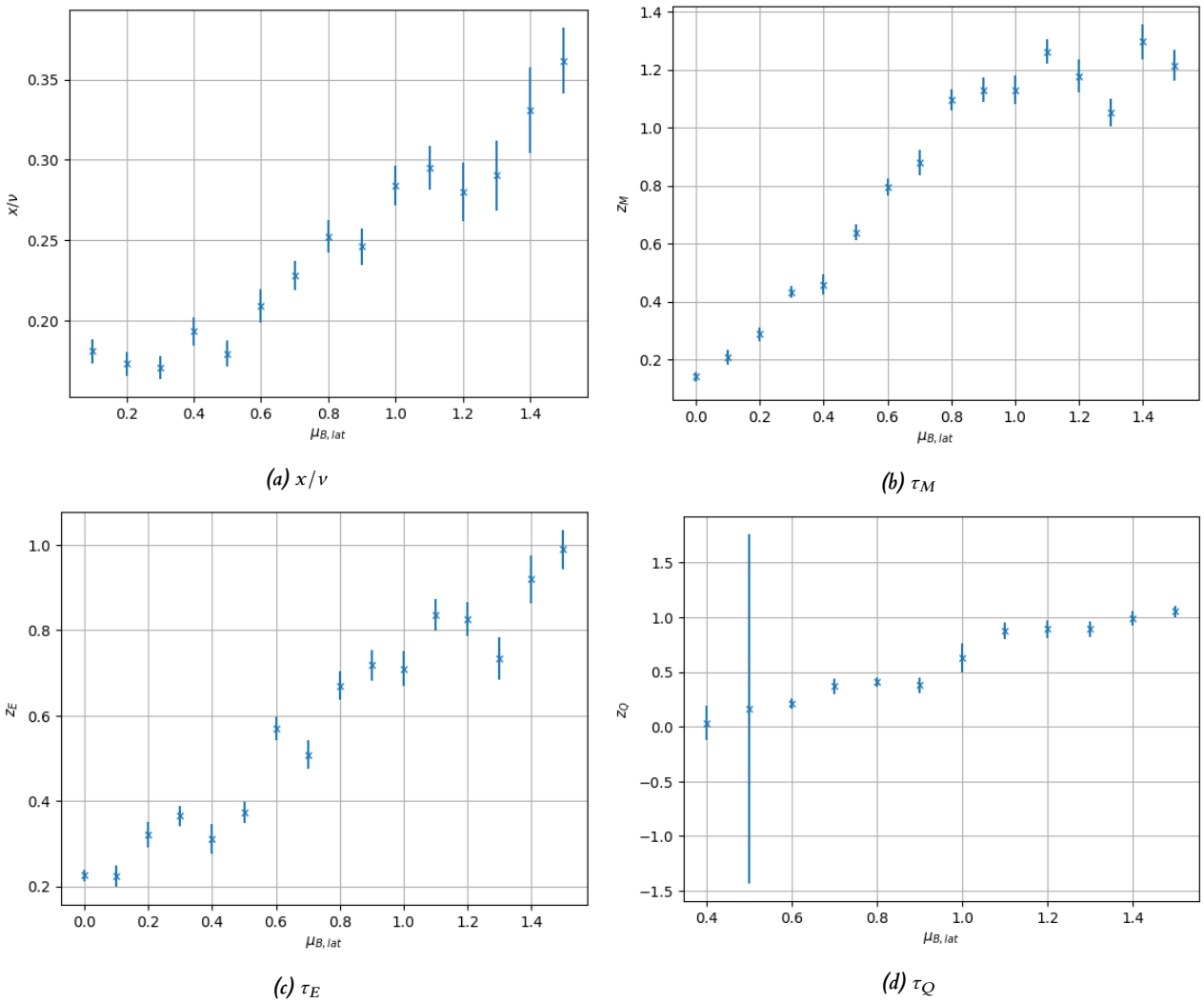

(a) x/ν *(b)* τ_M

(c) τ_E *(d)* τ_Q

Figure 5.26: *Critical exponents at the closest* β_{lat} *values in our data set from the* $\beta_{c,lat}$ *values extrapolated from the observable* c_V*. (a) Quotient of critical exponents* x/ν *obtained from* χ_Q*, (b)* τ_M *obtained from M, (c)* τ_E *obtained from E and (d)* τ_Q *obtained from Q.*

5.15 Phase diagram in lattice units

We present six phase diagrams in lattice units obtained from three observables and three autocorrelation times: χ_M, c_V, χ_Q, τ_M, τ_E and τ_Q. In the thermodynamic limit all these phase diagrams must coincide (except perhaps for the phase diagram of χ_Q).

To obtain the pseudo critical temperatures of each of the observables and autocorrelation times we fit a Johnson unbounded system (S_U) function $J(\beta_{\text{lat}})$ near the maxima of the observables and autocorrelation times, [73]

$$J(\beta_{\text{lat}}) = \frac{\phi}{\sqrt{1+\left(\frac{\beta_{\text{lat}}-\zeta}{\nu}\right)^2}} \exp\left(-\left[\kappa + \rho \sinh^{-1}\left(\frac{\beta_{\text{lat}}-\zeta}{\nu}\right)\right]^2\right), \tag{5.5}$$

where ζ, κ, ν, ρ and ϕ are the fitting parameters. The Johnson S_U function is a non-symmetric modified Gaussian function. We employ this function because the observables and autocorrelation times are similar to Gaussian functions but not symmetric around the peak. Finding the location of the maximum of the Johnson S_U function is nontrivial, we use numerical methods.

Fig. 5.27 shows the observables χ_M and c_V and the fit functions at $\mu_{B,\text{lat}} = 0.1, 1$ and 2.5. We use the χ^2 test as a reference for our fit functions[5]. All the p-values of our fit models are far above 0.05. The lowest p-values for χ_M and c_V are at $\mu_{B,\text{lat}} = 2.5$ and $L = 20$, these are $p = 0.86$ and $p = 0.61$ respectively. Additionally, the plots of the observables and the fit functions are indications that our fits are suitable near the maxima of the observables and autocorrelation times.

The critical temperature $T_{c,\text{lat}}$ is the thermodynamic limit of the pseudo critical temperatures. We extrapolate the thermodynamic limit with the following ansatz,

$$\beta_{\max}(L) = \beta_{c,\text{lat}} + \frac{m}{L}, \tag{5.6}$$

where $\beta_{c,\text{lat}}$ and m are the fitting parameters and L is the number of lattice sites per edge in our cubic lattice.

Fig. 5.28 shows the positions on β_{lat} of the maxima of χ_M and c_V and the linear fitting from Eq. (5.6). The errors of $\beta_{\max}$ were obtained using the jackknife method and the errors of β_c are the parameter fitting errors (obtained with the standard covariance matrix method).

Figs. 5.29 and 5.30 show the phase diagrams in lattice units of the observables and autocorrelation times χ_M, c_V, χ_Q, τ_M, τ_E and τ_Q. To obtain these values we used all the lattice volumes given in Tab. 5.2. The errors are the fit errors of T_c, obtained with the standard covariance matrix method. All the phase diagrams are compatible. The plot of the phase diagram is concave, in agreement with the expected curvature of the phase diagram of QCD [4; 5; 6].

Up to volume 20^3 the observable χ_Q and the autocorrelation time τ_Q do not have clear maxima at small $\mu_{B,\text{lat}}$ in our β_{lat} range. We suppress the phase diagrams of these quantities up to $\mu_{B,\text{lat}} = 1.2$ for χ_Q and $\mu_{B,\text{lat}} = 0.8$ for τ_Q.

Fig. 5.31 shows the phase diagram obtained fitting a constant to the respective $\mu_{B,\text{lat}}$ points of the phase diagrams in Fig. 5.29. This final phase diagram, which represents our final result, shows the fit errors (obtained with the standard covariance matrix method).

[5] Given a threshold value for the χ^2 distribution with n degrees of freedom, or equivalently a minimal p-value p_0 (usually $p_0 = 0.05$), we reject a fit model if its p-value is lower than p_0 [74]. The χ^2 test only allows us to discard a fit model, it is not a measure of goodness of the fit. We use the χ^2 test although it is usually more reliable with larger degrees of freedom.

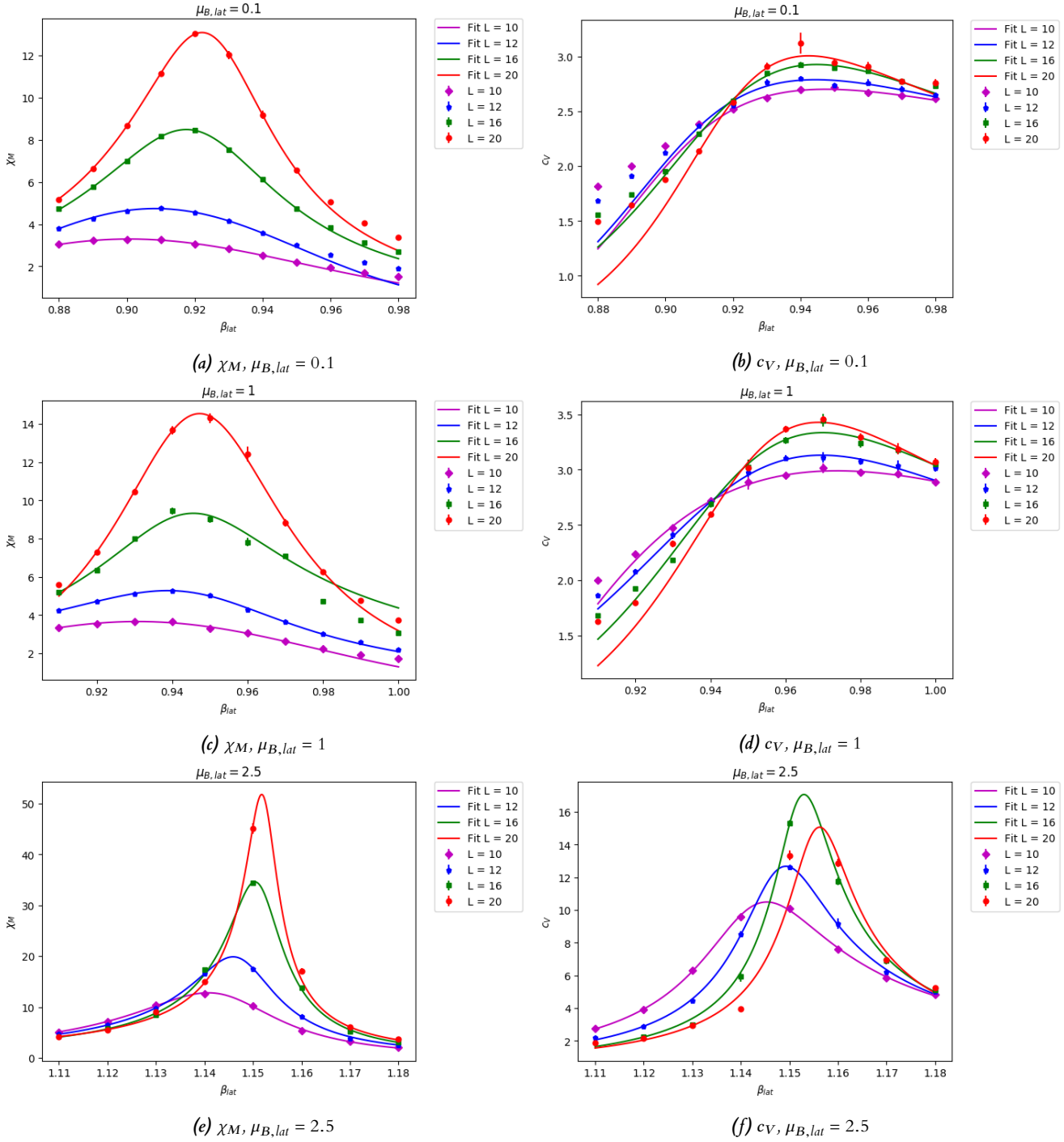

(a) χ_M, $\mu_{B,lat} = 0.1$

(b) c_V, $\mu_{B,lat} = 0.1$

(c) χ_M, $\mu_{B,lat} = 1$

(d) c_V, $\mu_{B,lat} = 1$

(e) χ_M, $\mu_{B,lat} = 2.5$

(f) c_V, $\mu_{B,lat} = 2.5$

Figure 5.27: *Observables and Johnson S_U function fits.*

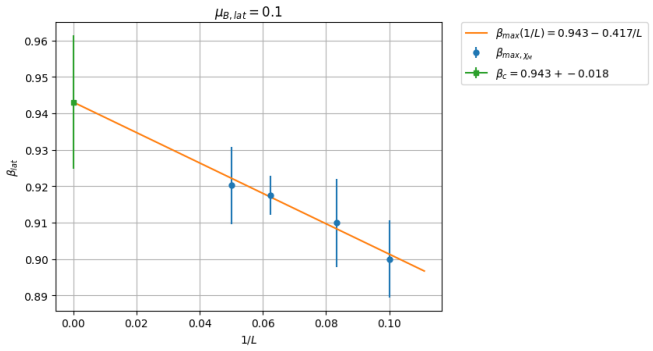

(a) From χ_M at $\mu_{B,lat} = 0.1$

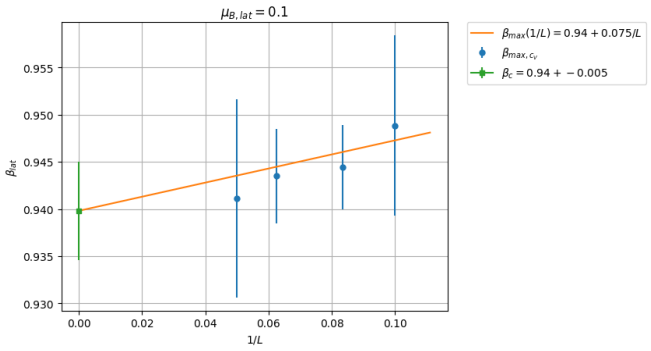

(b) From c_V at $\mu_{B,lat} = 0.1$

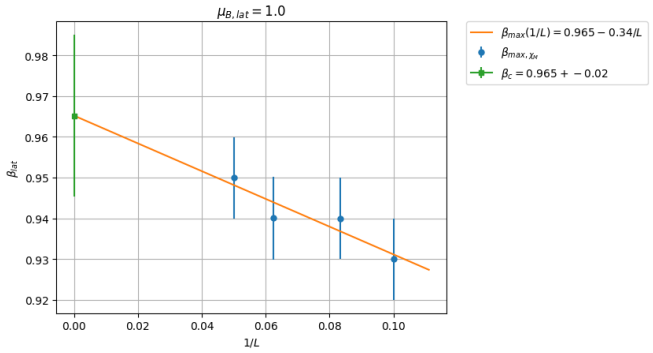

(c) From χ_M at $\mu_{B,lat} = 1$

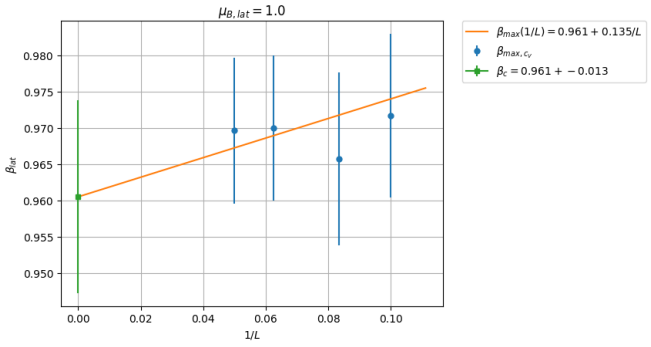

(d) From c_V at $\mu_{B,lat} = 1$

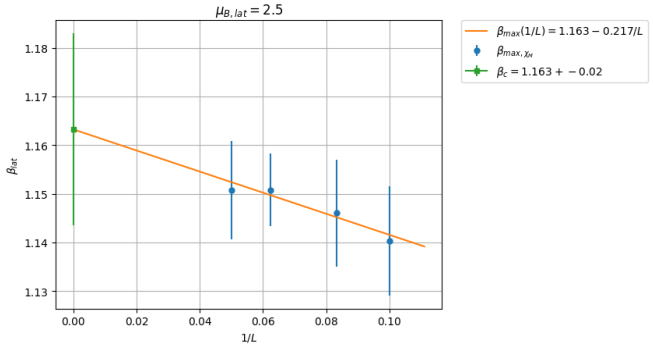

(e) From χ_M at $\mu_{B,lat} = 2.5$

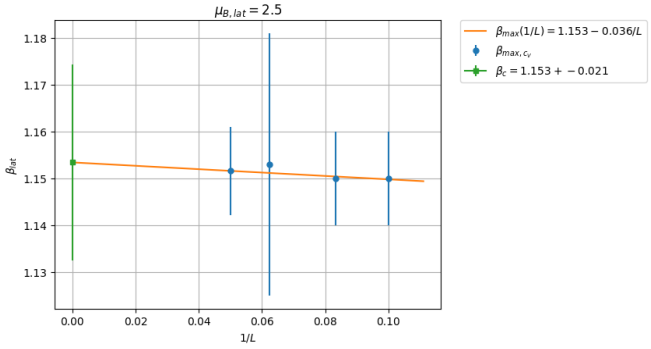

(f) From c_V at $\mu_{B,lat} = 2.5$

Figure 5.28: *β_{max} and $\beta_{c,lat}$ extrapolations. The errors were calculated using the jackknife method.*

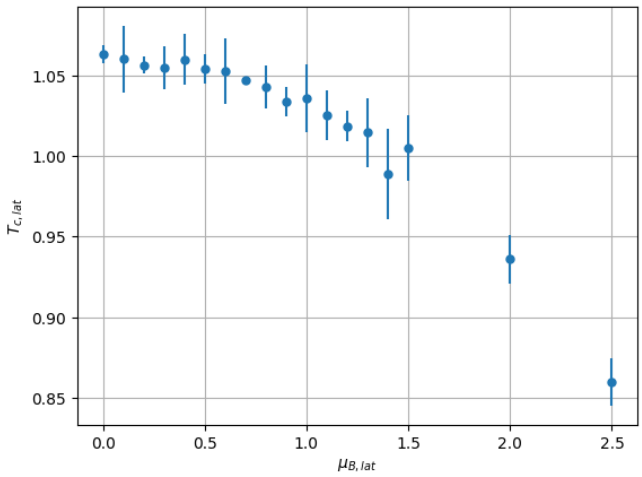

(a) χ_M

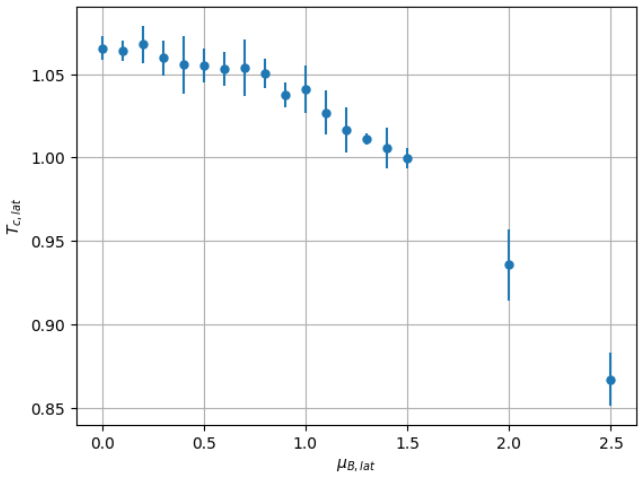

(b) c_V

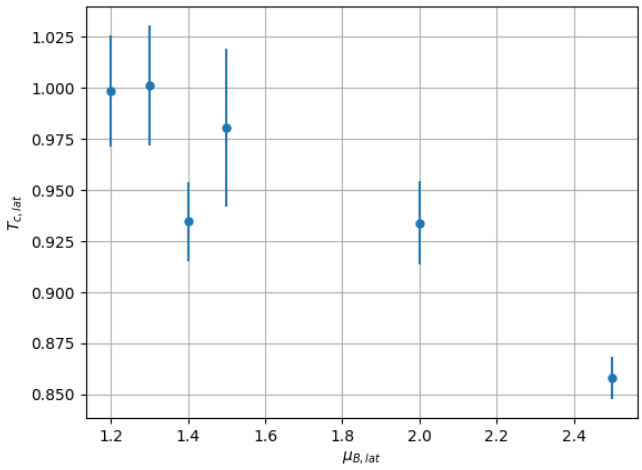

(c) χ_Q

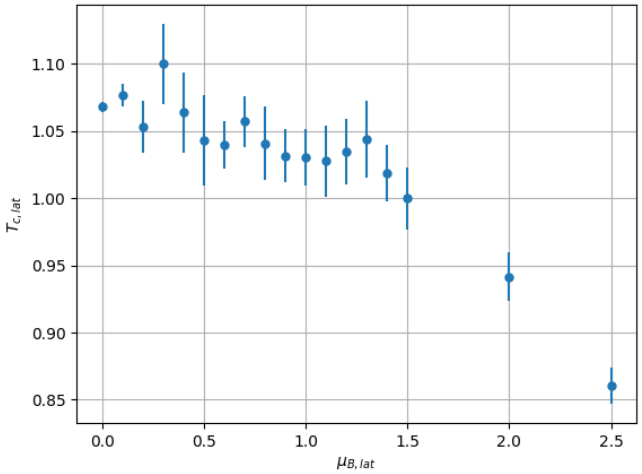

(d) τ_M

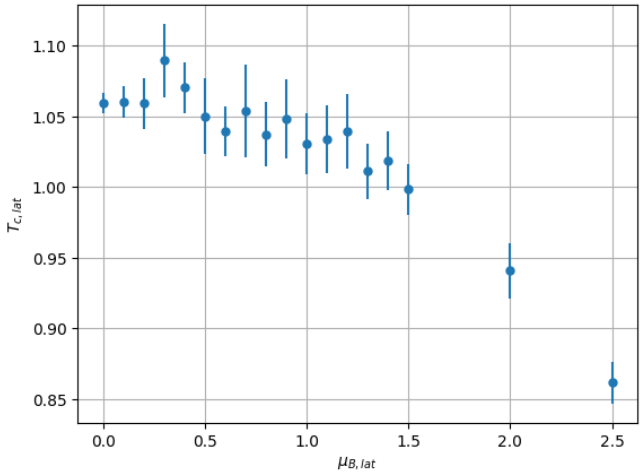

(e) τ_E

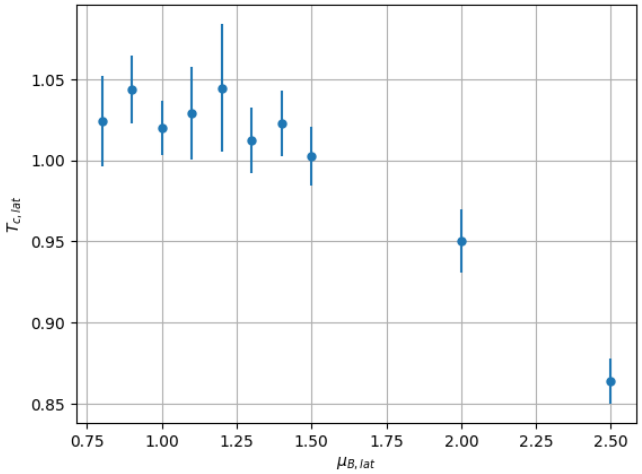

(f) τ_Q

Figure 5.29: *Phase diagrams in lattice units from* χ_M, c_V, χ_Q, τ_M, τ_E *and* τ_Q.

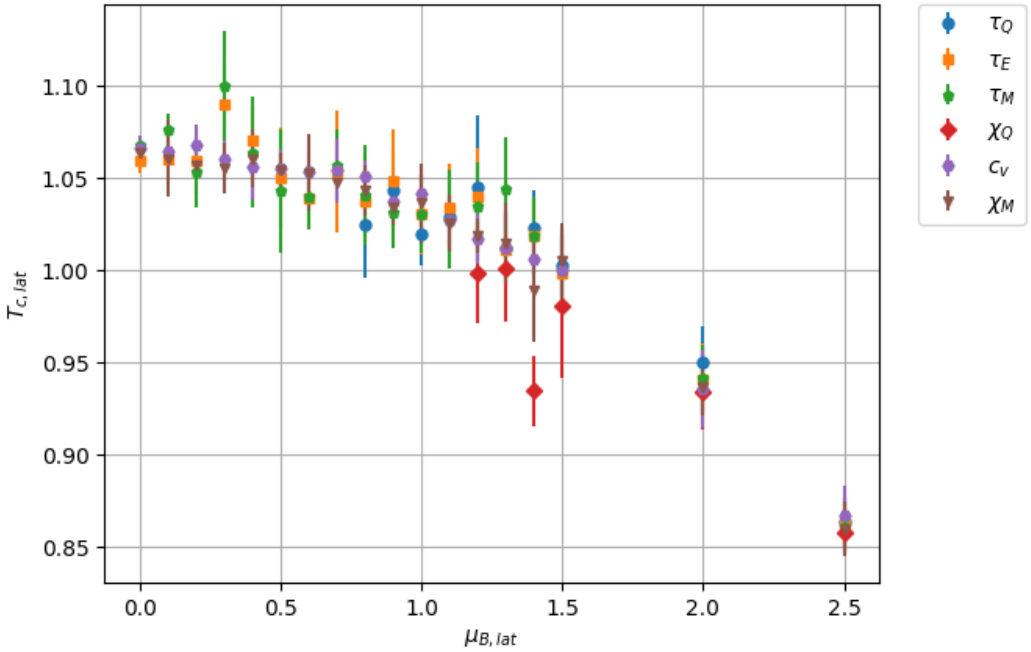

Figure 5.30: *Superposition of the phase diagrams in lattice units from χ_M, c_V, χ_Q, τ_M, τ_E and τ_Q. The phase diagrams of χ_Q and τ_Q begin at $\mu_{B,lat} = 1.2$ and 0.8 respectively.*

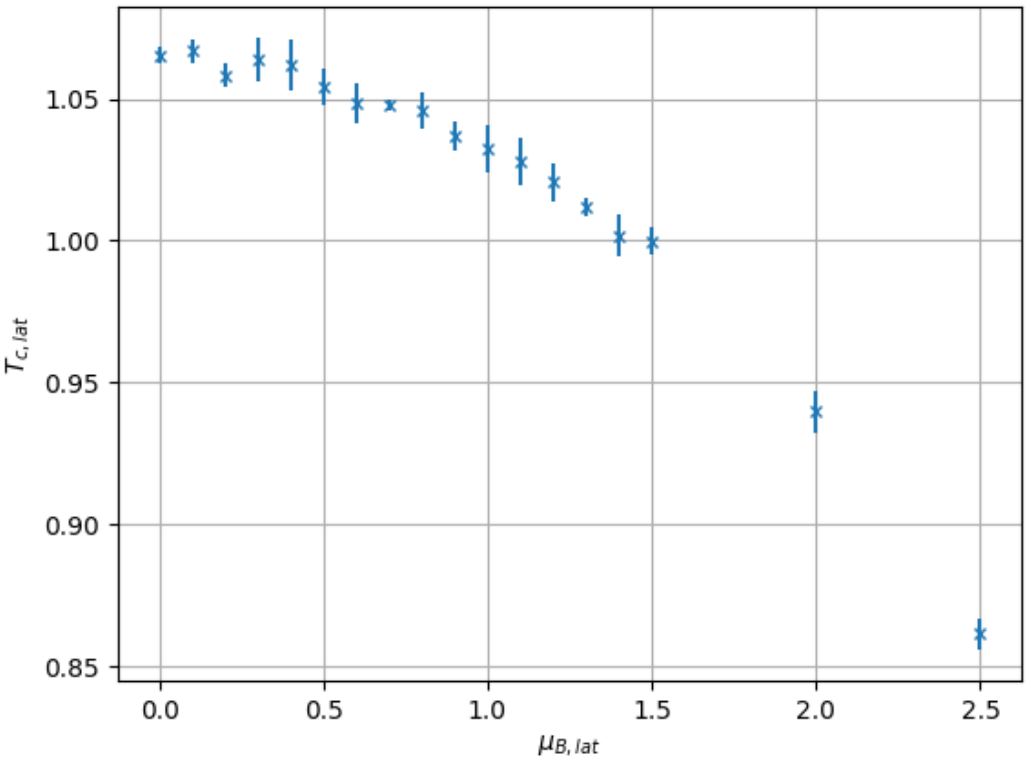

Figure 5.31: *Phase diagram obtained fitting a constant to the respective $\mu_{B,lat}$ points in our phase diagrams. The phase diagram shows the fit parameter errors.*

5.16 Phase diagram in physical units

We convert the lattice units of the phase diagrams to physical units with the formulas (2.69) and (2.70). We made the conversions using the $\mu_{B,\text{lat}} = 0$ values. Fig. 5.32 shows the phase diagrams in physical units of the observables and autocorrelation times χ_M, c_V, τ_M, τ_E. In this figure, we omit the phase diagrams from χ_Q and τ_Q because they are not standard quantities to determine the phase diagram. There is no evidence of a first order phase transition up to $\mu_B = 362$ MeV.

Fig. 5.33 shows the phase diagram from Figs. 5.31 converted to physical units. Our last point on the critical line, with coordinates $\mu_B = 362.7$ MeV and $T_c = 124.9(8)$ MeV, appears to agree with QCD only within 4 sigma [7], this discrepancy may be due to the masses of the quarks.

Tab. 5.4 shows some recently proposed locations of the critical end point (CEP) of the second order phase transition line of the QCD phase diagram.

Reference	T_{CEP}[MeV]	$\mu_{B,\text{CEP}}$[MeV]
Contrera et al. [75]	69.9-128.6	223.3-319.1
Cui et al. [76]	38	245
Kovács and Wolf [77]	53	885
Rougemont et al. [78]	< 130	> 400
Sharma [79]	< 145	$2T_{\text{CEP}}$
Antoniou et. al [80]	119-162	252-258
Ayala et al. [81]	18-45	315-349
Goswami et al. [82]	195.23-200.6	$\pi/3T_{\text{CEP}}$
Knaute et al. [83]	111.5	611.5
Li et al. [84]	100	240
Martínez and Raya [85]	49	310
Motta et al. [86]	122	862
Zhao et al. [87]	237	101
Ayala et al. [88]	40-51	271-291
Wu et al. [89]	69-72	813-971
Shi et al. [90]	116-127	135-160
Zhao et al. [91]	328-330	72-76
This work	< 124.9(8)	> 362.7

Table 5.4: *Recently proposed locations for the CEP in the QCD phase diagram. For a previous table see ref. [81].*

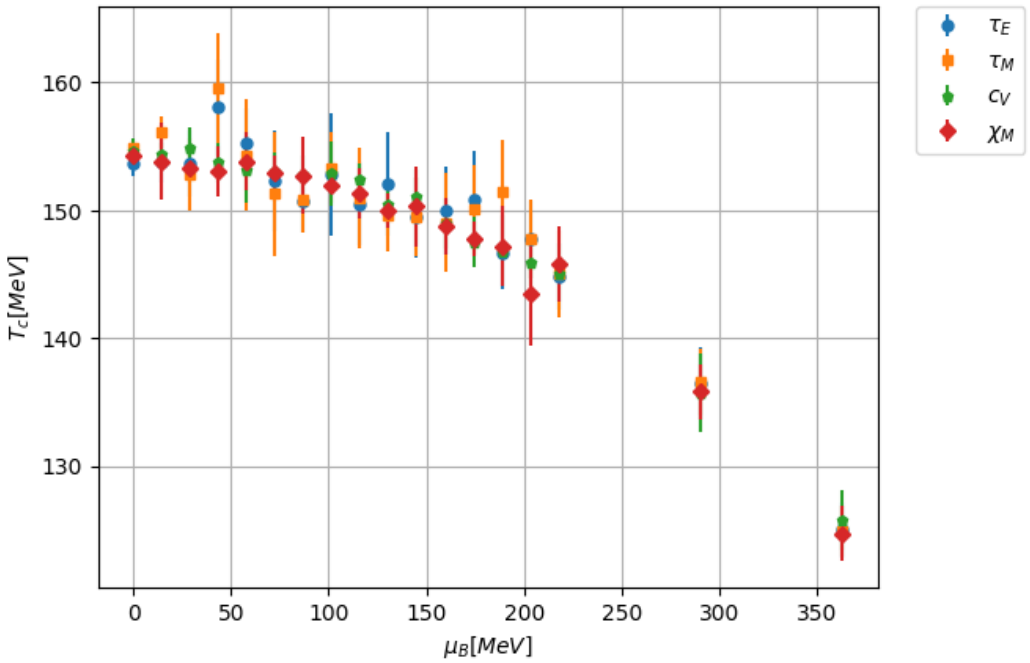

Figure 5.32: *Superposition of the phase diagrams in physical units from χ_M, c_V, τ_M and τ_E.*

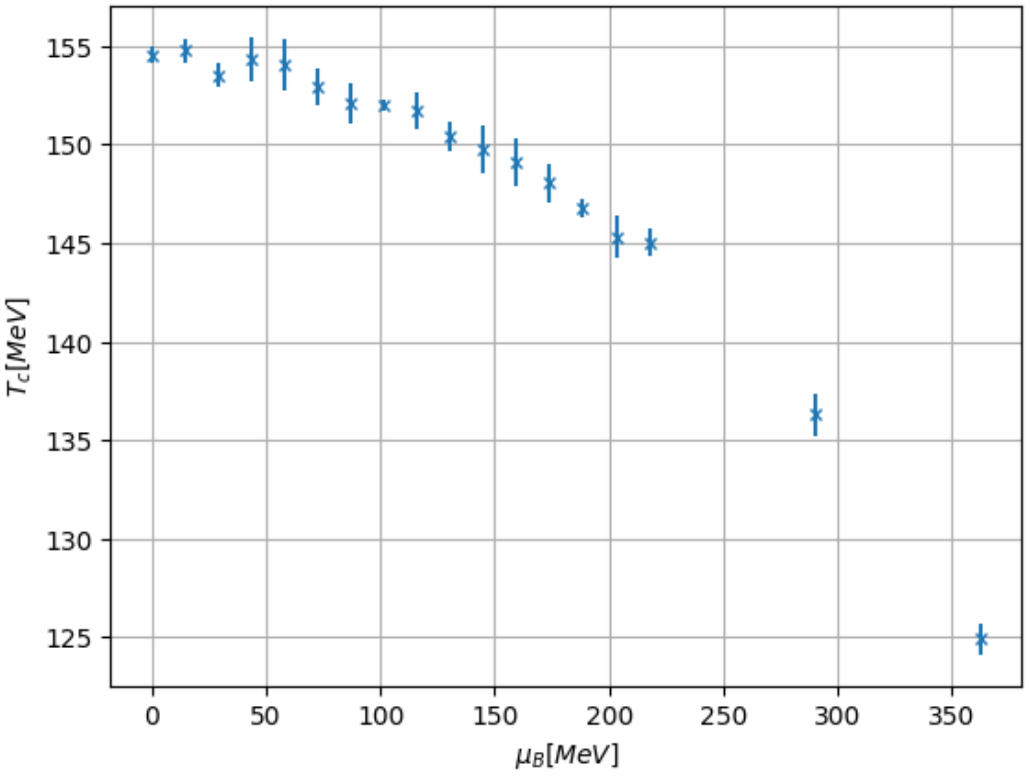

Figure 5.33: *Phase diagram from the constant fits converted to physical units.*

6 Conclusions

6.1 Summary

The main motivation for this thesis is that the critical points of the symmetry breakings of the 3d O(4) non-linear σ model and QCD with two flavors in the chiral limit are conjectured to be in the same universality class, but most of the literature ignores the topological sector of the 3d O(4) non-linear σ model. The topological charge of the 3d O(4) non-linear σ model can be interpreted as the baryon number. Therefore, the 3d O(4) non-linear σ model with chemical potential is an effective model for finite baryon density QCD with two flavors in the limit of massless quarks.

Our primary goal is to obtain the phase diagram of the 3d O(4) non-linear σ model at finite chemical potentials. The study must be carried out using non-perturbative methods. In this project we perform numerical simulations using a modified multicluster algorithm to include the topological charge in the acceptance probability.

We obtain the phase diagram by means of three observables (χ_M, c_V and χ_Q) and three autocorrelation times (τ_M, τ_E and τ_Q). We present the ratios of four critical exponents (α/ν, β/ν and γ/ν), and three dynamical critical exponents (z_M, z_E and z_Q). In this framework, we measure a set of observables, namely m, ϵ, q, χ_M, c_V, χ_Q, ξ, $\xi_{2\text{nd}}$ and M_{rms}.

6.2 Evaluation of results

The six phase diagrams which we obtain (one for each of the three observables and three autocorrelation times) are consistent within the errors. The final phase diagram boundary obtained with the other six is monotonically decreasing, as the phase diagram of QCD with two flavors in the chiral limit. Our critical temperature at $\mu_{B,\text{lat}} = 0$ is consistent with the literature.

There are no clear signs of a first order phase transition up to $\mu_{B,\text{lat}} = 2.5$ (362.7 MeV), but we cannot discard a phase transition of this order since the observables m, M_{rms}, ϵ and q have steeper slopes near the critical temperatures as the lattice volume or $\mu_{B,\text{lat}}$ increases. The plots of these observables at $\mu_{B,\text{lat}} = 2.5$ have pronounced slopes near the critical temperature, similar to those expected in first order phase transitions. Our volumes at $\mu_{B,\text{lat}} = 2.5$ are probably too small to infer, beyond any doubt, the order of the phase transitions.

We cannot assure the existence of a critical end point nor its possible position. But assuming the critical end point to exist and that the larger volume results for the order of the phase transitions are not different from our results, we place the critical end point at $T_{c,\text{lat}} < 0.861(5)$ and $\mu_{B,\text{lat}} > 2.5$, or in physical units, $T_c < 124.9(8)$ MeV and $\mu_B > 362.7$ MeV, which is in agreement with some proposals for the location of the CEP found in the literature.

There is a deviation of up to 15% in our critical exponents compared with the literature in the case $\mu_{B,\text{lat}} = 0$. This, together with the values of $\xi \approx O(L)$ near the critical temperatures, are indications of marked finite size effects. Although, also in the case $\mu_{B,\text{lat}} = 0$, the finite size effects still allow us to extrapolate the critical temperature consistently with the literature.

6.3 Algorithm

Including a nonzero baryon chemical potential in the 3d O(4) non-linear σ model makes our algorithm computationally much more expensive than the multicluster algorithm for the same model at $\mu_{B,\mathrm{lat}} = 0$. We have evident finite size effects. The time to generate each configuration and the autocorrelation times limit the statistics that we can accumulate in a reasonable time and the maximum lattice volumes. In the literature, lattice sizes of $L > 100$ are used in the case $\mu_{B,\mathrm{lat}} = 0$ to minimize the finite size effects [72].

6.4 Future work

There are many things to do in future projects. Some of them are:

- Perform simulations with larger lattice volumes, especially near $\mu_{B,\mathrm{lat}} = 2.5$, to improve the phase diagram and critical exponents. With larger volumes we can better infer the order of the phase transitions. The most stringent limitation is the autocorrelation time. In the case $L = 24$ at $\mu_{B,\mathrm{lat}} = 2.5$, generating a sample of 10^4 (minimally correlated) field configurations with 50 jobs would take at least 50 days (i.e. 6 hours per core per minimally correlated sample, higher frequency cores than our 2.60 GHz cores would reduce this time and more jobs would reduce the overall time, e.g. with 250 jobs, the total time would be reduced to 10 days).
- Refine the β_{lat} spacing to improve the phase diagram and critical exponents.
- Compute the critical exponents δ and ν.
- Explore the higher $\mu_{B,\mathrm{lat}}$ values to search the critical end point of the phase diagram.
- If the critical end point is found, search the possible "color superconductivity" zone of the phase diagram on larger $\mu_{B,\mathrm{lat}}$ values. In this phase the Fourier transform of the magnetization form a band structure.

A | Data of $L = 20$

A.1 Statistics

	$\mu_{B,\mathrm{lat}}$					
	0	0.1	0.2	0.3	0.4	0.5
β_{lat}	Statistics$[10^4]$					
0.88	20	10	–	–	–	–
0.89	20	5	10	10	–	–
0.9	10	5	10	10	5	20
0.91	10	5	6.6	6.7	3.3	2.5
0.92	6.7	3.3	6.6	5	2.5	4
0.93	5	2.5	5	4	2	3.3
0.94	5	2.5	5	4	1.7	3.3
0.95	5	2.5	5	5	2	3.3
0.96	6.6	3.3	5	2.5	2	3.3
0.97	6.6	3.3	5	2.5	2.5	4
0.98	6.6	3.3	3.4	2.5	2.5	4
0.99	6.6	–	–	–	2.5	2.5

	$\mu_{B,\mathrm{lat}}$					
	0.6	0.7	0.8	0.9	1	1.1
β_{lat}	Statistics$[10^4]$					
0.9	3.3	–	–	5	–	–
0.91	2.5	2.5	5	4	2	–
0.92	2	1.7	4.2	2.9	1.4	1.4
0.93	1.4	1.3	2.8	2.2	1.1	1.1
0.94	1.3	1.1	2.7	2.1	1.4	2.5
0.95	1.4	1.1	2.5	1.8	1.1	1.9
0.96	1.7	1.3	2.8	2.1	1.1	1.7
0.97	1.7	1.4	3.1	2	1.3	1.8
0.98	2	1.7	3.6	2.5	1.7	2.3
0.99	2	2	1.7	2.9	1.2	2.7
1	–	–	1.7	1.4	1.4	1.1
1.01	–	–	2	–	–	1.3

	$\mu_{B,\mathrm{lat}}$			
	1.2	1.3	1.4	1.5
β_{lat}	Statistics$[10^4]$			
0.92	1.4	–	–	–
0.93	2.2	1.1	–	–
0.94	2.7	4	1	–
0.95	2	3.2	2.3	2.7
0.96	1.6	1.3	1.7	2.2
0.97	1.5	1.1	1.3	1.5
0.98	1.8	1.2	1	1.2
0.99	2.5	1.5	1.2	1
1	2.1	1.9	1.5	1.2
1.01	1	2.3	2	1.6
1.02	1.1	2.5	2.5	2.1
1.03	–	–	2.9	2.5

	$\mu_{B,\mathrm{lat}}$
	2
β_{lat}	Statistics$[10^4]$
1.01	1.7
1.02	1.3
1.03	1.8
1.04	1.3
1.05	1
1.06	1.3
1.07	2
1.08	1.4
1.09	1.4

	$\mu_{B,\mathrm{lat}}$
	2.5
β_{lat}	Statistics$[10^4]$
1.11	2.5
1.12	2.1
1.13	1.4
1.14	1
1.15	1
1.16	1.3
1.17	1.4
1.18	3.1

A.2 Magnetization density

	$\mu_{B,\mathrm{lat}}$					
	0	0.1	0.2	0.3	0.4	0.5
β_{lat}	m					
0.88	0.07740(8)	0.0771(1)	–	–	–	–
0.89	0.08910(10)	0.0886(1)	0.0877(1)	0.0858(1)	–	–
0.9	0.1055(1)	0.1050(2)	0.1032(2)	0.1010(1)	0.0979(2)	0.0936(1)
0.91	0.1291(2)	0.1290(2)	0.1263(2)	0.1227(2)	0.1185(3)	0.1127(2)
0.92	0.1630(2)	0.1621(4)	0.1593(2)	0.1547(2)	0.1470(4)	0.1396(2)
0.93	0.2046(2)	0.2037(3)	0.2002(3)	0.1949(3)	0.1873(4)	0.1772(4)
0.94	0.2456(2)	0.2445(5)	0.2420(2)	0.2374(2)	0.2307(6)	0.2211(3)
0.95	0.2810(2)	0.2805(2)	0.2782(2)	0.2745(1)	0.2688(3)	0.2612(2)
0.96	0.3105(1)	0.3102(2)	0.3085(2)	0.3055(2)	0.3009(2)	0.2951(2)
0.97	0.3359(1)	0.3354(2)	0.3341(1)	0.3314(2)	0.3278(3)	0.3234(1)
0.98	0.3579(1)	0.3575(1)	0.3562(3)	0.3544(2)	0.3514(2)	0.3475(1)
0.99	0.3773(1)	–	–	–	0.3721(1)	0.3690(2)

	$\mu_{B,\mathrm{lat}}$					
	0.6	0.7	0.8	0.9	1	1.1
β_{lat}	m					
0.9	0.0895(4)	–	–	0.0747(1)	–	–
0.91	0.1057(3)	0.0988(2)	0.0922(2)	0.0856(2)	0.0789(3)	–
0.92	0.1301(2)	0.1210(4)	0.1107(3)	0.1007(4)	0.0926(3)	0.0825(2)
0.93	0.1651(5)	0.1525(7)	0.1380(4)	0.1232(5)	0.1104(9)	0.0977(4)
0.94	0.2085(4)	0.1933(7)	0.1758(3)	0.1576(5)	0.1380(4)	0.1193(4)
0.95	0.2514(4)	0.2378(5)	0.2212(3)	0.2001(7)	0.1757(9)	0.1517(3)
0.96	0.2868(3)	0.2765(2)	0.2633(3)	0.2463(3)	0.2238(3)	0.1969(4)
0.97	0.3174(3)	0.3093(3)	0.2987(3)	0.2856(2)	0.2674(4)	0.2446(5)
0.98	0.3426(2)	0.3356(3)	0.3280(1)	0.3175(3)	0.3038(3)	0.2865(3)
0.99	0.3648(2)	0.3594(2)	0.3527(2)	0.3443(2)	0.3338(3)	0.3204(2)
1	–	–	0.3741(4)	0.3680(1)	0.35929(9)	0.3483(2)
1.01	–	–	0.3939(1)	–	–	0.3721(4)

	$\mu_{B,\mathrm{lat}}$			
	1.2	1.3	1.4	1.5
β_{lat}	m			
0.92	0.0757(2)	–	–	–
0.93	0.0871(3)	0.0781(5)	–	–
0.94	0.1034(5)	0.0909(2)	0.0793(3)	–
0.95	0.1284(4)	0.1084(2)	0.0927(3)	0.0802(2)
0.96	0.1673(5)	0.1357(9)	0.1123(4)	0.0935(4)
0.97	0.2152(4)	0.1791(6)	0.1440(5)	0.1135(4)
0.98	0.2625(4)	0.2301(5)	0.1893(8)	0.1471(5)
0.99	0.3021(2)	0.2771(4)	0.2419(6)	0.1950(6)
1	0.3342(3)	0.3152(3)	0.2885(4)	0.2503(6)
1.01	0.3611(3)	0.3469(2)	0.3266(3)	0.2986(2)
1.02	0.3842(5)	0.3724(3)	0.3567(3)	0.3358(2)
1.03	–	–	0.3827(3)	0.3658(1)

	$\mu_{B,\mathrm{lat}}$
	2
β_{lat}	m
1.01	0.0741(2)
1.02	0.0864(2)
1.03	0.1068(4)
1.04	0.1416(5)
1.05	0.2035(7)
1.06	0.2804(7)
1.07	0.3398(4)
1.08	0.3816(2)
1.09	0.4139(2)

	$\mu_{B,\mathrm{lat}}$
	2.5
β_{lat}	m
1.11	0.0588(2)
1.12	0.0671(2)
1.13	0.0803(3)
1.14	0.1047(6)
1.15	0.1854(6)
1.16	0.3841(6)
1.17	0.4509(2)
1.18	0.4852(2)

A.3 Root mean square magnetization

	$\mu_{B,\mathrm{lat}}$					
	0	0.1	0.2	0.3	0.4	0.5
β_{lat}	M_{rms}					
0.88	0.08202(9)	0.0817(1)	–	–	–	–
0.89	0.0942(1)	0.0937(1)	0.0927(1)	0.0908(1)	–	–
0.9	0.1111(1)	0.1106(2)	0.1087(2)	0.1064(1)	0.1034(2)	0.0988(1)
0.91	0.1350(2)	0.1348(2)	0.1321(2)	0.1285(2)	0.1241(3)	0.1183(2)
0.92	0.1684(2)	0.1675(4)	0.1647(2)	0.1602(1)	0.1529(3)	0.1454(2)
0.93	0.2085(2)	0.2077(3)	0.2043(3)	0.1993(3)	0.1919(4)	0.1821(4)
0.94	0.2480(2)	0.2469(5)	0.2446(2)	0.2401(2)	0.2337(6)	0.2245(3)
0.95	0.2826(2)	0.2821(2)	0.2798(2)	0.2762(1)	0.2706(3)	0.2633(3)
0.96	0.3115(1)	0.3112(2)	0.3096(2)	0.3066(2)	0.3022(2)	0.2965(2)
0.97	0.3366(1)	0.3362(2)	0.3349(1)	0.3322(2)	0.3286(3)	0.3243(1)
0.98	0.3585(1)	0.3581(1)	0.3568(3)	0.3550(2)	0.3520(2)	0.3482(1)
0.99	0.3778(1)	–	–	–	0.3726(1)	0.3695(2)

	$\mu_{B,\mathrm{lat}}$					
	0.6	0.7	0.8	0.9	1	1.1
β_{lat}	M_{rms}					
0.9	0.0946(4)	–	–	0.0792(1)	–	–
0.91	0.1112(3)	0.1043(2)	0.0975(2)	0.0906(2)	0.0836(3)	–
0.92	0.1361(2)	0.1268(4)	0.1164(3)	0.1062(4)	0.0978(3)	0.0874(3)
0.93	0.1705(5)	0.1584(7)	0.1439(3)	0.1293(5)	0.1166(8)	0.1031(4)
0.94	0.2124(4)	0.1978(5)	0.1810(3)	0.1633(5)	0.1444(3)	0.1253(4)
0.95	0.2538(4)	0.2406(4)	0.2247(3)	0.2046(6)	0.1810(8)	0.1575(3)
0.96	0.2883(3)	0.2783(2)	0.2653(3)	0.2489(3)	0.2274(2)	0.2017(4)
0.97	0.3184(3)	0.3104(3)	0.3000(3)	0.2872(2)	0.2695(4)	0.2475(5)
0.98	0.3433(2)	0.3364(3)	0.3290(1)	0.3185(3)	0.3051(3)	0.2881(3)
0.99	0.3653(2)	0.3600(2)	0.3533(2)	0.3451(2)	0.3347(3)	0.3215(2)
1	–	–	0.3746(4)	0.3686(1)	0.35994(8)	0.3491(2)
1.01	–	–	0.3943(1)	–	–	0.3726(4)

	$\mu_{B,\mathrm{lat}}$			
	1.2	1.3	1.4	1.5
β_{lat}	M_{rms}			
0.92	0.0803(3)	–	–	–
0.93	0.0921(3)	0.0828(6)	–	–
0.94	0.1091(5)	0.0963(2)	0.0842(2)	–
0.95	0.1345(4)	0.1142(2)	0.0981(3)	0.0853(2)
0.96	0.1730(5)	0.1420(9)	0.1183(3)	0.0989(4)
0.97	0.2192(4)	0.1845(5)	0.1503(5)	0.1196(4)
0.98	0.2648(4)	0.2336(5)	0.1946(8)	0.1533(6)
0.99	0.3035(2)	0.2792(4)	0.2452(6)	0.2003(5)
1	0.3351(3)	0.3164(3)	0.2904(4)	0.2534(5)
1.01	0.3618(3)	0.3477(2)	0.3277(2)	0.3003(2)
1.02	0.3847(5)	0.3730(3)	0.3575(3)	0.3368(2)
1.03	–	–	0.3833(3)	0.3666(1)

	$\mu_{B,\mathrm{lat}}$
	2
β_{lat}	M_{rms}
1.01	0.0787(2)
1.02	0.0917(2)
1.03	0.1130(3)
1.04	0.1485(5)
1.05	0.2098(7)
1.06	0.2835(6)
1.07	0.3413(4)
1.08	0.3825(2)
1.09	0.4145(2)

	$\mu_{B,\mathrm{lat}}$
	2.5
β_{lat}	M_{rms}
1.11	0.0627(2)
1.12	0.0716(2)
1.13	0.0863(4)
1.14	0.1122(7)
1.15	0.1982(7)
1.16	0.3865(5)
1.17	0.4516(2)
1.18	0.4855(2)

A.4 Energy density

	$\mu_{B,\mathrm{lat}}$				
	0	0.1	0.2	0.3	0.4
β_{lat}	ϵ				
0.88	-0.85666(6)	-0.85634(7)	–	–	–
0.89	-0.87673(7)	-0.8764(1)	-0.8755(1)	-0.87427(8)	–
0.9	-0.89849(7)	-0.89830(8)	-0.8972(1)	-0.89566(7)	-0.8938(1)
0.91	-0.92286(8)	-0.9228(1)	-0.92140(8)	-0.9195(1)	-0.9171(1)
0.92	-0.9512(1)	-0.9506(3)	-0.9491(1)	-0.94667(7)	-0.9431(1)
0.93	-0.9833(1)	-0.9828(1)	-0.9809(2)	-0.9783(1)	-0.9743(2)
0.94	-1.0173(1)	-1.0164(4)	-1.0152(2)	-1.0124(1)	-1.0084(2)
0.95	-1.0511(1)	-1.05066(10)	-1.0492(2)	-1.04647(8)	-1.0426(2)
0.96	-1.0832(1)	-1.0830(3)	-1.0818(2)	-1.0793(1)	-1.0757(2)
0.97	-1.11406(10)	-1.1137(1)	-1.1125(1)	-1.1104(2)	-1.1072(2)
0.98	-1.1437(1)	-1.1432(1)	-1.1419(3)	-1.1404(2)	-1.1375(2)
0.99	-1.1717(1)	–	–	–	-1.1664(1)

	$\mu_{B,\mathrm{lat}}$					
	0.5	0.6	0.7	0.8	0.9	1
β_{lat}	ϵ					
0.9	-0.89095(8)	-0.8879(1)	-	-	-0.87664(8)	-
0.91	-0.9136(2)	-0.9097(2)	-0.9057(2)	-0.90106(8)	-0.89637(8)	-0.8913(2)
0.92	-0.9393(1)	-0.9345(3)	-0.9291(2)	-0.92343(7)	-0.91769(8)	-0.9117(1)
0.93	-0.9692(1)	-0.9630(2)	-0.9566(4)	-0.9492(2)	-0.9417(1)	-0.9340(2)
0.94	-1.0028(1)	-0.9961(2)	-0.9883(2)	-0.9792(1)	-0.9699(2)	-0.9599(2)
0.95	-1.0374(1)	-1.0310(1)	-1.0229(2)	-1.0133(1)	-1.0022(3)	-0.9899(2)
0.96	-1.0713(1)	-1.0654(2)	-1.0576(2)	-1.0489(2)	-1.0384(2)	-1.0254(3)
0.97	-1.10340(10)	-1.0982(2)	-1.0916(3)	-1.0839(1)	-1.0742(2)	-1.0620(1)
0.98	-1.1340(1)	-1.1293(1)	-1.1236(2)	-1.1168(2)	-1.1084(2)	-1.0974(2)
0.99	-1.1633(2)	-1.1594(2)	-1.1541(1)	-1.1477(1)	-1.1405(1)	-1.1309(2)
1	-	-	-	-1.1776(2)	-1.1714(3)	-1.1631(1)
1.01	-	-	-	-1.2063(1)	-	-

	$\mu_{B,\mathrm{lat}}$				
	1.1	1.2	1.3	1.4	1.5
β_{lat}	ϵ				
0.92	-0.9056(2)	-0.8998(1)	-	-	-
0.93	-0.9266(1)	-0.9194(1)	-0.9125(1)	-	-
0.94	-0.9502(1)	-0.94115(10)	-0.93276(7)	-0.9247(1)	-
0.95	-0.9777(1)	-0.9659(2)	-0.95496(8)	-0.94489(9)	-0.9361(1)
0.96	-1.0107(1)	-0.9959(1)	-0.9808(2)	-0.9679(1)	-0.95636(8)
0.97	-1.0477(2)	-1.0309(2)	-1.0124(2)	-0.9950(1)	-0.9795(1)
0.98	-1.0848(1)	-1.0690(2)	-1.0495(1)	-1.0281(2)	-1.0072(2)
0.99	-1.1202(2)	-1.1062(2)	-1.0884(2)	-1.0670(3)	-1.0416(3)
1	-1.1530(2)	-1.1411(2)	-1.1259(2)	-1.1068(2)	-1.0820(3)
1.01	-1.1844(3)	-1.1742(4)	-1.1613(2)	-1.1443(2)	-1.1236(2)
1.02	-	-1.2052(2)	-1.1939(2)	-1.1797(1)	-1.1614(2)
1.03	-	-	-	-1.2124(2)	-1.1967(2)

	$\mu_{B,\mathrm{lat}}$
	2
β_{lat}	ϵ
1.01	-0.9962(1)
1.02	-1.0157(1)
1.03	-1.0386(2)
1.04	-1.0671(2)
1.05	-1.1082(2)
1.06	-1.1618(3)
1.07	-1.2128(2)
1.08	-1.2574(2)
1.09	-1.2962(3)

	$\mu_{B,\mathrm{lat}}$
	2.5
β_{lat}	ϵ
1.11	-1.0913(1)
1.12	-1.1077(1)
1.13	-1.1266(1)
1.14	-1.1509(3)
1.15	-1.2016(3)
1.16	-1.3358(4)
1.17	-1.4030(2)
1.18	-1.4467(1)

A.5 Magnetic susceptibility

	$\mu_{B,\mathrm{lat}}$					
	0	0.1	0.2	0.3	0.4	0.5
β_{lat}	χ_M					
0.88	5.18(2)	5.16(2)	–	–	–	–
0.89	6.62(3)	6.65(4)	6.43(4)	6.27(3)	–	–
0.9	8.71(4)	8.68(6)	8.36(4)	8.17(4)	7.88(6)	7.28(3)
0.91	11.23(5)	11.15(5)	10.84(6)	10.61(6)	10.05(9)	9.6(1)
0.92	13.03(9)	13.1(1)	12.90(8)	12.94(7)	12.8(2)	12.16(8)
0.93	12.17(8)	12.0(2)	12.5(1)	12.69(9)	13.08(10)	13.2(1)
0.94	9.07(6)	9.2(2)	9.52(7)	9.83(8)	10.61(8)	11.4(2)
0.95	6.68(6)	6.55(6)	6.90(6)	7.02(6)	7.7(1)	8.4(1)
0.96	5.03(3)	5.07(4)	5.16(4)	5.42(6)	5.77(7)	5.99(9)
0.97	4.03(2)	4.05(4)	4.13(3)	4.31(8)	4.43(4)	4.70(4)
0.98	3.36(2)	3.36(3)	3.48(5)	3.47(4)	3.59(5)	3.79(2)
0.99	2.88(2)	–	–	–	3.11(3)	3.14(3)

	$\mu_{B,\mathrm{lat}}$					
	0.6	0.7	0.8	0.9	1	1.1
β_{lat}	χ_M					
0.9	6.70(5)	–	–	4.96(3)	–	–
0.91	8.61(6)	8.13(6)	7.28(4)	6.39(6)	5.58(5)	–
0.92	11.7(1)	10.6(1)	9.60(10)	8.40(6)	7.30(3)	6.1(1)
0.93	13.5(1)	13.5(2)	12.4(1)	11.4(1)	10.5(2)	8.2(1)
0.94	12.35(6)	13.2(4)	13.9(2)	13.9(1)	13.7(2)	11.0(1)
0.95	9.22(8)	10.4(2)	11.77(10)	13.6(1)	14.3(2)	13.6(1)
0.96	6.58(10)	7.6(1)	8.34(8)	10.2(3)	12.4(4)	14.6(2)
0.97	4.95(9)	5.43(8)	6.2(1)	7.08(6)	8.8(2)	11.0(2)
0.98	4.05(4)	4.36(6)	4.73(5)	5.31(7)	6.27(10)	7.5(1)
0.99	3.33(7)	3.48(4)	3.80(3)	4.29(4)	4.75(5)	5.60(5)
1	–	–	3.22(3)	3.48(8)	3.75(5)	4.32(6)
1.01	–	–	2.73(3)	–	–	3.6(1)

	$\mu_{B,\mathrm{lat}}$			
	1.2	1.3	1.4	1.5
β_{lat}	χ_M			
0.92	5.22(8)	–	–	–
0.93	6.64(6)	5.6(1)	–	–
0.94	9.1(1)	7.64(6)	6.05(5)	–
0.95	12.3(1)	9.83(8)	7.82(8)	6.33(5)
0.96	14.9(3)	13.4(2)	10.7(1)	7.9(2)
0.97	13.6(3)	15.3(2)	14.2(2)	11.1(2)
0.98	9.7(2)	12.7(2)	16.2(3)	14.7(3)
0.99	6.9(1)	9.2(1)	12.6(2)	16.6(4)
1	5.02(10)	6.31(5)	8.5(2)	12.8(2)
1.01	3.96(3)	4.65(5)	6.04(9)	8.1(2)
1.02	3.41(7)	3.72(3)	4.55(4)	5.84(7)
1.03	–	–	3.66(3)	4.45(3)

	$\mu_{B,\mathrm{lat}}$
	2
β_{lat}	χ_M
1.01	5.68(9)
1.02	7.7(1)
1.03	11.2(1)
1.04	16.7(1)
1.05	21.6(2)
1.06	14.8(3)
1.07	8.5(1)
1.08	5.67(8)
1.09	4.12(6)

	$\mu_{B,\mathrm{lat}}$
	2.5
β_{lat}	χ_M
1.11	4.22(3)
1.12	5.50(6)
1.13	9.0(3)
1.14	14.9(3)
1.15	45(1)
1.16	17.1(5)
1.17	6.02(3)
1.18	3.64(5)

A.6 Specific heat

	$\mu_{B,\mathrm{lat}}$					
	0	0.1	0.2	0.3	0.4	0.5
β_{lat}	c_V					
0.88	1.516(9)	1.493(9)	–	–	–	–
0.89	1.643(8)	1.64(2)	1.65(2)	1.63(1)	–	–
0.9	1.87(1)	1.88(1)	1.84(1)	1.82(1)	1.80(3)	1.711(10)
0.91	2.16(1)	2.14(2)	2.14(1)	2.10(1)	2.05(2)	2.01(2)
0.92	2.53(2)	2.58(3)	2.56(2)	2.49(2)	2.47(3)	2.32(2)
0.93	2.91(2)	2.91(3)	2.92(2)	2.91(2)	2.80(2)	2.78(2)
0.94	3.02(2)	3.12(10)	3.07(4)	3.04(2)	3.01(3)	3.05(3)
0.95	2.99(2)	2.94(3)	3.03(4)	3.03(3)	3.04(2)	3.12(2)
0.96	2.93(2)	2.91(4)	2.95(4)	3.00(5)	2.98(3)	3.03(3)
0.97	2.87(3)	2.78(2)	2.83(2)	2.93(4)	2.93(4)	2.98(3)
0.98	2.78(3)	2.76(3)	2.88(7)	2.75(3)	2.87(3)	2.85(2)
0.99	2.68(4)	–	–	–	2.76(2)	2.79(3)

	$\mu_{B,\mathrm{lat}}$					
	0.6	0.7	0.8	0.9	1	1.1
β_{lat}	c_V					
0.9	1.77(1)	–	–	1.54(1)	–	–
0.91	1.90(1)	1.81(2)	1.78(1)	1.697(10)	1.62(2)	–
0.92	2.23(3)	2.12(2)	2.022(9)	1.90(1)	1.79(2)	1.67(2)
0.93	2.65(3)	2.63(1)	2.39(3)	2.24(2)	2.33(3)	1.91(2)
0.94	3.05(2)	2.90(3)	2.87(2)	2.83(3)	2.60(3)	2.24(1)
0.95	3.18(4)	3.21(5)	3.23(3)	3.15(5)	3.01(4)	2.74(3)
0.96	3.08(4)	3.18(3)	3.23(4)	3.34(5)	3.37(3)	3.30(7)
0.97	3.10(3)	3.07(4)	3.20(3)	3.29(3)	3.46(3)	3.54(5)
0.98	2.94(4)	3.00(2)	3.07(3)	3.20(3)	3.29(3)	3.52(2)
0.99	2.86(4)	2.91(2)	3.15(4)	3.13(3)	3.19(5)	3.32(2)
1	–	–	2.91(4)	2.96(3)	3.07(4)	3.18(3)
1.01	–	–	2.79(3)	–	–	3.15(3)

	$\mu_{B,\mathrm{lat}}$			
	1.2	1.3	1.4	1.5
β_{lat}	c_V			
0.92	1.58(2)	–	–	–
0.93	1.76(1)	1.67(2)	–	–
0.94	2.02(2)	1.90(1)	1.72(2)	–
0.95	2.42(2)	2.15(1)	1.93(1)	1.76(1)
0.96	2.97(2)	2.65(4)	2.26(5)	1.981(10)
0.97	3.54(3)	3.30(3)	2.85(3)	2.36(2)
0.98	3.66(4)	3.63(5)	3.57(3)	2.89(4)
0.99	3.52(3)	3.83(5)	4.00(3)	3.77(7)
1	3.38(4)	3.60(3)	3.87(4)	4.14(6)
1.01	3.26(3)	3.46(3)	3.71(4)	4.00(4)
1.02	3.16(4)	3.33(4)	3.54(3)	3.83(4)
1.03	–	–	3.39(2)	3.61(3)

	$\mu_{B,\mathrm{lat}}$
	2
β_{lat}	c_V
1.01	1.91(2)
1.02	2.15(3)
1.03	2.64(2)
1.04	3.60(5)
1.05	5.64(6)
1.06	6.2(1)
1.07	5.53(5)
1.08	4.79(8)
1.09	4.32(6)

	$\mu_{B,\mathrm{lat}}$
	2.5
β_{lat}	c_V
1.11	1.87(2)
1.12	2.17(2)
1.13	2.94(3)
1.14	3.95(7)
1.15	13.3(3)
1.16	12.9(2)
1.17	6.9(1)
1.18	5.25(6)

A.7 Topological charge density

	$\mu_{B,\mathrm{lat}}$					
	0.1	0.2	0.3	0.4	0.5	0.6
β_{lat}	q					
0.88	0.001694(6)	–	–	–	–	–
0.89	0.001626(5)	0.003277(5)	0.004960(4)	–	–	–
0.9	0.001551(5)	0.003109(5)	0.004721(4)	0.006393(5)	0.008127(4)	0.009979(6)
0.91	0.001445(5)	0.002925(4)	0.004445(3)	0.006021(5)	0.007692(6)	0.009469(5)
0.92	0.001342(3)	0.002706(4)	0.004116(4)	0.005603(4)	0.007178(4)	0.008881(6)
0.93	0.001208(4)	0.002443(3)	0.003727(3)	0.005086(5)	0.006562(4)	0.008181(6)
0.94	0.001071(4)	0.002173(3)	0.003312(3)	0.004532(5)	0.005870(4)	0.007350(6)
0.95	0.000952(4)	0.001910(3)	0.002928(3)	0.004007(3)	0.005192(4)	0.006494(7)
0.96	0.000837(4)	0.001684(3)	0.002580(4)	0.003526(4)	0.004560(3)	0.005724(5)
0.97	0.000740(4)	0.001490(2)	0.002272(3)	0.003116(4)	0.004016(3)	0.005020(5)
0.98	0.000653(3)	0.001316(8)	0.002006(3)	0.002741(4)	0.003539(3)	0.004424(5)
0.99	–	–	–	0.002412(3)	0.003123(4)	0.003886(4)

	$\mu_{B,\mathrm{lat}}$					
	0.7	0.8	0.9	1	1.1	1.2
β_{lat}	q					
0.9	–	–	0.016291(5)	–	–	–
0.91	0.011363(7)	0.013409(5)	0.015615(5)	0.018015(8)	–	–
0.92	0.010707(7)	0.012699(4)	0.014863(6)	0.017215(7)	0.019790(9)	0.022565(8)
0.93	0.009929(7)	0.011859(5)	0.013984(7)	0.016305(10)	0.018861(10)	0.02164(1)
0.94	0.009000(8)	0.010845(6)	0.012909(9)	0.01522(1)	0.017793(7)	0.020585(8)
0.95	0.007977(9)	0.009697(5)	0.01165(1)	0.01393(1)	0.016464(8)	0.01931(1)
0.96	0.007025(7)	0.008522(7)	0.010279(9)	0.01238(1)	0.014854(10)	0.01771(1)
0.97	0.006158(6)	0.007465(5)	0.008996(8)	0.010845(9)	0.01309(1)	0.01579(2)
0.98	0.005417(6)	0.006556(5)	0.007875(7)	0.009489(9)	0.011394(9)	0.01379(1)
0.99	0.004767(5)	0.005764(6)	0.006907(3)	0.008276(7)	0.009931(7)	0.01198(1)
1	–	0.005057(5)	0.006061(6)	0.007238(7)	0.00867(1)	0.01041(1)
1.01	–	0.004449(4)	–	–	0.00758(2)	0.00907(1)
1.02	–	–	–	–	–	0.00791(1)

	$\mu_{B,\mathrm{lat}}$		
	1.3	1.4	1.5
β_{lat}	q		
0.93	0.02469(1)	–	–
0.94	0.023630(5)	0.02699(2)	–
0.95	0.022413(7)	0.02581(1)	0.02951(1)
0.96	0.02093(1)	0.02444(1)	0.02821(1)
0.97	0.01904(2)	0.02269(2)	0.02669(1)
0.98	0.01681(3)	0.02047(2)	0.02472(2)
0.99	0.01460(1)	0.01797(2)	0.02223(2)
1	0.01261(1)	0.01548(1)	0.01931(2)
1.01	0.01093(2)	0.01333(1)	0.01651(2)
1.02	0.009512(9)	0.01154(1)	0.01419(2)
1.03	–	0.009995(9)	0.01223(2)

	$\mu_{B,\mathrm{lat}}$
	2
β_{lat}	q
1.01	0.04704(2)
1.02	0.04512(2)
1.03	0.04274(2)
1.04	0.03956(4)
1.05	0.03474(4)
1.06	0.02850(4)
1.07	0.02317(3)
1.08	0.01906(2)
1.09	0.01590(3)

	$\mu_{B,\mathrm{lat}}$
	2.5
β_{lat}	q
1.11	0.08323(4)
1.12	0.08077(5)
1.13	0.07759(3)
1.14	0.07301(10)
1.15	0.06216(6)
1.16	0.03455(8)
1.17	0.02402(5)
1.18	0.01866(2)

A.8 Topological susceptibility

	$\mu_{B,\mathrm{lat}}$					
	0.1	0.2	0.3	0.4	0.5	0.6
β_{lat}	χ_Q					
0.88	0.01949(8)	–	–	–	–	–
0.89	0.01845(7)	0.01862(9)	0.01920(6)	–	–	–
0.9	0.01742(7)	0.01760(7)	0.01818(6)	0.01891(7)	0.01988(6)	0.02120(9)
0.91	0.01602(8)	0.01646(6)	0.01707(6)	0.01784(9)	0.01883(8)	0.0201(1)
0.92	0.01470(7)	0.01504(5)	0.01565(6)	0.01675(8)	0.01781(6)	0.01917(9)
0.93	0.01306(8)	0.01354(5)	0.01418(5)	0.01526(6)	0.01650(6)	0.01807(8)
0.94	0.01162(6)	0.01188(4)	0.01257(4)	0.01358(6)	0.01490(5)	0.01659(9)
0.95	0.01005(4)	0.01027(4)	0.01093(3)	0.01180(6)	0.01305(5)	0.01459(9)
0.96	0.00878(4)	0.00908(3)	0.00952(4)	0.01027(4)	0.01136(4)	0.01270(5)
0.97	0.00762(3)	0.00791(2)	0.00828(4)	0.00896(4)	0.00979(3)	0.01093(6)
0.98	0.00667(3)	0.00688(3)	0.00729(4)	0.00777(4)	0.00850(3)	0.00949(5)
0.99	–	–	–	0.00675(3)	0.00745(4)	0.00820(4)

	$\mu_{B,\mathrm{lat}}$					
	0.7	0.8	0.9	1	1.1	1.2
β_{lat}	χ_Q					
0.9	–	–	0.02596(9)	–	–	–
0.91	0.02164(9)	0.02330(7)	0.02509(8)	0.0273(1)	–	–
0.92	0.0209(1)	0.02244(6)	0.02445(8)	0.0268(1)	0.02911(10)	0.0315(2)
0.93	0.02012(10)	0.02179(6)	0.02388(9)	0.0266(1)	0.0288(1)	0.0312(2)
0.94	0.01857(9)	0.02095(9)	0.0236(1)	0.0265(3)	0.0284(1)	0.0309(1)
0.95	0.01680(8)	0.0194(1)	0.0223(2)	0.0252(1)	0.0283(2)	0.0312(1)
0.96	0.01465(7)	0.01687(9)	0.0199(1)	0.0238(1)	0.0278(2)	0.0318(3)
0.97	0.01256(6)	0.01462(7)	0.01717(8)	0.0208(2)	0.0254(2)	0.0309(3)
0.98	0.01074(5)	0.01251(7)	0.01485(6)	0.0176(1)	0.0219(2)	0.0272(3)
0.99	0.00936(4)	0.01083(5)	0.01271(6)	0.0151(2)	0.0186(1)	0.0233(1)
1	–	0.00925(5)	0.01072(5)	0.0128(1)	0.0158(1)	0.0194(2)
1.01	–	0.00802(4)	–	–	0.0134(2)	0.0163(1)
1.02	–	–	–	–	–	0.0140(1)

	$\mu_{B,\mathrm{lat}}$		
	1.3	1.4	1.5
β_{lat}	χ_Q		
0.93	0.0344(2)	–	–
0.94	0.0343(1)	0.0371(4)	–
0.95	0.0341(1)	0.0376(2)	0.0414(2)
0.96	0.0347(5)	0.0383(3)	0.0410(3)
0.97	0.0359(3)	0.0396(3)	0.0427(2)
0.98	0.0339(5)	0.0408(4)	0.0452(4)
0.99	0.0298(3)	0.0384(4)	0.0478(5)
1	0.0246(2)	0.0328(5)	0.0440(5)
1.01	0.0210(2)	0.0269(4)	0.0366(4)
1.02	0.0175(1)	0.0227(2)	0.0300(2)
1.03	–	0.0187(1)	0.0249(2)

	$\mu_{B,\mathrm{lat}}$
	2
β_{lat}	χ_Q
1.01	0.0721(5)
1.02	0.0743(4)
1.03	0.0805(6)
1.04	0.094(3)
1.05	0.118(1)
1.06	0.108(1)
1.07	0.078(2)
1.08	0.0569(8)
1.09	0.0425(6)

	$\mu_{B,\mathrm{lat}}$
	2.5
β_{lat}	χ_Q
1.11	0.1580(9)
1.12	0.171(2)
1.13	0.212(2)
1.14	0.246(4)
1.15	0.62(1)
1.16	0.37(1)
1.17	0.140(3)
1.18	0.0831(8)

A.9 Correlation length

	$\mu_{B,\mathrm{lat}}$					
	0	0.1	0.2	0.3	0.4	0.5
β_{lat}	ξ					
0.88	3.53(1)	3.51(1)	–	–	–	–
0.89	4.083(8)	4.06(1)	4.03(1)	3.92(1)	–	–
0.9	4.88(1)	4.85(1)	4.74(1)	4.64(1)	4.50(1)	4.29(1)
0.91	5.96(1)	5.96(2)	5.85(1)	5.67(2)	5.49(4)	5.21(2)
0.92	7.57(4)	7.56(6)	7.43(2)	7.15(2)	6.84(3)	6.42(2)
0.93	9.58(3)	9.53(4)	9.35(3)	9.11(3)	8.70(5)	8.23(4)
0.94	11.68(3)	11.66(7)	11.47(3)	11.26(4)	10.87(4)	10.40(5)
0.95	13.57(5)	13.57(6)	13.41(4)	13.24(4)	12.91(7)	12.6(2)
0.96	15.34(4)	15.3(1)	15.16(5)	15.1(2)	14.76(6)	14.34(9)
0.97	16.77(9)	16.70(8)	16.60(8)	16.50(7)	16.25(8)	15.94(6)
0.98	18.02(8)	17.90(9)	17.98(10)	17.9(5)	17.7(3)	17.27(6)
0.99	19.3(1)	–	–	–	19.0(3)	18.71(8)

	$\mu_{B,\mathrm{lat}}$					
	0.6	0.7	0.8	0.9	1	1.1
β_{lat}	ξ					
0.9	4.11(2)	–	–	3.38(1)	–	–
0.91	4.85(4)	4.50(2)	4.20(2)	3.90(2)	3.57(2)	–
0.92	5.97(3)	5.58(5)	5.07(3)	4.63(3)	4.24(2)	3.72(1)
0.93	7.62(4)	7.02(8)	6.37(3)	5.65(4)	5.06(7)	4.42(8)
0.94	9.76(7)	9.06(4)	8.13(3)	7.28(5)	6.44(3)	5.46(3)
0.95	11.93(6)	11.3(1)	10.45(6)	9.4(1)	8.11(6)	6.98(3)
0.96	13.96(9)	13.23(9)	12.58(4)	11.55(9)	10.45(9)	9.10(6)
0.97	15.30(8)	15.15(8)	14.5(1)	13.66(7)	12.7(1)	11.46(6)
0.98	17.08(7)	16.46(9)	16.29(8)	15.55(8)	14.79(7)	13.74(5)
0.99	18.6(1)	17.95(8)	17.6(1)	17.03(7)	16.44(7)	15.6(1)
1	–	–	18.7(1)	18.1(1)	17.50(8)	17.3(1)
1.01	–	–	20.0(1)	–	–	18.6(1)

	$\mu_{B,\mathrm{lat}}$			
	1.2	1.3	1.4	1.5
β_{lat}	ξ			
0.92	3.40(2)	–	–	–
0.93	3.93(3)	–	–	–
0.94	4.68(5)	–	–	–
0.95	5.87(4)	4.94(2)	4.19(2)	3.60(3)
0.96	7.68(8)	6.20(9)	5.10(2)	4.21(3)
0.97	10.00(7)	8.1(1)	6.53(6)	5.12(3)
0.98	12.24(8)	10.58(6)	8.68(6)	6.69(7)
0.99	14.59(8)	13.26(10)	11.31(8)	8.87(6)
1	16.2(1)	15.05(9)	13.67(9)	11.5(1)
1.01	17.5(1)	16.82(7)	15.62(6)	13.90(10)
1.02	19.1(2)	18.4(1)	17.38(8)	15.94(9)
1.03	–	–	18.9(2)	17.9(1)

	$\mu_{B,\mathrm{lat}}$
	2
β_{lat}	ξ
1.01	–
1.02	3.83(4)
1.03	4.81(3)
1.04	6.36(5)
1.05	9.20(10)
1.06	12.9(1)
1.07	16.24(7)
1.08	18.5(1)
1.09	20.3(2)

	$\mu_{B,\mathrm{lat}}$
	2.5
β_{lat}	ξ
1.11	–
1.12	–
1.13	3.66(3)
1.14	4.77(4)
1.15	8.69(7)
1.16	18.4(2)
1.17	23.0(3)
1.18	25.3(2)

6 Bibliography

[1] H. Fritzsch, M. Gell-Mann, and H. Leutwyler. Advantages of the Color Octet Gluon Picture. *Phys. Lett.*, 47B(4):365–368, 1973.

[2] S. Narison. *QCD as a Theory of Hadrons: From Partons to Confinement*. Cambridge University Press, 2004.

[3] D. Goldberg. *The Standard Model in a Nutshell*. Princeton University Press, 2017.

[4] M. K. Alford, A. Schmitt, K. Rajagopal, and T. Schäfer. Color superconductivity in dense quark matter. *RMP*, 80:1455–1515, 2008.

[5] K. Fukushima and T. Hatsuda. The phase diagram of dense QCD. *Rep. Prog. Phys.*, 74:014001, 2011.

[6] S. Sharma. Recent progress on the QCD phase diagram. *PoS Proc. Sci.*, LATTICE2018:009, 2019.

[7] P. Steinbrecher and HotQCD collaboration. The QCD crossover at zero and non-zero baryon densities from Lattice QCD. *Nucl. Phys. A*, 982:847–850, 2019.

[8] V. Kekelidze, A. Kovalenko, R. Lednicky, V. Matveev, V. Meshkov, A. Sorin, and G. Trubnikov. The NICA Project at JINR Dubna. *EPJ Web Conf.*, 71(00127), 2014.

[9] P. Senger. Status of the Compressed Baryonic Matter experiment at FAIR. *Int. J. Mod. Phys. E*, 29(2):2030001, 2020.

[10] T. Sakaguchi and J-PARC-HI collaboration. High density matter at J-PARC-HI. *PoS Proc. Sci.*, CORFU2018:189, 2019.

[11] J. Zinn-Justin. *Path Integrals in Quantum Mechanics*. Oxford University Press, 2010.

[12] O. Philipsen. Lattice calculations at non-zero chemical potential:The QCD phase diagram. *PoS Proc. Sci.*, Confinement8:011, 2008.

[13] P. de Forcrand. Simulating QCD at finite density. *PoS Proc. Sci.*, LAT2009:010, 2009.

[14] W. Bietenholz. On the Isomorphic Description of Chiral Symmetry Breaking by Nonunitary Lie Groups. *Int. J. Mod. Phys. A*, 25(8):1699–1712, 2010.

[15] M. A. Nava Blanco, W. Bietenholz, and A. Fernández Téllez. Conjecture about the 2-Flavour QCD Phase Diagram. *J. Phys.: Conf. Ser.*, 912:012048, 2017.

[16] M. Tanabashi et al. (Particle Data Group). Review of Particle Physics. *Phys. Rev. D*, 98:030001, 2018.

[17] S. Scherer. Introduction to Chiral Perturbation Theory. *Adv. Nucl. Phys.*, 27:277–538, 2003.

[18] S. L. Adler. Axial-Vector Vertex in Spinor Electrodynamics. *Phys. Rev.*, 177(5):2426–2438, 1969.

[19] J. S. Bell and R. Jackiw. A PCAC Puzzle: $\pi^0 \to \gamma\gamma$ in the σ Model. *Il Nuovo Cimento*, 60A(1):47–61, 1969.

[20] Y. Nambu. Quasi-Particles and Gauge Invariance in the Theory of Superconductivity. *Phys. Rev.*, 117(3):648–663, 1960.

[21] J. Goldstone. Field Theories with «Superconductor» Solutions. *Il Nuovo Cimento*, 19(1):154–164, 1961.

[22] J. Goldstone, A. Salam, and S. Weinberg. Broken Symmetries. *Phys. Rev.*, 127(3):965–970, 1962.

[23] W. Weise. The QCD vacuum and its hadronic excitations. *arXiv:nucl-th/0504087*, 2005.

[24] M. Gell-Mann, R. J. Oakes, and B. Renner. Behavior of Current Divergences under $SU_3 \times SU(3)_3$. *Phys. Rev.*, 175(5):2195–2199, 1968.

[25] G. 't Hooft. A two-dimensional model for mesons. *Nucl. Phys. B*, 75:461–470, 1975.

[26] E. Witten. Baryons in the 1/N expansion. *Nucl. Phys. B*, 160:57–115, 1979.

[27] T. H. R. Skyrme. A non-linear field theory. *Proc. Roy. Soc. A*, 260:127–138, 1961.

[28] G. S. Adkins, C. R. Nappi, and E. Witten. Static properties of nucleons in the Skyrme model. *Nucl. Phys. B*, 228:552–566, 1983.

[29] E. Witten. Current algebra, baryons, and quark confinement. *Nucl. Phys. B*, 223:433–444, 1983.

[30] J. Gasser and H. Leutwyler. Chiral Perturbation Theory to One Loop. *Annals Phys.*, 158:142–210, 1984.

[31] J. A. García Hernández. *Conjecture about the quantum chromodynamics phase diagram with two light quark flavors. Bachelor thesis, Universidad Nacional Autónoma de México.* 2020.

[32] R. D. Pisarszki and F. Wilczek. Remarks on the chiral phase transition in chromodynamics. *Phys. Rev. D*, 29(2):338–341, 1984.

[33] F. Wilczek. Application of The Renormalization Group to a Second-Order QCD Phase Transition. *Int. J. Mod. Phys. A*, 7(16):3911–3925, 1992.

[34] K. Rajagopal and F. Wilczek. Static and dynamic critical phenomena at a second order QCD phase transition. *Nucl. Phys. B*, 399:395–425, 1993.

[35] J. Engels, S. Holtmann, T. Mendes, and T. Schulze. Finite-size-sacling functions for 3d O(4) and O(2) spin models and QCD. *Phys. Lett. B*, 514:299–308, 2001.

[36] J. Zinn-Justin. *Quantum Field Theory and Critical Phenomena, Fourth Edition.* Oxford University Press, 2002.

[37] P. Goddard and D. I. Olive. Magnetic monopoles in gauge field theories. *Rep. Prog. Phys.*, 41:1357–1437, 1978.

[38] V. G. Makhankov, Y. P. Rybakov, and V. I. Sanyuk. *The Skyrme Model: Fundamentals, Methods, Applications.* Springer-Verlag, 1993.

[39] H. Meyer-Ortmanns and T. Reisz. *Principles of Phase Structures in Particle Physics, World Scientific Lecture Notes in Physics - Vol. 77.* World Scientific, 2007.

[40] B. Berg and M. Lüscher. Definition and statistical distribution of a topological number in the lattice O(3) σ-model. *Nucl. Phys. B*, 190(FS3):412–424, 1981.

[41] M. A. Nava Blanco. *Estudio del diagrama de fase con dos sabores de QCD usando el modelo 3d O(4). Master thesis, Benemérita Universidad Autónoma de Puebla.* 2019.

[42] G. E. Andrews, R. Askey, and R. Roy. *Encyclopedia of Mathematics and its Applications 71: Special Functions.* Cambridge University Press, 1999.

[43] J. Murakami. Volume formulas for a spherical tetrahedron. *Proc. Amer. Math. Soc.*, 140(9):3289–3295, 2012.

[44] T. D. Cohen, J. A. Ponciano, and N. N. Scoccola. Skyrmions semiclassical quantization in the presence of an isospin chemical potential. *Phys. Rev. D*, 78:034040, 2008.

[45] M. Creutz and B. Freedman. A Statistical Approach to Quantum Mechanics. *Ann. Phys.*, 132:427–462, 1981.

[46] S. Borsanyi et al. (Wuppertal-Budapest Collaboration). Is there still any T_c mystery in lattice QCD? Results with physical masses in the continuum limit III. *JHEP*, 09(073), 2010.

[47] M. Oevers. *The finite temperature phase diagram of 2-flavour QCD with improved Wilson fermions. Diploma thesis, Universität Bielefeld.* 1996.

[48] W. Bietenholz. *private communication.*

[49] G. Jaeger. The Eherenfest Classification of Phase Transitions: Introduction and Evolution. *Arch. Hist. Exact Sci.*, 53:51–81, 1998.

[50] P. Fierro and E. K. Nyer. *The Water Encyclopedia, Third Edition: Hydrologic Data and Internet Resources.* CRC press, 2007.

[51] A. Melinder. *Thermophysical Properties of Aqueous Solutions Used as Secondary Working Fluids. Doctoral Thesis, KTH Royal Institute of Technology.* 2007.

[52] J. Cardy. *Scaling and Renormalization in Statistical Physics.* Cambridge University Press, 1996.

[53] W. Bietenholz. *lecture notes.* 2019.

[54] M. Le Bellac, F. Mortessagne, and G. G. Batrouni. *Equilibrium and Non-Equilibrium Statistical Thermodynamics.* Cambridge University Press, 2004.

[55] J. Zinn-Justin. *Phase Transitions and Renormalization Group.* Oxford University Press, 2007.

[56] H. Nishimori and G. Ortiz. *Elements of Phase Transitions and Critical Phenomena.* Oxford University Press, 2011.

[57] O. G. Mouritsen. *Computer Studies of Phase Transitions and Critical Phenomena.* Springer-Verlag, 1984.

[58] K. Binder and D. W. Heermann. *Monte Carlo Simulations in Statistical Physics: An Introduction, 5th Edition.* Springer, 2010.

[59] M. E. J. Newman and G. T. Barkeman. *Monte Carlo Methods in Statistical Physics.* Oxford University Press, 1999.

[60] M. Hasenbusch. The two-dimensional XY model at the transition temperature: a high-precision Monte Carlo study. *J. Phys. A: Math. Gen.*, 38:5869–5883, 2005.

[61] W. S. Kendall, F. Liang, and J. S. Wang. *Markov Chain Monte Carlo: Innovations and Applications*. World Scientific, 2005.

[62] R. B. Ash and C. Doléans-Dade. *Probability and Measure Theory, Second Edition*. Harcourt/Academic Press, 2000.

[63] P. Guttorp. *Stochastic Modeling of Scientific Data*. Chapman Hall/CRC, 1995.

[64] D. Gamerman and H. F. Lopes. *Markov Chain Monte Carlo, Stochastic Simulation for Bayesian Inference, Second edition*. Chapman and Hall/CRC, 2006.

[65] N. Metropolis, A. W. Rosenbluth, M. N. Rosenbluth, and A. H. Teller. Equation of state calculations by fast computing machines. *J. Chem. Phys*., 21(6):1087–1092, 1953.

[66] J. Wang and R. H. Swendsen. Cluster Monte Carlo Algorithms. *Phys. A*, 167(3):565–579, 1990.

[67] R. H. Swendsen and J. Wang. Nonuniversal Critical Dynamics in Monte Carlo Simulations. *Phys. Rev. Lett*., 58(2):86–88, 1987.

[68] J. Hoshen and R. Kopelman. Percolation and cluster distribution. I. Cluster multiple labeling technique and critical concentration algorithm. *Phys. Rev. B*, 14:3438–3445, 1976.

[69] U. Wolff. Collective Monte Carlo Updating for Spin Systems. *Phys. Rev. Lett*., 62(4):361–364, 1989.

[70] U. Wolff. Collective Monte Carlo updating in a high precision study of the X-Y model. *Nucl. Phys. B*, 322:759–774, 1989.

[71] B. Efron. Computers and the theory of statistics: Thinking the unthinkable. *SIAM Rev*., 21(4):460–480, 1979.

[72] J. Engels, L. Fromme, and M. Seniuch. Correlation lengths and scaling functions in the three-dimensional O(4) model. *Nucl.Phys. B*, 675:533–554, 2003.

[73] N. L. Johnson. Systems of frequency curves generated by methods of translation. *Biometrika*, 36(1/2):149–176, 1949.

[74] W. G. Cochran. The χ^2 test of goodness of fit. *Ann. Math. Statist*., 23(3):315–345, 1952.

[75] G. A. Contrera, A. G. Grunfeld, and D. Blaschke. Supporting the search for the CEP location with nonlocal PNJL models constrained by lattice QCD. *Eur. Phys. J. A*, 52(231), 2016.

[76] Z. F. Cui, J. L. Zhang, and H. S. Zong. Proper time regularization and the QCD chiral phase transition. *Sci. Rep*., 7:45937, 2017.

[77] P. Kovács and G. Wolf. Phase diagram and isentropic curves from the vector meson extended Polyakov quark meson model. *Acta Phys. Pol. B Proc. Suppl*., 10(4):1107–1112, 2017.

[78] R. Rougemont, R. Critelli, J. Noronha-Hostler, J. Noronha, and C. Ratti. Dynamical versus equilibrium properties of the QCD phase transition: A holographic perspective. *Phys. Rev. D*, 96:014032, 2017.

[79] S. Sharma. The QCD Equation of state and critical end-point estimates at $O(\mu_B^6)$. *Nucl. Phys. A*, 967:728–731, 2017.

[80] N. G. Antoniou, F. K. Diakonos, X. N. Maintas, and C. E. Tsagkarakis. Locating the QCD critical endpoint through finite-size scaling. *Phys. Rev. D*, 97:034015, 2018.

[81] A. Ayala, S. Hernández-Ortiz, and L. A. Hernández. QCD phase diagram from chiral symmetry restoration: analytic approach at high and low temperature using the linear sigma model with quarks. *Rev. Mex. Fís.*, 64:302–313, 2018.

[82] J. Goswami, F. Karsch, A. Lahiri, M. Neumann, and C. Schmidt. Critical end points in (2+1)-flavor QCD with imaginary chemical potential. *PoS Proc. Sci.*, CORFU2018:162, 2018.

[83] J. Knaute, R. Yaresko, and B. Kämpfer. Holographic QCD phase diagram with critical point from Einstein–Maxwell-dilaton dynamics. *Phys. Lett. B*, 778:419–425, 2018.

[84] B. L. Li, Z. F. Cui, B. W. Zhou, S. An, L. P. Zhang, and H. S. Zong. Finite volume effects on the chiral phase transition from Dyson–Schwinger equations of QCD. *Nucl. Phys. B*, 938:298–306, 2019.

[85] A. Martínez and A. Raya. An innovative approach for sketching the QCD phase diagram within the NJL model using Lagrange Multipliers. *arXiv:1909.12416 [hep-ph]*, 2019.

[86] M. Motta, M. Alberico, A. Beraudo, P. Costa, and R.. Stiele. Exploration of the phase diagram and the thermodynamic properties of QCD at finite temperature and chemical potential with the PNJL effective model. *arXiv:1909.05037 [hep-ph]*, 2019.

[87] Y. P. Zhao, R. R. Zhang, H. Zhang, and H. S. Zong. Chiral phase transition from the Dyson-Schwinger equations in a finite spherical volume. *Chinese Phys. C*, 43(6):063101, 2019.

[88] A. Ayala, S. Hernández-Ortiz, L. A. Hernández, V. Knapp-Pérez, and R. Zamora. Fluctuating temperature and baryon chemical potential in heavy-ion collisions and the position of the critical end point in the effective QCD phase diagram. *Phys. Rev. D*, 101:074023, 2020.

[89] Z. Q. Wu, J. L. Ping, and H. S. Zong. QCD phase diagram at finite isospin and baryon chemical potentials with the self-consistent mean field approximation. *arXiv:2009.13070 [nucl-th]*, 2020.

[90] C. Shi, X. T. He, J. W. B., Q. W. Wang, S. S. Xu, and H. S. Zong. Chiral transition and the chiral charge density of the hot and dense QCD matter. *J. High Energ. Phys.*, 122:JHEP06, 2020.

[91] Y. P. Zhao, S. Y. Zuo, and C. M. Li. QCD phase diagram and critical exponents within the nonextensive Polyakov-Nambu-Jona-Lasinio model. *arXiv:2008.09276 [hep-ph]*, 2020.